LBL-23737
UC-34D

Lawrence Berkeley Laboratory
UNIVERSITY OF CALIFORNIA

Physics Division

Charged Hadron Production in e^+e^- Annihilation at $\sqrt{s} = 29$ GeV

TPC/Two-Gamma Collaboration

March 1988

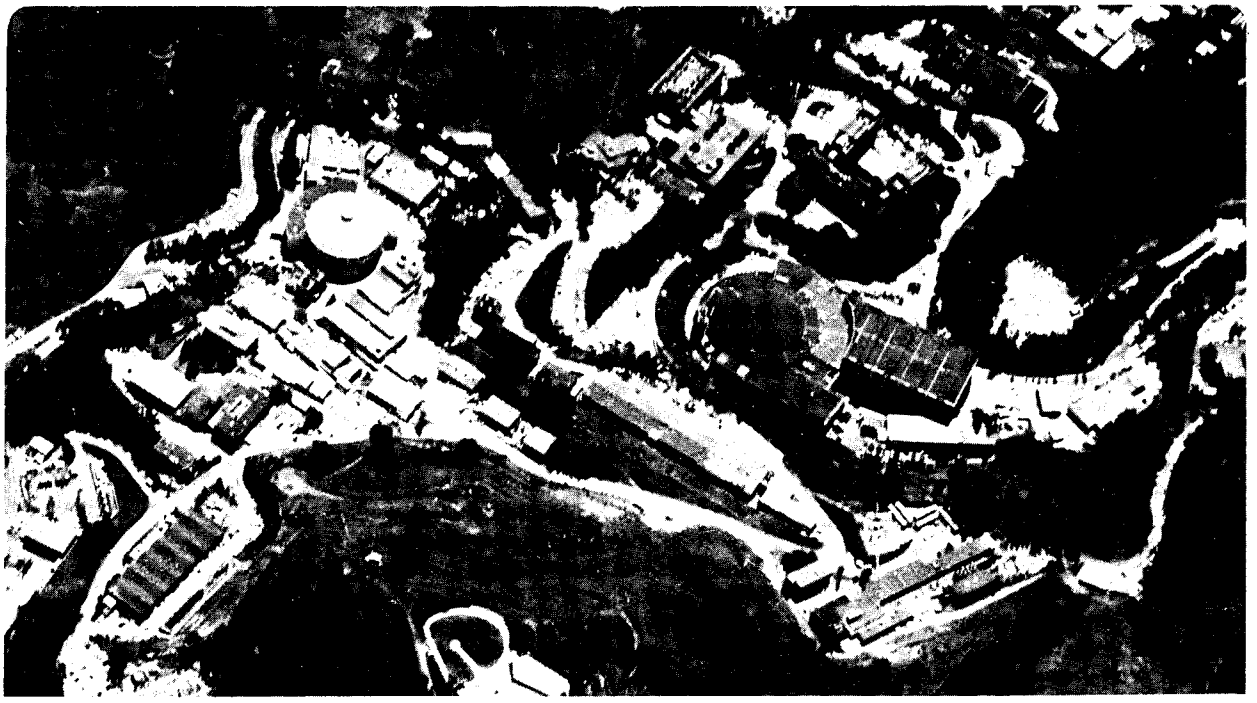

Prepared for the U.S. Department of Energy under Contract DE-AC03-76SF00098

DISCLAIMER

LBL-23737

Charged Hadron Production In e^+e^- Annihilation At $\sqrt{s} = 29$ GeV

H. Aihara,[n] M. Alston-Garnjost,[a] R.E. Avery,[a] A. Barbaro-Galtieri,[a] A.R. Barker,[g] B.A. Barnett,[j] D.A. Bauer,[g] H-U. Bengtsson,[d] G.J. Bobbink,[m] C.D. Buchanan,[d] A. Buijs,[m] D.O. Caldwell,[g] H-Y. Chao,[i] S-B. Chun,[d] A.R. Clark,[a] G.D. Cowan,[a] D.A. Crane,[j] O.I. Dahl,[a] M. Daoudi,[e] K.A. Derby,[a] J.J. Eastman,[a] P.H. Eberhard,[a] T.K. Edberg,[a] A.M. Eisner,[c] R. Enomoto,[n] F.C. Erné,[m] K.H. Fairfield,[f] J.M. Hauptman,[i] W. Hofmann,[a] J. Hylen,[j] T. Kamae,[n] H.S. Kaye,[a] R.W. Kenney,[a] S. Khacheryan,[d] R.R. Kofler,[k] W.G.J. Langeveld,[e] J.G. Layter,[e] W.T. Lin,[e] F.L. Linde,[m] S.C. Loken,[a] A. Lu,[g] G.R. Lynch,[a] R.J. Madaras,[a] B.D. Magnuson,[c] G.E. Masek,[f] L.G. Mathis,[a] J.A.J. Matthews,[j] S.J. Maxfield,[k] E.S. Miller,[f] W. Moses,[a] D.R. Nygren,[a] P.J. Oddone,[a] H.P. Paar,[f] S.K. Park,[i] D.E. Pellett,[b] M. Pripstein,[a] M.T. Ronan,[a] R.R. Ross,[a] F.R. Rouse,[a] K.A. Schwitkis,[g] J.C. Sens,[m] G. Shapiro,[a] B.C. Shen,[e] W.E. Slater,[d] J.R. Smith,[b] J.S. Steinman,[d] R.W. Stephens,[g] M.L. Stevenson,[a] D.H. Stork,[d] M.G. Strauss,[d] M.K. Sullivan,[c] T. Takahashi,[n] S. Toutounchi,[k] R. van Tyen,[a] G.J. VanDalen,[e] W. Vernon,[f] W. Wagner,[b] E.M. Wang,[a] Y-X. Wang,[g] W.A. Wenzel,[a] Z.R. Wolf,[a] H. Yamamoto,[a] S.J. Yellin,[g] C. Zeitlin[b]

TPC/Two-Gamma Collaboration

[a] *Lawrence Berkeley Laboratory, University of California, Berkeley, California 94720*

[b] *University of California, Davis, California 95616*

[c] *University of California Intercampus Institute for Research at Particle Accelerators, Stanford, California 94305*

[d] *University of California, Los Angeles, California 90024*

[e] *University of California, Riverside, California 92521*

[f] *University of California, San Diego, California 92093*

[g] *University of California, Santa Barbara, California 93106*

[i] *Ames Laboratory, Iowa State University, Ames, Iowa 50011*

[j] *Johns Hopkins University, Baltimore, Maryland 21218*

[k] *University of Massachusetts, Amherst, Massachusetts 01003*

[m] *National Institute for Nuclear and High Energy Physics, Amsterdam, The Netherlands*

[n] *University of Tokyo, Tokyo, Japan*

Abstract

We have used data from the Time Projection Chamber at the SLAC storage ring PEP to study the inclusive production of charged hadrons in e^+e^- annihilation at a center of mass energy of 29 GeV. Charged particles were identified by simultaneous dE/dx and momentum measurements. We present cross sections and particle fractions for $\pi^{\pm}$, $k^{\pm}$, and $p(\bar{p})$ as a function of energy, momentum, rapidity, and transverse momentum. We compare the predictions of various hadronization models to the data and note discrepancies at high momentum.

This work is supported by the United States Department of Energy under Contract DE-AC03-76SF00098.

Contents

1 INTRODUCTION

The fragmentation of quarks into jets of hadrons under the influence of color confinement forces is one of the fundamental phenomena in high energy reactions, yet it is poorly understood theoretically and the subject of numerous phenomenological models. The reaction $e^+e^- \rightarrow$ hadrons provides a very clean environment to study quark fragmentation, and to establish a rich base of data against which fragmentation models as well as measurements of particle production in other reactions can be compared. The goal of this paper is to provide a coherent set of inclusive charged pion, kaon, and proton cross sections and associated particle fractions in commonly used variables such as rapidity, Feynman x, transverse momentum, etc.

The data were taken at the PEP electron-positron storage ring at the Stanford Linear Accelerator Center using the TPC/Two-Gamma detector facility. A first data sample of 77 pb^{-1} was taken in 1982/83. A second event sample of 68 pb^{-1} was collected in 1984/86. Both data sets were taken at a center of mass energy of 29 GeV. In 1984, between the two running cycles, numerous improvements were made to the detector, the main one being the replacement of the 3.89 kG conventional coil by a 13.25 kG superconducting coil resulting in a major improvement in the momentum resolution. Other important improvements included a gated grid system to reduce space charge distortions in the Time Projection Chamber (TPC), a thinner field cage to reduce the amount of material in front of the TPC, and a better electronics calibration and monitoring system which improves the position resolution of the TPC. Because of the superior quality of the second data set, all results quoted here are based on this set. Data from the first set were analyzed in a consistent fashion and served as an additional cross-check.

Relying on the excellent particle identification capabilities and the good momentum resolution of the TPC, we derived the following cross sections for $e^+e^- \rightarrow \gamma^* \rightarrow \pi^\pm$, $k^\pm$, and $p,\bar{p}$:

1. $\frac{1}{\beta\sigma}\frac{d\sigma}{dx}$ $\quad (x = 2E/\sqrt{s})$
2. $\frac{z}{\sigma}\frac{d\sigma}{dz}$ $\quad (z = 2p/\sqrt{s})$
3. $\frac{1}{\sigma}\frac{d\sigma}{d|y|}$ $\quad (y = \frac{1}{2}\ln(\frac{E+p_\parallel}{E-p_\parallel}))$
4. $\frac{1}{\sigma}\frac{d\sigma}{dp_t^2}$
5. $\frac{1}{\sigma}\frac{d\sigma}{d|y|dp_t^2}$

This is the first time the rapidity (y), transverse momentum (p_t), and double differential cross sections have been measured separately for pions, kaons, and protons in e^+e^- annihilation at these energies.

Descriptions of the TPC/Two-Gamma detector and its major subsystems are given in section 2. Event reconstruction and event selection are discussed in section 3. Section 4 provides a detailed description of particle identification by dE/dx in the TPC. The measurement of the inclusive cross sections and particle fractions is discussed in section 5. Finally, in section 6 the results are presented and comparisons with hadronization models are made.

2 THE TPC/TWO-GAMMA DETECTOR FACILITY

2.1 Overview

The TPC/Two-Gamma detector facility is located at Interaction Region (IR) 2 of the PEP e^+e^- storage ring at SLAC. A cross section of the detector is shown in Fig. 1. The beam interaction region is surrounded by a cylindrical drift chamber (IDC) used mainly for triggering, followed (in the radial direction) by the Time Projection Chamber (TPC) as the main tracking device, a solenoidal magnet coil, an outer drift chamber (ODC), the electromagnetic barrel calorimeter (HEX), muon absorber steel serving as a flux return, and a muon detection system. Forward calorimeters and muon systems and small angle detectors complete the detector system. In this section, we will concentrate on the TPC as the primary detector component used in this analysis, and give only brief descriptions of the other components.

The material in front of the TPC is distributed as shown in Table 1 [1,2]. The beam pipe is made of aluminum with an inner radius of 8.5 cm and thickness of 0.203 cm. The beam pipe is cooled by six water filled aluminum tubes with an outside diameter of 0.635 cm and a wall thickness of 0.127 cm. These tubes add 4.5% of a radiation length to 7.1% of the particles. Surrounding the beam pipe is the aluminum pressure wall of the TPC and IDC. Its inner radius is 10.95 cm and its thickness is 0.635 cm, which is 7.1% of a radiation length.

The inner drift chamber [3] extends from roughly 13 cm to 19 cm in radius and is 1.2 m long, covering 95% of 4π. It consists of 4 axial layers of proportional chambers filled with 8.5 atm. of argon-methane gas (80%-20%). Each layer contains 60 sense wires uniformly distributed for a total of 240 sense wires, and is rotated 3° (half a cell size) with respect to the previous layer. At present the inner drift chamber is only used for triggering.

Outside the inner drift chamber is the Time Projection Chamber (TPC) [4], the detector used for this analysis. The TPC extends from roughly 22 cm to 97 cm in radius and is 2 m long. It is filled with argon-methane gas (80%-20%) at 8.5 atm. Fig. 2 shows the field configurations in the TPC. The axial magnetic field bends particle trajectories while the parallel, axial electric field sweeps the resulting ionization electrons to the endcaps. The ionization is measured at the endcaps giving position and dE/dx information. Particles are identified by simultaneous measurement of momentum (via the track curvature) and velocity (via dE/dx). The TPC is described in greater detail in section 2.2.

The axial drift field in the TPC is maintained by an inner and an outer field cage. A high voltage insulator separates the IDC and TPC. In 1984 the original mylar-polyurethane insulator was replaced by an insulator made of polyethylene on a carbon fiber support cylinder. This reduced the amount of material of the insulator plus field cage from 7.5% to 3.2% of a radiation length. The cumulative amount of material in front of the TPC was 19.6% of a radiation length before 1984

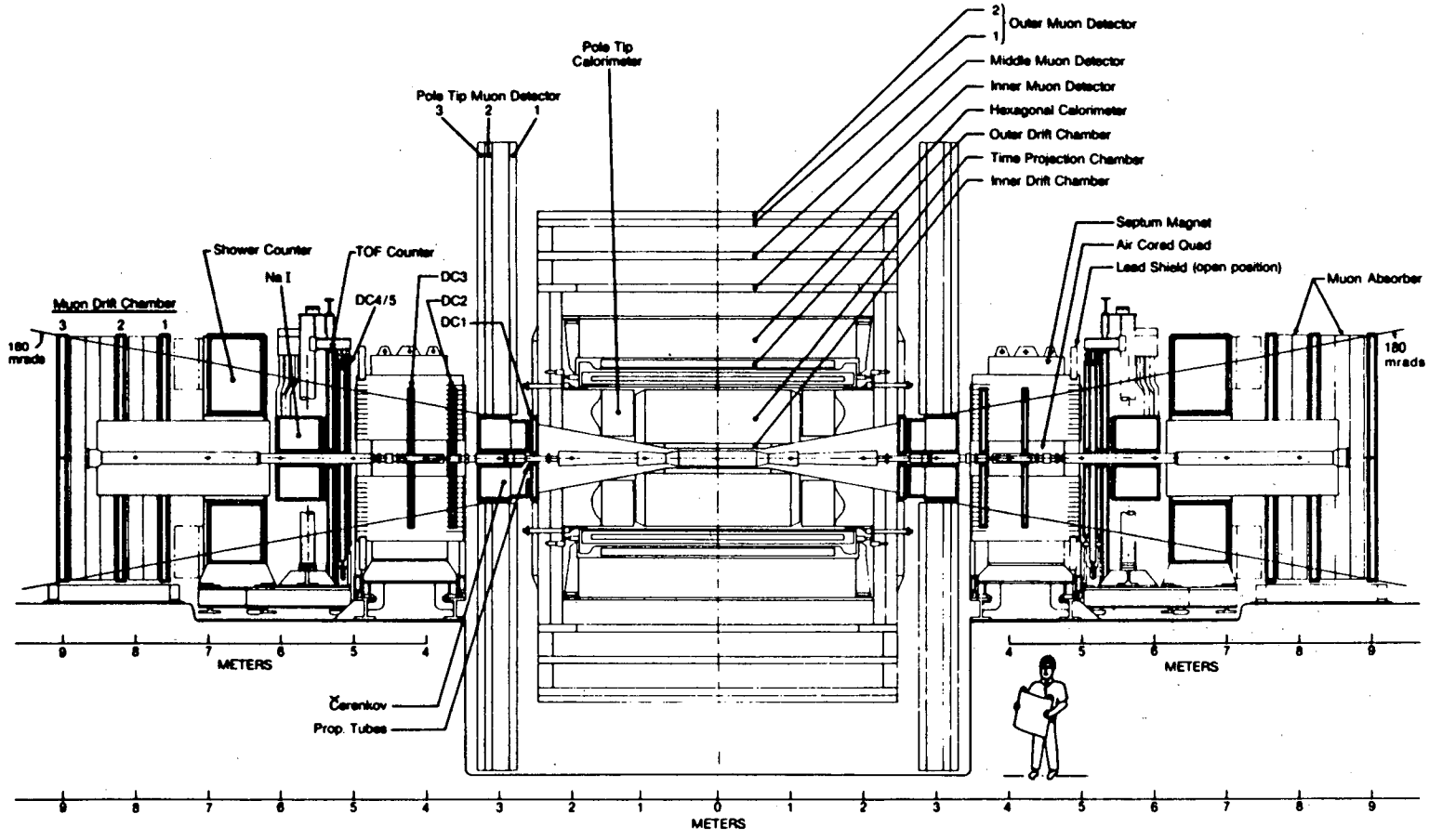

Figure 1: Diagram of the TPC/Two-Gamma detector showing the Time Projection Chamber and other detector systems.

Component	Inner Radius (cm)	Before 1984		After 1984	
		Radiation Length (%)	Cumulative Rad. Length (%)	Radiation Length (%)	Cumulative Rad. Length (%)
Beam Pipe	8.50	2.3	2.3	2.3	2.3
Cooling Tubes	8.70	0.3	2.6	0.3	2.6
Pressure Wall	10.95	7.1	9.7	7.1	9.7
Gas Gap	11.59	0.1	9.8	0.1	9.8
Inner Drift Chamber	13.18	2.3	12.1	2.6	12.4
Insulator + Field Cage	20.00	7.5	19.6	3.2	15.6
TPC Volume	22.25	4.9	24.5	4.9	20.5
Field Cage + Insulator	97.05	10.1	34.6	10.1	30.6
Gas Gap	100.50	0.1	34.7	0.1	30.7
Magnet Coil Package	102.00	131.9	166.6	87.4	118.1
Outer Drift Chamber	119.00	6.5	173.1	6.5	124.6

Table 1: Distribution of material in the TPC.

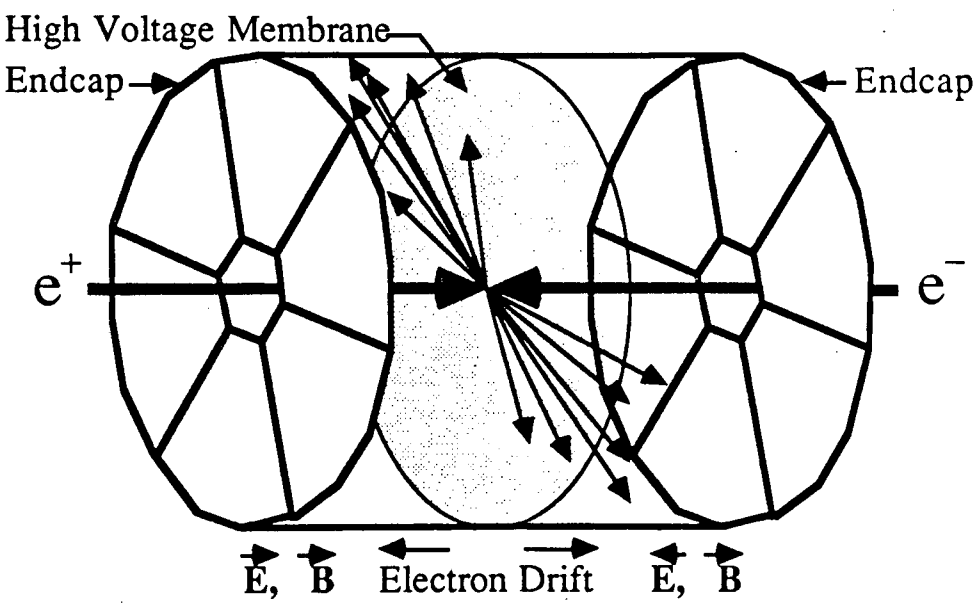

Figure 2: Schematic diagram of the Time Projection Chamber showing the axial electric and magnetic field configurations.

and is 15.6% of a radiation length now.

The magnet coil package is located directly outside the insulator for the large radius field cage at an inner radius of 102.1 cm. Prior to 1984 a conventional coil was used which produced a magnetic field of 3.89 kG. The combination of heat shields, cooling tubes and coil added 1.32 radiation lengths before the electromagnetic calorimeter. In 1984 the conventional coil was replaced by a superconducting coil which produced a magnetic field of 13.25 kG and added only 0.87 radiation length before the electromagnetic calorimeter.

Directly outside the magnet coil is the outer drift chamber [3]. It has three axial layers of proportional wires and extends from a radius of 1.19 m to 1.24 m and is 3 m long, covering 77% of 4π. The gas used is argon-methane (80%-20%) at 1 atm. The outer drift chamber is used for triggering and provides information about photons converting in the coil.

The hexagonal electromagnetic calorimeter [5] outside the outer drift chamber is a 40 layer gas, lead-laminate sampling calorimeter operated in a limited Geiger mode. It is azimuthally subdivided into 6 trapezoidal modules, each 10.4 radiation lengths deep. The length of 4.2 m gives a solid angle coverage of 75% of 4π. Before 1984, the gas used was argon-ethyl bromide (96%-4%) at 1 atm. Unfortunately, a chemical reaction between the ethyl bromide and aluminum crippled two of the six modules. In 1984 the modules were restored and the gas was changed to argon(92.3%)-methylal(5.5%)-nitrous oxide(2.2%) at a pressure of 1 atm. No subsequent problems developed. Sense wires are strung axially in the 6 mm gas gaps with 5 mm wire spacing. The lead-laminates in each layer have aluminum cathode strips at $\pm 60°$ with respect to the wires providing a stereo view of the showers. The measured energy resolution is $\sigma_E/E \simeq 17\%/\sqrt[4]{E}$ (E in GeV) for E below 1 GeV [6]. The energy resolution is degraded at high energies because of the limited thickness (10.4 r. l.) of the calorimeter. For Bhabhas $\sigma_E/E = 14\%$ at 14.5 GeV is obtained.

Behind the end planes of the TPC and in front of the magnet pole-tips are the pole-tip calorimeters [7]. Each pole-tip calorimeter is an electromagnetic calorimeter consisting of 51 layers of lead-laminate and gas with sense wires operating in the proportional mode. The direction of the wires in three consecutive layers are rotated by 60° so as to provide three 60° stereo views of a shower. The gas is 8.5 atm. of argon-methane (80%-20%). Each calorimeter is 13.5 radiation lengths deep and together they cover 18% of 4π. The resolution is $\sigma_E/E = 11\%/\sqrt{E}$ below 10 GeV and 6% for Bhabhas at 14.5 Gev.

Outside the electromagnetic calorimetry is the muon detector system [8]. The central muon detector consists of three layers of drift chambers parallel to the beam direction, followed by a fourth layer of drift chambers at 90°. The drift chambers are made from triangular extruded aluminum tubes. With this geometry, two adjacent wires usually fire resolving left-right ambiguities inherent in most drift chambers. In the barrel region, 30 cm of iron form the return yoke for the magnet and the first absorber layer. The first wire layer is directly outside the iron return yoke. It is followed by a 35 cm iron inner absorber before the second wire layer, and then

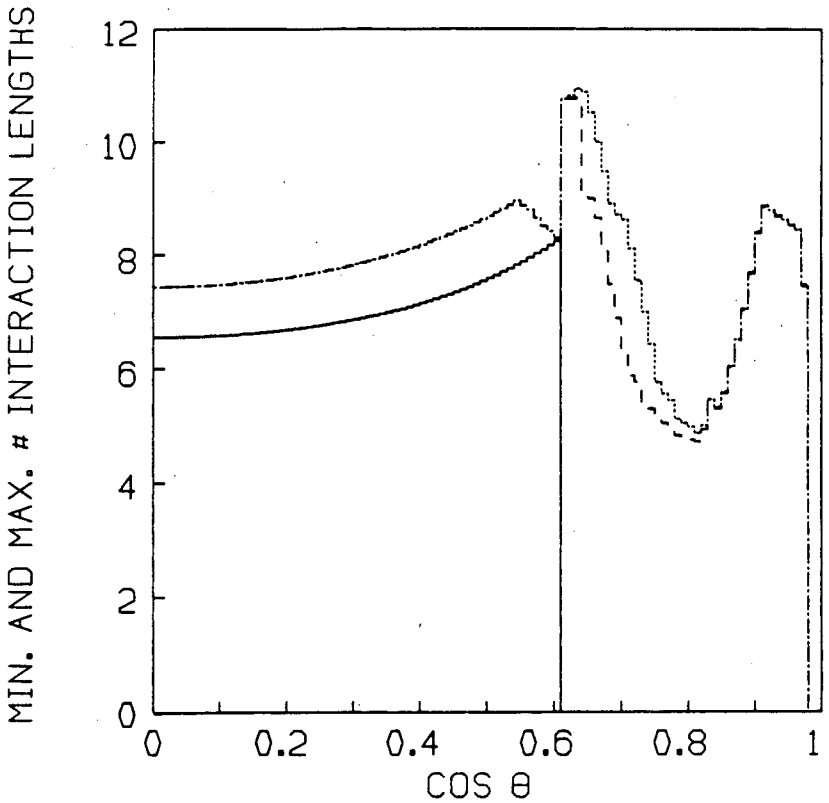

Figure 3: Minimum and maximum number of interaction lengths in the iron over all azimuth as a function of the cosine of the angle with respect to the beam pipe.

a 30 cm iron outer absorber before the third and fourth wire layers (Fig. 1). The wires are operated in the proportional mode with argon-methane gas (80%-20%) at 1 atm. Three layers of these proportional tubes are also placed behind the pole-tips of the TPC giving the muon system a total coverage of 98% of 4π. Fig. 3 shows the minimum and maximum number of interaction lengths in the iron over all azimuth as a function of $\cos\theta$, where θ is the angle with respect to the beam pipe. A coverage map of one octant of the muon detectors is shown in Fig. 4 where the cracks between the barrel and the endcap detectors (lower right), the crack between two barrel detectors (lower left), and the crack between the two halves of the endcap detectors (upper right) are visible. The reduced iron thickness in front of the endcap muon detectors makes them less useful than the central detectors.

Low-angle tracks and photons are measured by forward spectrometers at each end of the central detector. At very small angles (22–90 mrad from the beam) calorimetry is provided by NaI arrays. Each array consists of 60 hexagonal NaI(Tl) crystals of size 6 inches apex to apex and 20 inches (20 radiation lengths) in depth. Light generated by particle shower development is coupled to photomultiplier tubes by means of external lucite rods. Short term monitoring of photomultiplier gain is accomplished using an LED light flasher system. Absolute energy calibrations to

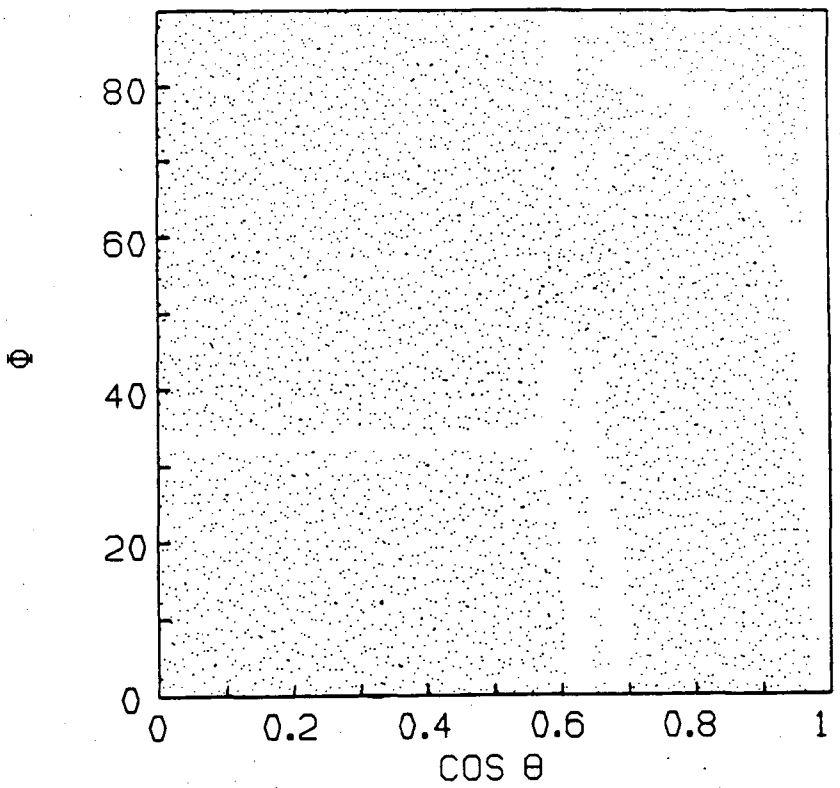

Figure 4: Coverage map of one octant of the muon detector system as a function of azimuth angle and cosine of the angle with respect to the beam pipe. The cracks between two barrel segments (lower left), the barrel and endcap segments (lower right), and the two halves of the endcap detectors (upper right) are visible.

0.3% are obtained using elastic e^+e^- (Bhabha) events. Long term degradation of the energy resolution due to radiation damage required spatial dependent corrections as well. The average energy resolution was measured to be $\sigma_E/E = 1.2\%$ at 14.5 GeV, with a best performance without radiation damage of 0.9%. The position resolution is 4 mm (rms), corresponding to an angular resolution of 0.7 mrad.

Lead-scintillator shower counters provide calorimetry in the angular range 100–180 mrad. Each unit consists of 55 layers of lead sheets interspersed with acrylic plastic scintillator strips for a total depth of about 18 radiation lengths. The scintillator strips are oriented in three directions (horizontal and $\pm 30°$ with respect to the vertical) to measure the position of showers and avoid ambiguities. All strips in consecutive layers with the same orientation are optically coupled to a BBQ-doped wave bar which is viewed by a photomultiplier tube. Short-term monitoring of the system is done with a nitrogen laser coupled to a system of optical fibers while the overall calibration uses Bhabha events. The resulting energy resolution is well-described by the form $\sigma_E/E = A/\sqrt{E}$ (E in GeV). The coefficient A was measured in an electron test beam to be 14% but, due to aging and radiation damage effects, the average value during colliding-beam operation was closer to 20%. The spatial resolution is 7 mm (rms), which corresponds to an angular resolution of 1.1 mrad.

Charged particles are measured in 15 planes of drift chambers which are grouped into the five modules labeled DC1–DC5 in Fig. 1. The chamber wires have orientations of $-5°$, $+5°$ or $90°$ from the vertical. Double sense wires are used to resolve right-left ambiguities and to provide a differential output for common-mode noise immunity. All chambers are run at atmospheric pressure with DC1 using an Ar–Ethane (50%–50%) gas mixture and DC2–DC5 using Ar–CO_2 (83%–17%). The angular acceptance of the drift chambers is 22–180 mrad. A septum magnet produces an approximately vertical field in the top and bottom regions and a quadrupole field at the beam axis. The $\int Bdl$ of the septum magnet is about 0.26 T-m. The momentum resolution of the system at large angles is given by $(\sigma_p/p)^2 \approx (0.026)^2 + (0.008p)^2$ with a position resolution of about 300 μm.

Particle identification in the forward direction is achieved using a combination of techniques. A Cerenkov counter with a 70 cm long, atmospheric-pressure CO_2 radiator covers the angular range 22–180 mrad. Bhabha events were used to map the efficiency of the counter, which is 90% overall and better than 95% over 80% of the acceptance. Momentum thresholds for muons and pions are 3.5 GeV/c and 4.5 GeV/c, respectively. Separation of pions from kaons and protons is the function of the time-of-flight (TOF) counters. Crossed planes of scintillator strips, each of width 8.5 cm, cover the full angular acceptance. The time resolution is 300 psec, which allows a three standard deviation separation of π/K and K/p for momenta less than 1.8 GeV/c and 3.0 GeV/c, respectively. Finally, muons are identified using three layers of drift chambers interleaved with a total of 1 m of iron. The gas is Ar-Ethane ($50\% - 50\%$) and a 220 μm position resolution has been obtained. The system covers about 40% of the forward solid-angle with momentum thresholds for muons of 1 GeV and 3 GeV for penetration to the second and third layer,

respectively.

2.2 The Time Projection Chamber

The primary detector used for this analysis was the Time Projection Chamber. In this section the device itself is first discussed, then the calibration and performance.

2.2.1 Description of the TPC

The Time Projection Chamber (TPC) is a gas filled cylindrical detector which provides 3-dimensional images of tracks from charged particles and which also measures ionization energy loss (dE/dx) [4]. The ionization along a track drifts in an axial electric field to the end planes which are equipped with a large array of proportional wires and position pads. The wire signals provide dE/dx, and radial and axial position information, while the pads provide azimuthal and axial position information. The axial or "z" position is determined from the drift time of the electrons in the electric field. A solenoidal magnetic field bends the tracks so the particle momentum is determined from the position measurements which give the curvature. The simultaneous dE/dx and momentum measurements provide particle identification.

Fig. 2 shows the field configurations in the TPC. The axial magnetic field is produced by the solenoidal coil. The axial electric field is defined by the central membrane at a negative voltage and by the field cage, a series of equipotential rings at the inner and outer radii of the TPC. Prior to 1984 the electric field strength was 75 kV/m resulting in an ionization drift speed of 5 cm/μs. In 1984 the electric field was lowered to 50 kV/m giving an ionization drift speed of 3.3 cm/μs. (Halfway through the data taking the field was raised to 55 kV/m.) Decreasing the drift velocity improved the z position resolution as discussed below.

The detector end planes are divided into 6 sectors, each with 183 sense wires spaced at 0.4 cm and operated in the proportional mode. The amplitude of the signal on a sense wire provides ionization (dE/dx) information, and the timing of the pulse determines the depth of the track in the TPC. Thus the wires give r, z, and amplitude information. Fig. 5 shows the wire configuration of a sector. The drift region and amplification region are separated by a shielding grid. Between the sense wires are wires for field shaping. In 1984 a gating grid was installed. This grid serves to reduce the space charge in the TPC drift volume due to positive ions created in the amplification regions. Only after a (loose) pretrigger condition is fulfilled, the grid is switched into the transparent mode (Fig. 5) and drift electrons can reach the sense wires [10]. By the time positive ions produced in the amplification region drift back to the grid wires, the grid is usually closed and the ions are discharged at the grid wires. The gating grid greatly reduces electrostatic distortions, improving the momentum resolution. Azimuthal information is obtained from induced signals on 15 rows of rectangular cathode pads 0.75 cm high and 0.70 cm wide with spacing of 0.05 cm between pads. The cathode pads are 0.4 cm behind the sense wires (Fig. 5). There are 1152 pads per sector. Fig. 6 shows the relative position of the strips

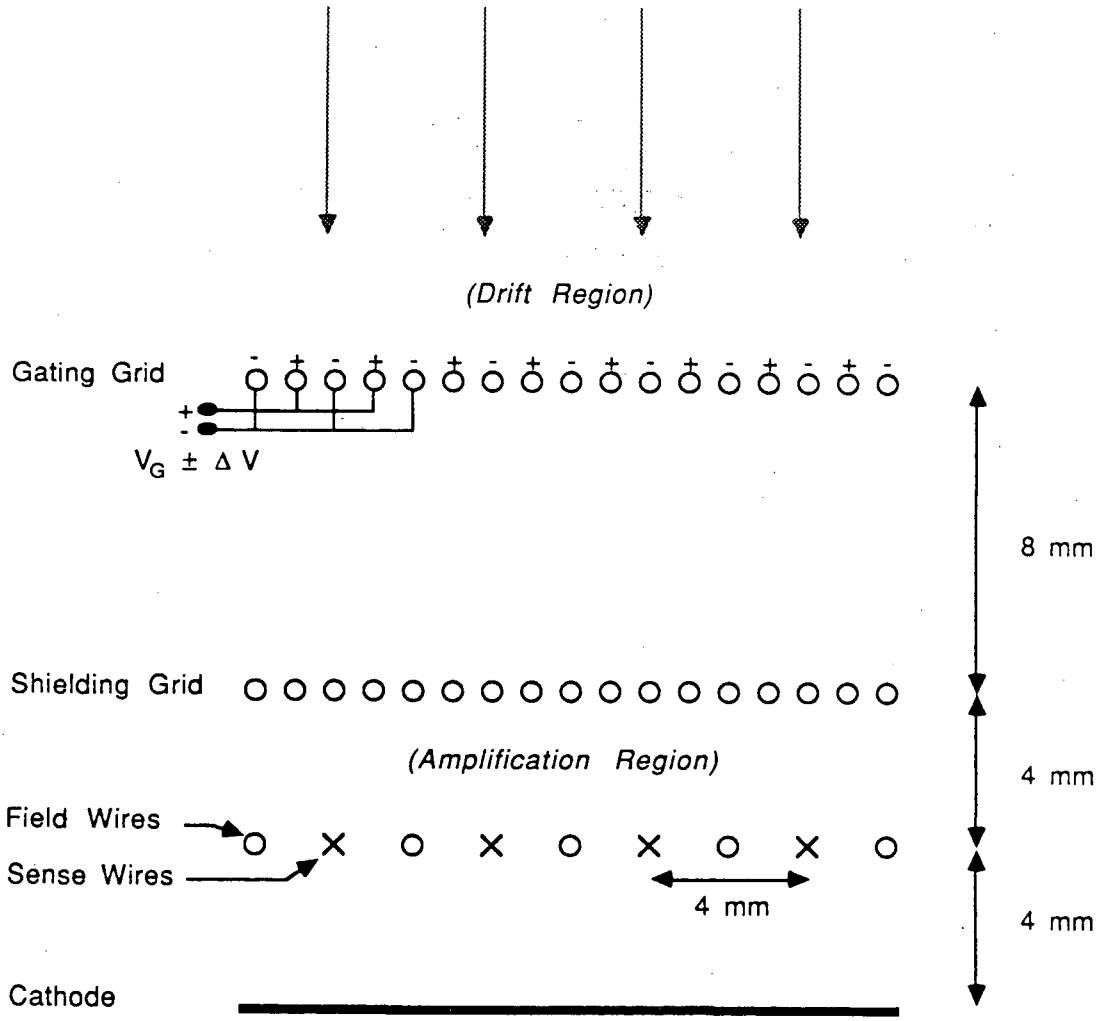

Voltages

Midplane	-55 kV	
Gating Grid	-910 V ± 90 V	*(Opaque Mode)*
	± 0 V	*(Transparent Mode)*
Shielding Grid	0 V	
Field Wires	700 V	
Sense Wires	3400 V	
Cathode	0 V	

Figure 5: Wire configuration of a sector. The sense wires are operated in the proportional mode, and together with the induced signals on the segmented cathode, provide x, y, z, and amplitude information.

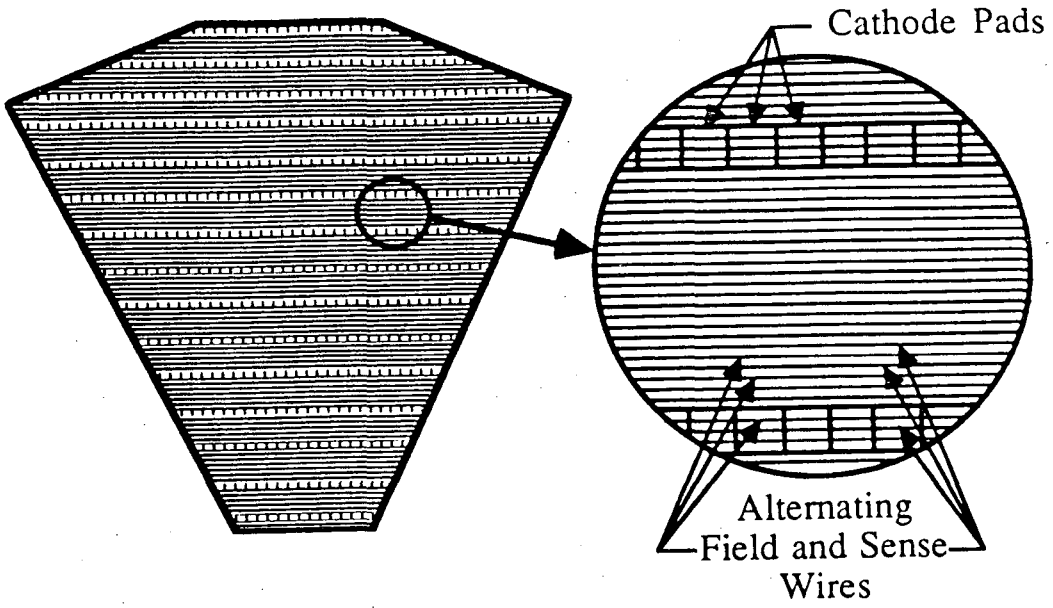

Figure 6: Relative position of the 15 rows of cathode pads.

of cathode pads in a sector. This geometry provides 2 or more 3-d points and 15 or more wire signals per track over 97% of 4π.

The signals on the sense wires and pads are amplified and shaped before being sampled by charge coupled devices (CCD's) which provide pulse height measurements at 100 ns intervals [11]. The CCD's hold a 45.5 μs history (455 CCD buckets). On readout, the CCD clock frequency is changed from 10 MHz to 20 kHz allowing time for the signals in the CCD to be digitized. Each digitized signal is compared to a threshold for that channel stored in a RAM, and is read out to a buffer memory only if it is above the threshold. The shaper amplifiers were designed so an ionization pulse typically has 5 to 7 samples above threshold, thus providing enough information for good time (z) and pulse height resolution.

2.2.2 TPC calibration and corrections

Both tracking and dE/dx determination in the TPC require very precise charge measurements. To achieve the required accuracy for the ionization and spatial position measurements, each channel must provide charge information which is both accurate and stable to better than 1% [12,13]. Several corrections must be applied to the raw pulse-height data from the TPC so it accurately reflects the ionization produced in the TPC volume. The size of a pad or wire signal depends on temperature, pressure, and composition of the TPC gas, the absorption of drift electrons by electronegative impurities, the gas gain as determined by the local geometry of the sense wire and cathodes, and on the transmission and recovery characteristics of the preamp, CCD, and digitizer. In addition, the measurement of the z-coordinate via the drift time requires precise knowledge of the drift velocity

as well as propagation delays in the readout system. Calibration constants related to gas composition or detector temperature are usually time dependent.

The TPC electronics calibration is performed in two stages. First, the pedestal levels are determined by setting the digitizer thresholds to zero and reading out the CCD's. A least squares straight line fit to the measurements gives the pedestal slope (due to leakage currents, the pedestal increases over a full CCD readout by typically 1-2% of a pulse height for a minimum ionizing track) and the rms noise. The second step in the calibration is to measure the shape of the amplifier's gain curve. The shielding grid (see Fig. 5) is pulsed at different voltages with a precision pulser and the gain of the wires and pads is measured and parameterized by an 11 point spline fit.

After a pulse is amplified, the amplifier output undershoots by about 0.5% of the pulse height, lowering the pedestal value for the remainder of the CCD read-in time. This biases any second ionization pulse to a lower value. This effect is corrected, removing an observed dependence of the measured pulse heights on the number of tracks per sector.

Gas gain corrections are done in several steps. An initial calibration determines fixed correction factors (such as for variations in wire diameter) for each wire. Then time varying correction factors for continuously measured quantities (such as for TPC gas temperature variations) are applied on an event by event basis. Finally, run to run corrections are made which account for longitudinal diffusion and electron capture, and all remaining effects.

The calibration is based on a map of the wire gain made before the sectors were installed and on *in situ* corrections to the map. The map of the wire gain was made using an ^{55}Fe line source to determine the relative gain every 4 degrees in azimuth along the wires. These relative gains were shown to be constant as long as the sector was not changed mechanically. The observed fluctuations were on the order of 3% rms due to variations in the diameter of the wire and variations in the distance from the wire to the cathode [12]. In addition, the heat from the wire preamps, in spite of water cooling, caused a 3% increase in the gain in the vicinity of the preamps.

Since the environment of the sectors is different in the detector from that in the test system, the gain maps alone can not be used as a calibration of the gain at the sense wires. *In situ* calibration is necessary. Each TPC sector is equipped with three ^{55}Fe line sources which can be moved pneumatically from behind screens to irradiate the wires. The ^{55}Fe emits monoenergetic 5.89 keV X-rays which ionize K shell electrons in the argon. About 85% of the time an Auger electron is emitted in addition to the primary electron and both travel a distance on the order of microns before loosing their energy by dE/dx. The ionization is collected on a single wire providing the main calibration peak $\sim$ 5.89 keV. The other 15% of the time a photon is emitted which travels about 1 cm resulting in satellite peaks. Corrections to the initial gain maps from this calibration are of order 1-2% [14]. In addition, this data is used to eliminate sector to sector and wire to wire gain variations which are on the order of 15%. The reproducibility of the end plane source measurements has

been extremely good with changes less than 0.3% over periods of six months [12]. The calibration is performed once or twice a month.

Quantities like gas pressure, temperature, and sector voltage which affect the proportional amplification are continuously measured and are read out with each event. Corrections for any changes are made to the data. A 1% change in the sector voltage causes an 18% change in the gain, a 1% change in gas density causes a 9% change in the gain, a 1% change in the CH_4 fraction causes a 10% change in the gain, and a 1 °C change in temperature makes a 3% change in the gain [12]. Changes in the proportional amplification affect dE/dx measurements.

Longitudinal diffusion and electron capture by electronegative contaminants in the gas biases the ionization measurements to lower values for longer drift distances. The effect is typically between 5% and 13% over one meter [14]. This effect is monitored on a run by run basis (i.e. typically once per hour) and is corrected for.

After these corrections, a global dE/dx normalization factor is determined from the data for each run by looking at tracks with momentum between 400 and 600 MeV/c. In this region pions are minimum ionizing and are well separated from kaons and electrons (see Fig. 18). The mean dE/dx value for these tracks (the mean of the truncated means) is corrected to be 12.1 keV/cm (because early theoretical work predicted this value) and other dE/dx measurements are then made relative to this value. dE/dx measurements are discussed further in section 4.1.

In addition to the run to run corrections to the ionization measurements, there are also corrections that have to be made on a track by track basis. For example, when determining dE/dx, the amount of ionization per unit track length is required, so the effects of dip angle (the angle between the track and the midplane) must be included. The track length sampled by each wire increases with dip angle. Also, the truncated mean ionization per unit track length depends on the logarithm of the length of the track sample. The dip angle correction includes this "log(length)" effect. After these corrections are made, the dE/dx of minimum ionizing pions is plotted as a function of time, azimuth, and dip angle. Any remaining dependence on these variables is removed with *ad hoc* corrections which are typically less than 3% [15].

A final quantity that must be accurately known is the drift velocity since it affects the z position resolution. The most accurate method for determining the drift velocity comes from measuring the z positions of the two tracks in Bhabha events tagged by the hexagonal electromagnetic calorimeter. The drift velocity was determined on a run to run basis during the data taking (i.e. about every hour). The variation in drift velocity over the entire running cycle was around 7%, and the drift velocity was determined to 0.03%.

2.2.3 Position measurement in the TPC

The 15 pad rows on each sector provide x-y position measurements for up to 15 points along a track. Signals are induced on a given pad from the five wires nearest the pad, and an avalanche on a given wire induces signals on either two or three

pads. The x position (along a pad row) is found by assuming a Gaussian response of the pads. For 40% of the measurements, three pads are above threshold and the width of the Gaussian can be determined by a fit. If only two pads are above threshold, the measured average width (as a function of drift distance and track angle) is used as input to the x position calculation.

The y position (perpendicular to the pad row) is calculated as the average position of the five wires that contribute to the pad signals, weighted by their pulse heights and coupling to the pad. This method reduces the effects of ionization fluctuations.

The z position of a spatial point is given by the average of the z positions determined by the pad signals. On any individual pad, an arriving pulse is shaped and sampled by the CCD. In the analysis, the samples are used to reconstruct the pulse and the position of the peak determines the arrival time. The z position is given by the product of the arrival time and the drift velocity.

After the 15 or so spatial points on a track have been reconstructed, corrections are made for known electrostatic distortions. Positive ion distortions affect the position measurement at small radii (the first 2-3 pad rows). In the older data set their magnitude was on the order of 1 cm. However, with the addition of the gated grid, they were negligible in the newer data set. Local electrostatic distortions caused by charge buildup on the field cages affect both the first and last pad rows. Their size is on the order of 1-2 mm for both the old and new data sets. Distortions from large scale electric field irregularities in the volume of the TPC are on the order of 1 mm for both the old and new data sets.

Since pulse heights are used to find position, factors determining the position resolution are the electronics calibration, electronic noise, diffusion in the 1 m drift distance, and ionization fluctuations [16]. A further factor is an $\vec{E} \times \vec{B}$ effect near the sense wires. This affects the resolution through a transverse force due to the fact that the electric and magnetic fields are no longer parallel.

The x-y position resolution is plotted in Fig. 7. For the newer data set, we assign a floor of 85 μm to the x-y position resolution, the largest contribution coming from the uncertainty in the calibration of the electronics gain. Electronic noise contributed 62 μm to the resolution with an rms variation of 25 μm depending on the position and orientation of the track with respect to the pad row. The floor and noise contributions can be added in quadrature resulting in a fixed error of 105 μm. The x-y position error from transverse diffusion is proportional to $L^{\frac{1}{2}}$, $P^{-\frac{1}{2}}$, and $(1+(\omega\tau)^2)^{-\frac{1}{2}}$, where L is the drift distance, P is the pressure, ω is the electron cyclotron frequency, and τ is the mean electron collision time. For a one meter drift the error averaged over azimuth is 64 μm with an rms variation of 8 μm. Ionization fluctuations contribute an error which varies strongly with azimuth, as does the error due to $\vec{E} \times \vec{B}$ effects. To illustrate this, consider a track whose projection on the end plane makes an angle α with respect to the normal to the wires. If $\alpha \neq 0$, an ionization fluctuation on one of the five wires contributing to the two or three pad signals will bias the pad response to larger values near the fluctuation. This will

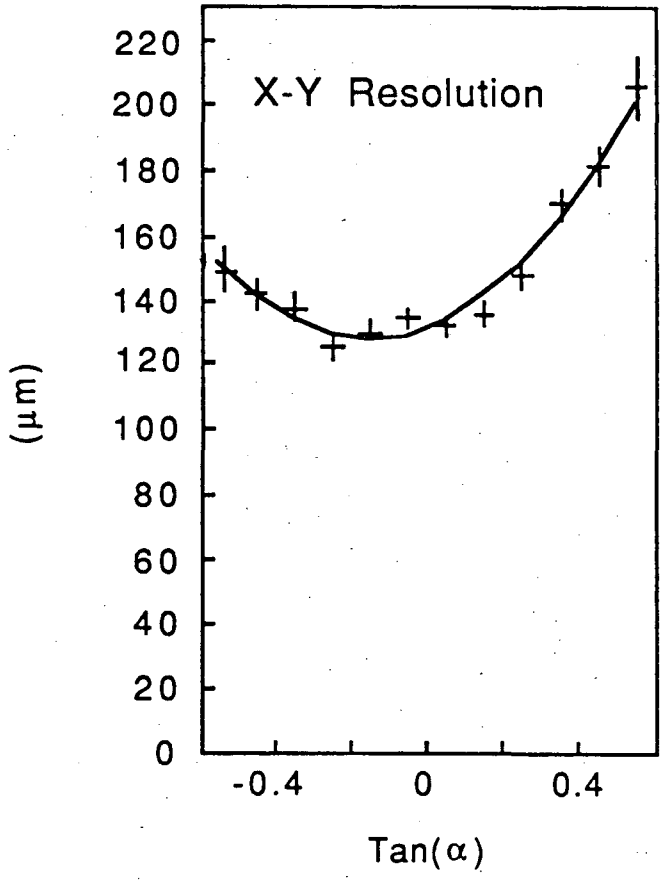

Figure 7: Position resolution σ_{xy} as a function of the tangent of the azimuth angle α.

shift the measured x position. Weighting the five wires with their pulse heights to determine the y position partially compensates for this. The error is proportional to $\tan(\alpha)$. In addition, the x-y resolution is affected by the $\vec{E} \times \vec{B}$ force near the wires, the main effect of which is to shift the angle at which the resolution is minimum. Ionization fluctuations and the $\vec{E} \times \vec{B}$ effect contribute to the resolution about 200 μm at $+30°$ and 100 μm at $-30°$. All effects are combined in Fig. 7 which shows the x-y position resolution as a function of $\tan(\alpha)$ over a sector ($-30° < \alpha < 30°$). The non-symmetric shape is due to the $\vec{E} \times \vec{B}$ effect.

For comparison, in the older data set the fixed position error was about 160 μm, the error from transverse diffusion was about 105 μm (for a 1 m drift), and the error from ionization fluctuations was about 250 μm. The $\vec{E} \times \vec{B}$ effect was not important with the lower magnetic field strength. The 1984 electronics calibration improvement is largely responsible for the smaller fixed position error in the newer data set. The increased magnetic field strength is responsible for limiting transverse diffusion, giving a smaller error from this contribution.

The position resolution in z is determined by the uncertainty in the arrival time of an ionization pulse, the drift velocity, and the t_0 calibration. The main factors that contribute to the uncertainty in the arrival time of an ionization pulse are the CCD sampling rate, ionization fluctuations, electronic noise, and longitudinal diffusion. Under present conditions, the CCD sampling rate gives the largest contribution. Since the CCD sampling rate did not change in 1984, the uncertainty in the arrival time of a pulse did not change significantly. However, the decrease in drift velocity improved the z position resolution proportionally, from 340 μm to 200 μm (averaged over dip angles).

The measured z position resolution as a function of dip angle is shown in Fig. 8. The z position resolution depends strongly on the dip angle (angle with respect to the midplane) of a track since the ionization pulse broadens with dip angle enhancing the effects of ionization fluctuations and electronic noise.

2.2.4 Momentum measurement in the TPC

The momentum of a charged particle in the TPC is determined by first fitting an orbit to the measured spatial points, taking into account the energy loss along the track. The inner and outer drift chambers are not used in the fit. A vertex fit then constrains the orbits to go through a common origin, consistent with the beam position. Only those tracks are included in the vertex fit which do not raise the global χ^2 of the fit by more than 30. For tracks included in the vertex fit, the result of this constrained fit is used in the analysis. Note that since the TPC measures true space-points, three points or two points and the common vertex are sufficient to measure the momentum of a particle.

The error on the momentum has two contributions: position measurement errors and multiple scattering. The drastic reduction of beam related electrostatic distortions for the second data sample resulted in much smaller position measurement errors on both the inner and outer pad rows, essentially adding two points to

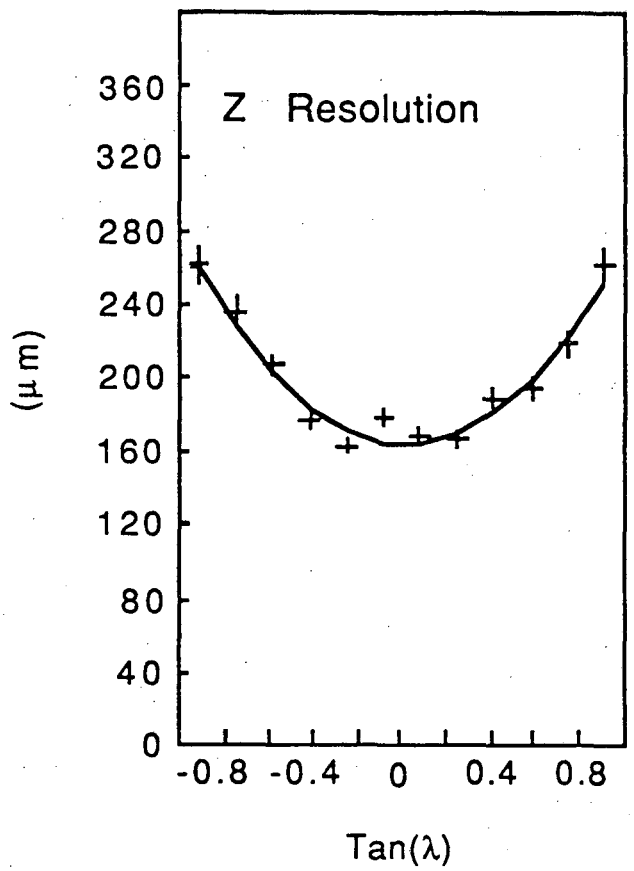

Figure 8: Position resolution σ_z as a function of the tangent of the dip angle λ.

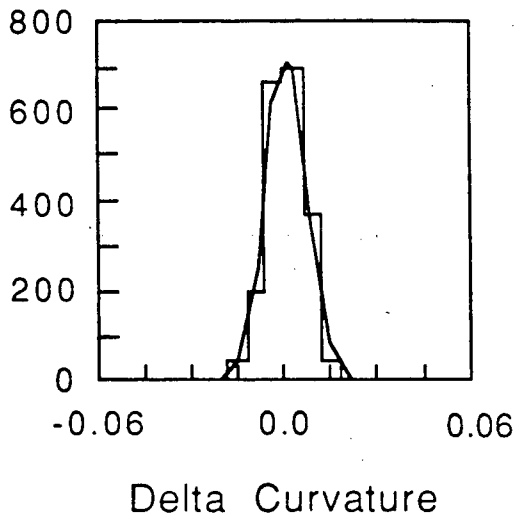

Figure 9: Distribution of curvature difference for cosmic rays as measured in two different sectors.

the track fit. In addition, the improved position resolution reduced the component of the momentum uncertainty due to measurement errors. Increasing the magnetic field in the TPC from 3.89 kG to 13.25 kG improved both the measurement and multiple scattering components of the momentum resolution by the ratio of the field strengths. The measured momentum resolution was $(\sigma_p/p)^2 = (0.06)^2 + (0.035p)^2$ prior to 1984, and at present is $(\sigma_p/p)^2 = (0.015)^2 + (0.007p)^2$ (p in GeV/c) for the fit with the vertex constraint. Without the vertex constraint, the measurement error contribution to the momentum resolution increased from $0.035p$ to $0.06p$ in the first data set, and from $0.007p$ to $0.011p$ (p in GeV/c) in the second data set.

The measurement error component of the momentum resolution was determined by comparing the curvature of cosmic rays as measured in two opposite sectors. A constraint that the two halves of the track meet at a common vertex was imposed. The distribution of the curvature difference is shown in Fig. 9 for the new data. A Gaussian fit gives

$$\frac{\sigma_p}{p^2} = 0.007\,(\mathrm{GeV/c})^{-1}.$$

This value was checked with Bhabha and $\mu^+\mu^-$ events where the momenta of both particles is 14.5 GeV (broadened by bremsstrahlung). Fig. 10 shows the curvature distribution for particles in Bhabha events. The peaks for positive and negative particles are separated and symmetrical around zero curvature. The width of the peaks correspond to a momentum resolution consistent with the cosmic ray result.

The quoted multiple scattering contribution to the momentum resolution is calculated using the formula in Gluckstern [17].

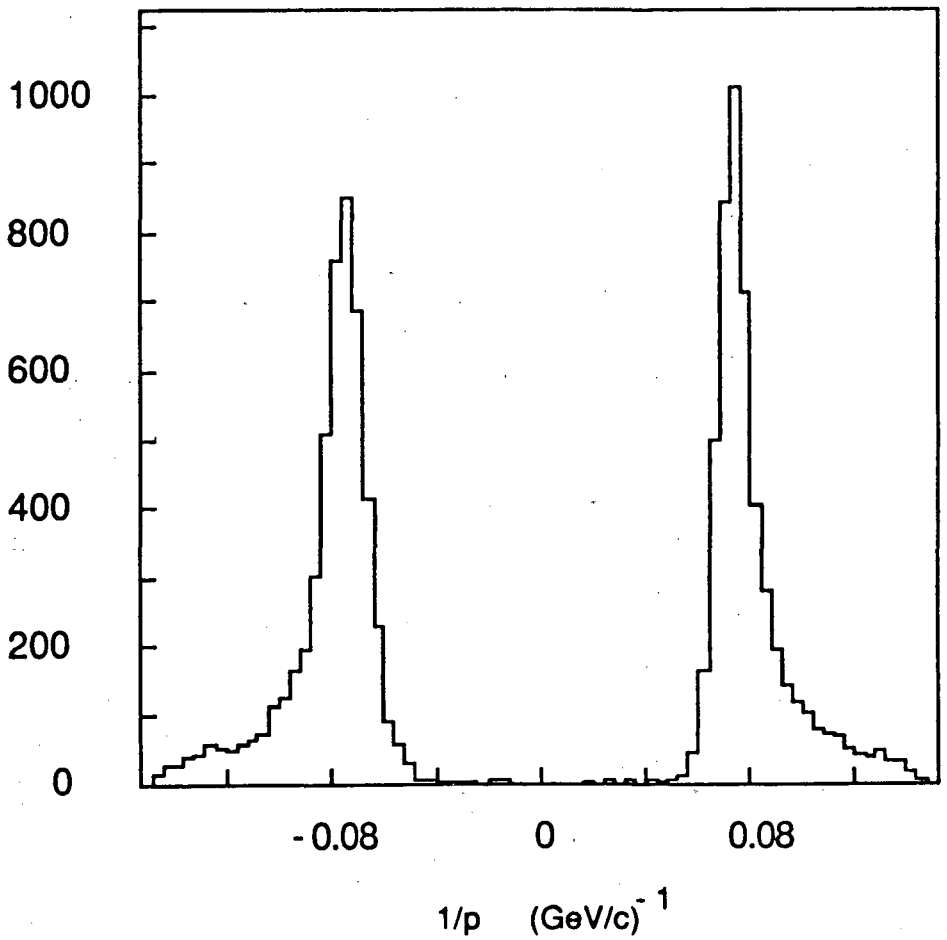

Figure 10: Curvature distribution for tracks in Bhabha events.

2.3 Trigger

The trigger system [18] for the TPC/Two-Gamma facility uses information from the drift chambers, the TPC, and the calorimetry, and is designed to provide high efficiency not only for annihilation events, but also for low-multiplicity two-photon reactions. The trigger for the newer data set is composed of three parts: a pretrigger which selects events of interest within the beam crossing time and turns on the TPC gated grid, a second level trigger used for fast digital decisions, and a final hardware trigger based on a limited pattern analysis. The trigger for the older data set was similar, but simpler because the gated grid was absent. Only the trigger for the newer data set will be described. The PEP beam crossing time is 2.44 μs, and the ionization drift time from the midplane to the endcap of the TPC is about 30 μs with 3.3 cm/μs drift velocity.

The main categories of pretriggers were: (i) central detector charged particles, using prompt signals from tracks passing through an endcap of the TPC and from the IDC and ODC; (ii) energy of more than 250 MeV deposited in the pole-tip calorimeters (PTC) or in the hexagonal electromagnetic calorimeter (HEX); and (iii) forward detector tag-candidates (scattered electrons or positrons in two-photon reactions with at least one highly-virtual photon), based mainly upon energy deposits in the NaI or lead-scintillator shower counters (with effective thresholds of approximately 3 and 5 GeV, respectively). Beam crossings of possible interest were selected within 1.8 μs, leaving about 600 ns for clearing the analog systems if no pretrigger was generated. At a luminosity of 2×10^{31} cm^{-2}s^{-1}, the pretrigger rate was about 1.5 kHz, corresponding to a trigger decision dead time of about 1.6%.

In the event of a pretrigger, the second level trigger was formed within an additional 7.5 μs in the same manner as the pretrigger, but with somewhat tighter requirements. In addition to information from the calorimeters and drift chambers, the second level trigger used the first 10 cm of drift information from the TPC to efficiently find small angle tracks. For a luminosity of 2×10^{31} cm^{-2}s^{-1}, the second level trigger rate was about 500 Hz, corresponding to a trigger decision dead time of about 2.0%.

If a second level trigger was generated, the final trigger used the TPC wire signals to search for continuous tracks coming from the beam crossing position to form a charged particle trigger in about 35 μs, limited by the ionization drift time. These TPC tracks could be defined over 85% of 4π. The primary trigger used for multi-hadron annihilation physics and untagged two-photon physics required at least two such TPC tracks in separate sectors, while the primary trigger used for singly-tagged two-photon physics required at least one TPC track in addition to the forward tag.

Additional charged and neutral particle triggers were generated. These included the following: A double-tag (two-photon physics) trigger required forward tags on opposite sides of the interaction point and a minimal indication of activity in the IDC, PTC, or HEX. An energy deposition trigger was defined by having either at least 2 GeV of energy deposition in the HEX; or at least 1 GeV of energy deposition

in the PTC (with two clusters required); or energy in two or more calorimeter modules, each with more than 0.7 GeV. A charged+neutral trigger was formed if there were one or more charged tracks in the TPC and minimum energy of about 700 to 1300 MeV in the HEX and 2 to 4 GeV in the PTC. A single tag+neutral trigger required a forward tag and minimum PTC or HEX energy of about 300 to 1000 MeV. All triggers involving forward tags were vetoed by the occurrence of back-to-back NaI hits, a signature for Bhabha scattering into the NaI. Calibration and random beam crossing triggers were also used.

In the event of a final trigger, all detectors were read out, requiring about 80 ms. At a luminosity of 2.0×10^{31} $cm^{-2}s^{-1}$, the final trigger rate was approximately 2 Hz, resulting in a total electronics dead time of about 20%. The trigger efficiency for multihadronic events is larger than 99%.

3 EVENT RECONSTRUCTION, SELECTION, AND SIMULATION

This section describes the method used to reduce the data samples of 77 pb^{-1} taken in the 1982/83 running cycle and 68 pb^{-1} taken in the 1984/86 running cycle to data summary tapes. A further event selection was used for this analysis and it is also described. Finally, because of its importance in the analysis, the Monte Carlo program used for event simulation is discussed.

3.1 Event reconstruction

The events which trigger the TPC are reconstructed in an iterative procedure. After the application of calibration constants to determine pulse heights and drift distance, a pattern recognition algorithm finds approximate orbits. The resulting knowledge about the direction of a track crossing a pad row is used to determine second-order, orbit dependent corrections. These corrected points are used in the final fits.

The first step in analysing an event is to find the spatial points in the TPC volume from the corrected sense wire and pad signals. Fig. 11 shows the signals on three neighboring pads as a function of CCD sample number. The signal from each channel is first examined as a function of CCD sample number, and contiguous samples are combined to give an arrival time and pulse height by fitting the three largest samples to a parabola. The arrival time is corrected for the relative timing of the CCD clock with respect to the beam crossing. The z position where the ionization originated is then calculated using the measured drift velocity. The pulse height is corrected using the electronics calibration. Spatial points are then roughly found by searching for contiguous pads with signals roughly at the same z. The x position along the pad row is given by the average of the pad positions weighted by the pulse heights, and the y position perpendicular to the pad row is set to the centerline of the pad row. The z position is the weighted average of the z positions of the individual pad signals. Track finding algorithms connect the rough spatial points to form a first order set of tracks in the event. This is done online.

The track finding program for high multiplicity events makes histograms in $\sin\lambda$ (λ is the dip angle with respect to the midplane) of the spatial points for each sector. For each bin in the histogram, the program chooses test points starting at the outer radius and moving inward. For each test point, it goes through the other points in the bin and makes a histogram of the sagitta of the circle that goes through the origin. Peaks in the histograms are taken as track candidates. The points in the peaks are then fit to a helix. Any points causing large residuals are excluded. In the end, a clean up procedure combines pieces of the same track together and adds points that had not been found before. The procedure is around 98% efficient at finding tracks which traverse many pad rows, and around 50% efficient at finding short tracks which traverse only three pad rows.

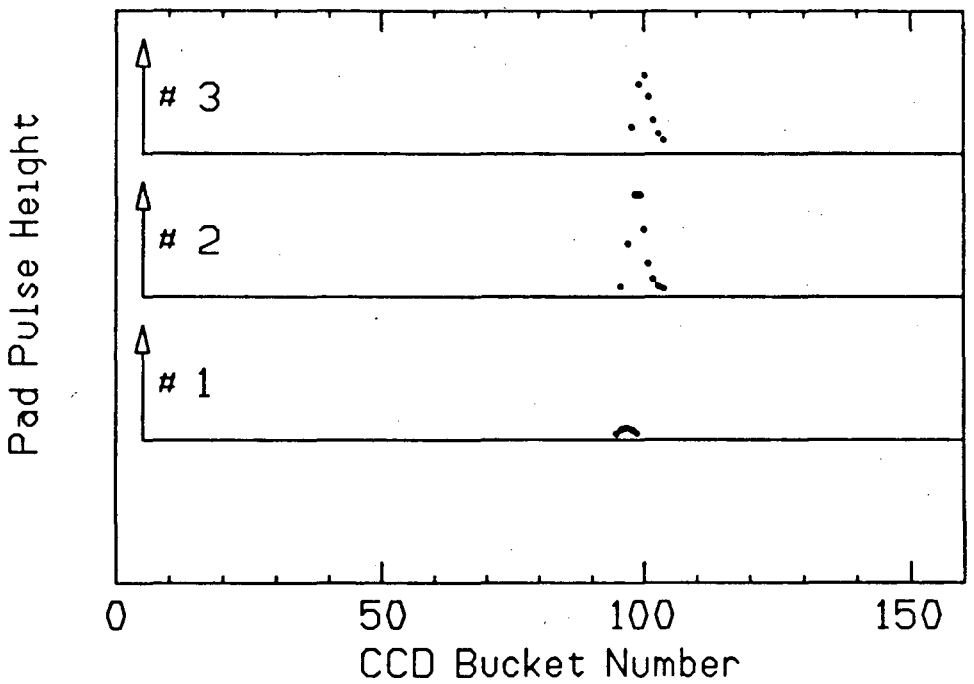

Figure 11: CCD samples above threshold from three pads.

At this stage, time-dependent correction factors are determined from the data and updated. The beam-beam interaction point is measured as the average of the fitted event vertices. The drift velocity is measured by monitoring the endpoint of the ionization arrival time distribution. Gas gain at the sense wires is monitored using the dE/dx of minimum ionizing pions. Also, electrostatic distortions are monitored using the residuals of points in the track fits. Those corrections are averaged over an event sample (typically a 1 hour run) and are then applied in a second-pass, offline analysis.

In the next stage of the analysis, wire signals are associated with all tracks previously found using pads. A wire signal is associated with a track if its z position is within 0.7 cm of the original fitted track (1 cm in the older data set because of the increased drift velocity). However, a wire is excluded if the track to be associated with it is ambiguous, or if the pulse height is uncertain for some reason (if there is a neighboring large pulse which could cause crosstalk, or if there is another wire hit close in time which would affect the electronics). 65% of the tracks have 80 or more wire signals associated with them. The wire signals are used to determine the particle's dE/dx, as discussed in section 4.

The wire pulse heights and track information are used to refine the pad space points. The x position along the pad row is determined by a Gaussian fit to the pad signals, and the wire signals are used to find the y position, perpendicular to the pad row. Tracks are then refit to the refined space points. These refined tracks are used in the final fit which constrains all tracks to come from the event vertex.

Fig. 12 shows a typical multihadron event in the TPC from the 1984/86 data set. The reconstructed tracks have been labeled with a letter or number at each measured point. In the side view all points have been rotated about the beam axis to lie in a plane.

3.2 Multihadron event selection

After the event reconstruction, a selection is made to separate multihadron events. (Tagged and untagged two-photon events go through two separate selection and analysis chains.) The criteria for an event to be part of the standard multihadron event sample are discussed below.

The tracks used to select multihadron events are "good tracks" which pass the following cuts. (1) The angle of the track with respect to the beam pipe must be larger than 30° to ensure that the track is in the fiducial volume of the TPC. (2) The error on the measured curvature of the track must be less than 0.3 $(\mathrm{GeV/c})^{-1}$ or the curvature error has to be less than 30% of the curvature. This is to ensure a good momentum determination. (3) The measured momentum in the TPC of the particle must be larger than 0.10 GeV/c to remove particles coming from nuclear interactions in the material in front of the TPC. (4) The measured vertex momentum (ie. the momentum in the TPC corrected for energy loss in the material before the TPC) must be larger than 0.12 GeV/c. (5) The extrapolated origin of the track

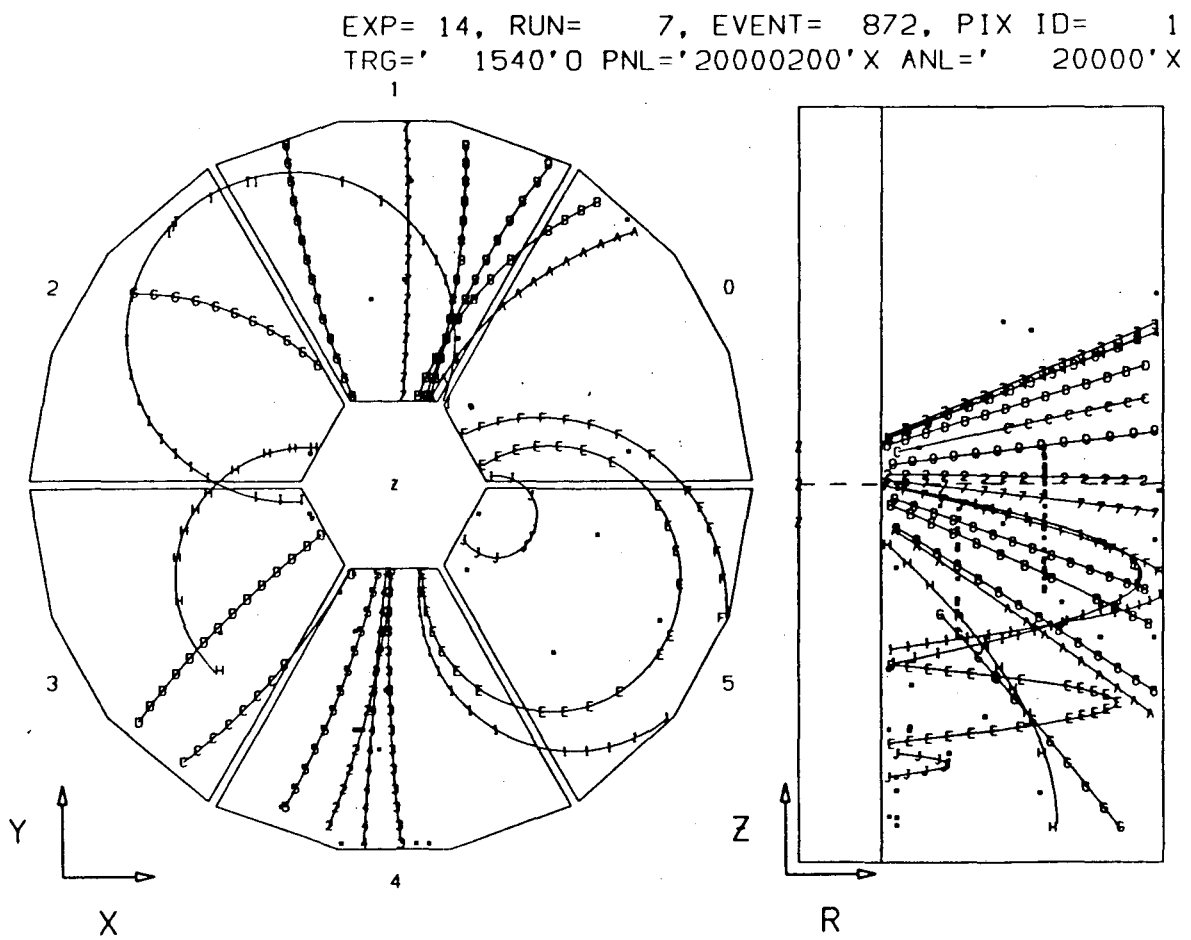

Figure 12: Typical multihadron event in the TPC from the 1984/86 data set.

must be within 6 cm in the x-y direction, and 10 cm in the z direction (along the beamline) of the nominal vertex. This is to eliminate tracks not associated with the event such as those from cosmic rays and also some tracks produced by interactions in the material before the TPC.

The "good tracks" defined above are used to select multihadron events. To be considered a multihadron event, an event must meet the following criteria. (1) The event must have at least five good tracks in the TPC which are determined to be non-electrons either by dE/dx or by a pair finder program which geometrically reconstructs conversion pairs. The restriction to non-electrons is to eliminate Bhabha events where the electron or positron showered in the material in front of the TPC. (2) The observed energy of charged particles, E_{ch}, has to exceed 7.25 GeV. This cut is used to eliminate 2-photon events. (3) The net momentum along the beam pipe of the charged particles must be less than 40% of E_{ch}/c. This cut eliminates events with large initial state radiation and also reduces contamination from two-photon events. (4) The majority of the tracks in the event have to be good tracks in the sense defined above. (5) To reject τ events two hemispheres along the jet axis are constructed. In at least one hemisphere the event must have more than three charged tracks, or the invariant mass of the charged particles in the hemisphere must be larger than 2 GeV. (6) The reconstructed vertex of the event must be within 2.0 cm in x-y and 3.5 cm in z of the nominal vertex.

With these standard multihadron event selection criteria, contamination is estimated to be $0.4 \pm 0.1\%$ from $\tau\overline{\tau}$ events, $0.5 \pm 0.1\%$ from two-photon events, and less than 0.1% from beam gas events and Bhabha scattering.

For this analysis, not all the "good tracks" of the standard multihadron event sample were used. Only those that met the following additional criteria were accepted. (1) The error on the measured curvature of the track had to be less than 0.15 $(\mathrm{GeV/c})^{-1}$ or the curvature error had to be less than 15% of the curvature. (2) The measured momentum of the particle had to be larger than 0.15 GeV/c. (3) The extrapolated origin of the track had to be within 3 cm in the x-y direction, and 5 cm in the z direction of the nominal vertex.

To be considered for this analysis, an event from the standard multihadron event sample still had to have 5 or more good tracks as defined in the preceding paragraph. In addition, it was required that the polar angle of the event axis with respect to the beam pipe had to be larger than 45°. This was done to ensure that a large majority of the particles in each event were in the fiducial volume. For the older data set 21434 events survived these cuts, and 20270 events survived in the newer data set.

3.3 Event simulation

Monte Carlo event simulation is essential in understanding detector performance. The TPC group uses two Monte Carlo detector simulations, a full simulation which generates raw data for all detectors, and a simulation designed for speed, the Fast

Monte Carlo, which generates space points and fits them producing DST output. For determining the acceptances and particle misidentification probabilities needed for this analysis, the Fast Monte Carlo was used because high statistics were needed.

The Fast Monte Carlo [14] uses a physics generator (Lund, Webber, ...) to produce input events. Initial state radiation is simulated using the program of Behrends and Kleiss [19]. The event vertex is chosen in accordance with the PEP beam size. Both charged and neutral particles are tracked through the detector and long lived particles are allowed to decay in the detector volume. Pad hits are generated for charged particles in the TPC and a fit to the points gives the particle's momentum. A dE/dx value is calculated. The output is written in the standard DST format with an additional block containing information about the generated event.

The Fast Monte Carlo models the TPC as a series of discrete layers, each of uniform density. The beam pipe, pressure wall, inner drift chamber, and field cage each constitute a single layer, as does the full distance between pad rows in the TPC. Charged and neutral particles are tracked from layer to layer. The effects of energy loss, multiple scattering, bremsstrahlung, decay in flight, and nuclear interactions are included for charged particles. Neutral hadrons can interact in material and photons can convert to e^+e^- pairs. Pad hits are generated for charged particles at the appropriate layers by smearing the tracked position with a resolution function that includes the effects of diffusion, dip angle, electrostatic distortions, and the electronics. Inefficiencies due to missing electronic channels, sector boundaries, and track overlap are included.

Individual wire hits are not generated. Rather, a particle's dE/dx is calculated using its average $\beta\gamma$ in the TPC, and then smeared. The dE/dx resolution used for the smearing is the measured resolution depending on the number of wires and the dip angle (section 4.1). In determining the number of wires, effects of sector boundaries, track overlap, and missing electronics channels are included, in addition to the TPC geometry.

Pattern recognition in the Fast Monte Carlo is done using a simple algorithm for speed. Measured pad space points within 1 cm of a track are associated with that track, and any track with 3 or more space points is assumed to be found. Ambiguous space points are assigned to only one track. A vertex constrained fit giving the particle momenta is performed in a manner equivalent to the real data analysis.

In the region within the cuts used for this analysis, the Fast Monte Carlo agrees with the experimental data very well, as illustrated in Fig. 13.

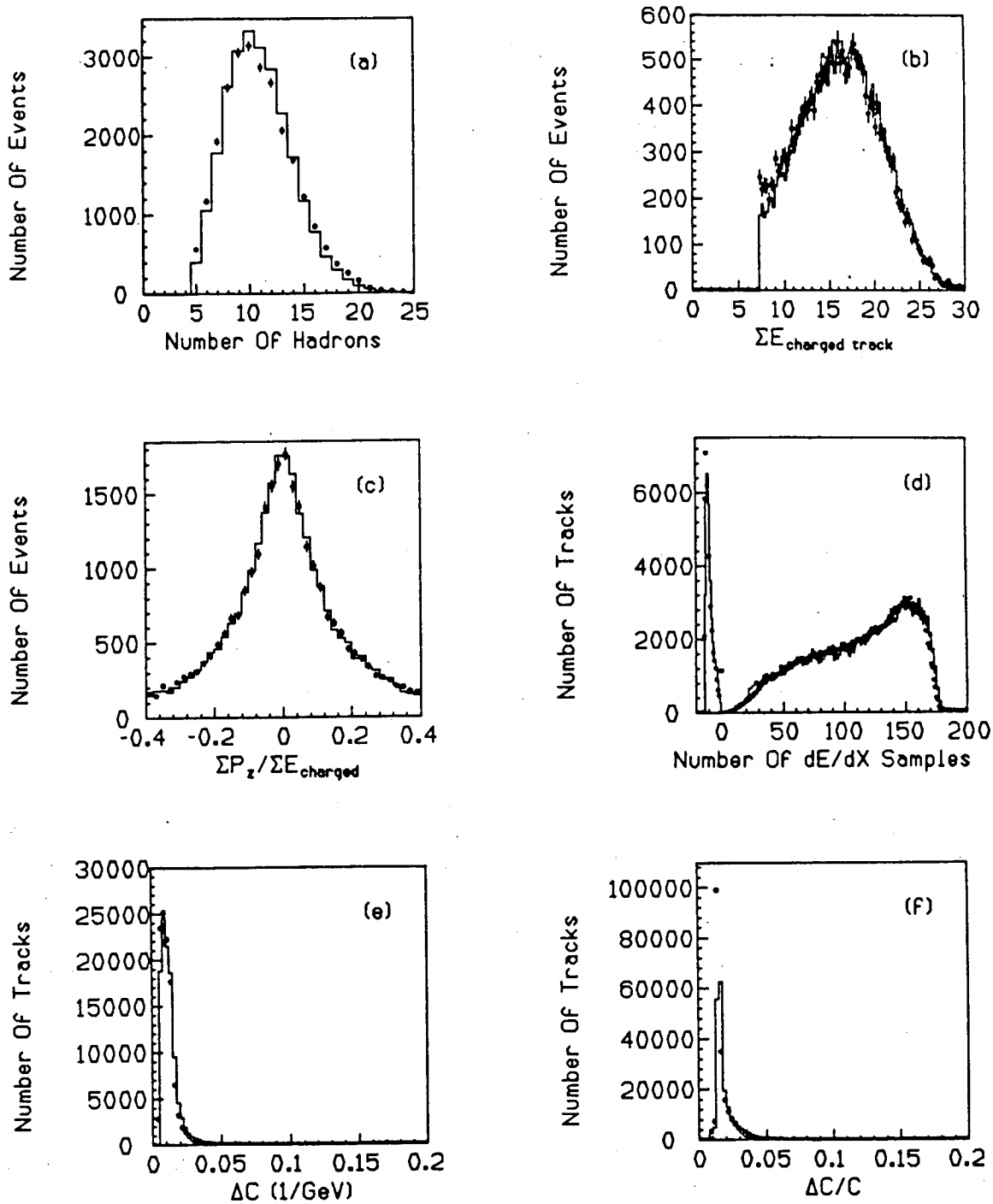

Figure 13: Comparison between the data (points) and the Fast Monte Carlo (histogram).
(a) The number of charged hadrons. (b) The sum of the energies of good tracks. (c) The momentum balance ($\sum p_z / \sum E$) along the beam direction. (d) The number of dE/dx samples along a track. Negative numbers indicate pads were used in the dE/dx calculation rather than wires due to track overlap. (e) The curvature error ΔC for tracks with $p > 1$ GeV/c. (f) The relative curvature error $\Delta C/C$ for tracks with $p < 1$ GeV/c.

4 PARTICLE IDENTIFICATION BY dE/dx

4.1 Theory and measurement of ionization energy loss in the TPC

Effective particle identification by dE/dx requires the precise knowledge of the expected ionization energy loss as a function of particle mass and momentum. For the TPC analysis, the velocity dependence of the energy loss is taken from a rather detailed theoretical calculation, to which small empirical corrections are applied for best agreement with the data. The calculations were heavily based on the work of Lynch [20], Lapique and Piuz [21], Allison and Cobb [22], and Talman [23].

The cross section $d\sigma/dE$ for an incident particle to lose energy E in a collision with an atom of a gas is approximated by [22]

$$\frac{d\sigma}{dE} = (\frac{d\sigma}{dE})_{resonance} + (\frac{d\sigma}{dE})_{Rutherford}$$

where

$$(\frac{d\sigma}{dE})_{resonance} = \frac{\alpha}{\beta^2\pi}\frac{\sigma_\gamma(E)}{EZ}\ln\frac{2mc^2\beta^2}{E\sqrt{(1-\beta^2\epsilon_1)^2+\beta^4\epsilon_2^2}}$$

$$(\frac{d\sigma}{dE})_{Rutherford} = \frac{\alpha}{\beta^2\pi}\frac{1}{E^2}\int_0^E \frac{\sigma_\gamma(E')}{Z}\,dE'.$$

In these expressions $\sigma_\gamma(E)$ is the photoabsorption cross section for a photon of energy E, β is the incident particle's velocity, Z is the atomic number of the atom, m is the electron mass, α is the fine structure constant, and ϵ_1 and ϵ_2 are the real and imaginary parts, respectively, of the dielectric constant of the gas which can be expressed as a function of the photoabsorption cross section. For notational convenience, the gas is assumed monatomic, but the extension to mixtures is straightforward. A term representing Cherenkov radiation has been ignored since it is small in the TPC. The first term labeled *resonance* depends on $\sigma_\gamma(E)$ and is large at the ionization thresholds. The important feature of this term, however, is the logarithmic β dependence which allows relativistic particle identification. The *Rutherford* term represents the contribution from hard scattering off electrons. In the regions of E near the photoabsorption peaks, the Rutherford contribution to the cross section is smaller than the resonance contribution. However, at large E where $\sigma_\gamma(E)$ is small, the Rutherford term is the larger since it depends on $\int_0^E \sigma_\gamma(E')dE'$. This gives a $1/E^2$ tail to the cross section. The expression for $d\sigma/dE$ shows that the Rutherford scattering term with $1/\beta^2$ velocity dependence will be of little use in distinguishing relativistic particles with $\beta \simeq 1$. Thus, to determine velocity, resonant energy loss must dominate dE/dx, not hard Rutherford collisions. This is achieved in practice by sampling the energy loss in thin layers of the gas, so that in any layer the probability of a Rutherford scatter is small.

Atom	Level	w_i	E_i	s_i	E_{eff}
Ar	K	0.111	3206.	2.75	5341.
Ar	L	0.444	248.	2.29	490.
Ar	M	0.133	52.	3.20	82.
Ar	M	0.311	15.8	3.20	25.
CH_4	-	0.8	11.5	2.15	27.
CH_4	K	0.2	283.	2.52	506.

Table 2: Table of energy levels and relevant data used in the dE/dx calculations.

The average number of interactions resulting in energy loss E in dE per unit path length dx is given by

$$\frac{d^2N}{dxdE} = n\frac{d\sigma}{dE}$$

where n is the number density of atoms in the gas. This expression yields the average number of interactions per unit length

$$\frac{dN}{dx} = \int n\frac{d\sigma}{dE}dE.$$

The actual number of interactions per unit path length $d\mathcal{N}/dx$ is distributed according to a Poisson distribution with mean value dN/dx.

A Monte Carlo program was written [14] to calculate the distribution of observed energy loss per unit path length for an incident particle with fixed velocity. For argon and methane separately, the photoabsorption cross section $\sigma_\gamma(E)$ was expressed in terms of the oscillator strength $f(E)$ by

$$\sigma_\gamma(E) = \frac{2\pi^2 e^2}{mc}f(E),$$

and the oscillator strength was approximated by a sum over atomic levels

$$f(E) = \sum_i w_i f_i(E)$$

where w_i is the probability that an electron is found in atomic level i. The form of $f_i(E)$ was taken to be

$$f_i(E) = \begin{cases} \frac{s_i-1}{E_i}(\frac{E}{E_i})^{-s_i}, & \text{for } E > E_i \\ 0, & \text{otherwise,} \end{cases}$$

where s_i and E_i are constants for level i. The atomic levels and values of s_i and E_i used in the Monte Carlo are given in Table 2. Using this expression for $f(E)$, dN_i/dx was approximated for each atomic level and a value of $d\mathcal{N}_i/dx$ was chosen

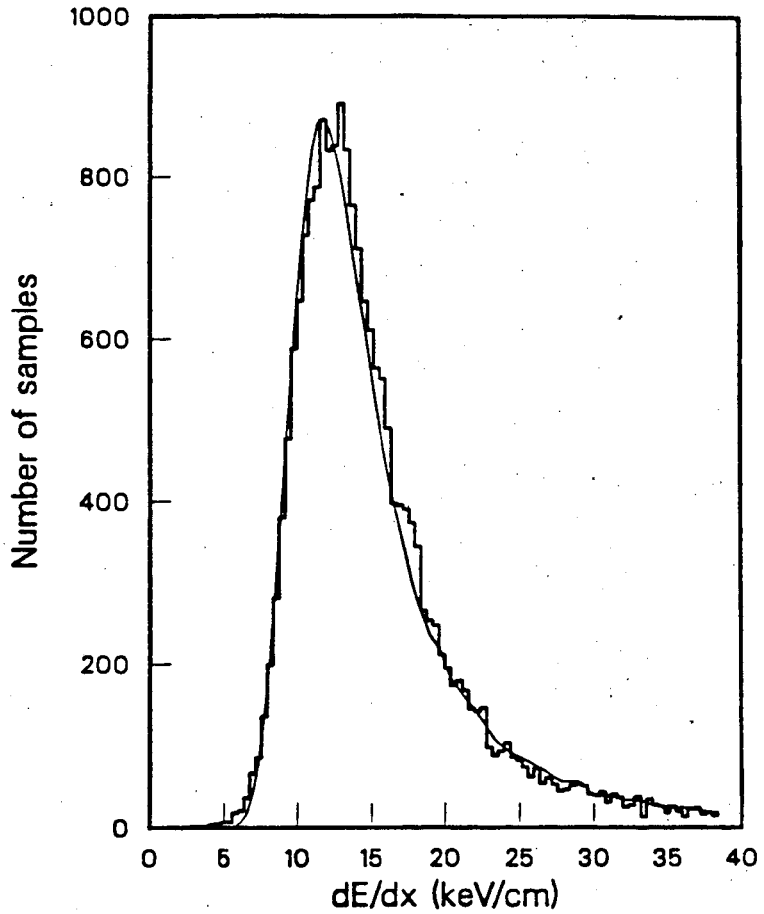

Figure 14: Distribution of energy losses in 4 mm of the 8.5 atm. argon-methane (80% – 20%) TPC gas.

according to a Poisson distribution. An average energy transfer per interaction was taken to be E^i_{eff} (Table 2) in the resonance region, and in the Rutherford region was chosen according to a $1/E^2$ distribution. The total energy deposited in dx was then calculated by summing the energy deposited in resonance and Rutherford collisions for each level i for the argon and the methane. The resulting distribution is shown in Fig. 14 along with the measured distribution. Its most striking features are its broad shape and long Landau tail [24]. Because the distribution is so wide, many measurements are needed to measure its shape or to form an estimator. Fig. 14 shows the intrinsic width (excluding the tail) of the energy loss distribution is $\sim 60\%$ of the most probable dE/dx value.

To associate the incident particle's velocity with the measured dE/dx distribution, it is desirable for practical reasons to have a single number, an estimator, reflect the distribution. Because of the Landau tail, the statistical uncertainty of the mean dE/dx is much greater than that of the most probable value, for a given

number of dE/dx samples. To estimate the most probable dE/dx, the mean of a fixed fraction r of the lowest measurements (the truncated mean) is used. The resolution of the truncated mean was found to be insensitive to values of r in the range $0.4 \leq r \leq 0.7$. We chose $r = 0.65$. The truncated mean will be referred to as the dE/dx value when talking about the estimator.

The measurement of dE/dx in the TPC proceeds along lines previously discussed. Ionization arriving at a wire undergoes proportional amplification. The wire signal is then amplified, shaped, and sampled 5 to 7 times by a CCD. Upon analysis, the three largest CCD samples are fit to a parabola to determine the pulse height, which is then corrected as previously discussed in section 2.2.2. Up to 183 wire signals can be obtained along a track. These individual measurements are then used to calculate a truncated mean.

In some cases the amplitude of the pad signals provides a more accurate dE/dx determination than the wire signals. In cases of track overlap, few wires are associated with a track. Since the pad signals integrate over several wires, the statistical significance of a pad signal is greater than for a wire signal. The pad signals are used to determine the dE/dx value if $N_{pads} \geq 0.4 N_{wires}$. This happens 13% of the time.

An assumption, which is widely used, is that the ionization I produced by a moving charged particle is proportional to its energy loss E, $I = E/W$, where the proportionality constant $1/W$ is independent of E [22]. We have assumed this, often speaking of energy loss and ionization equivalently.

The expected velocity dependence of the truncated mean was calculated using the formalism discussed above [15]. It was assumed the truncated mean dE/dx has the same velocity dependence as the most probable value, which is fairly easy to calculate.

The calculation proceeds along the same lines used to derive the dE/dx distribution, except a closed form expression is obtained. Again, the calculation is outlined for a monatomic gas for simplicity, but the extension to mixtures is straightforward. The most probable energy loss ΔE^{mp} in a thickness Δx of gas is approximated by the sum of a resonance and a hard scattering contribution,

$$\Delta E^{mp} = \Delta E^{mp}_{resonance} + \Delta E^{mp}_{Rutherford}.$$

$\Delta E^{mp}_{resonance}$ is given by the sum over energy levels of the most probable number of interactions from level i, times the average energy loss per interaction. The most probable number of interactions from level i is the mean ($\Delta x \; dN_i/dx$) minus 1/2, since the number of interactions follows a Poisson distribution. The values of the average energy loss E'_i for level i were obtained from the oscillator strength using the expression

$$\ln E'_i = \int_0^\infty \ln(\epsilon) f_i(\epsilon) d\epsilon.$$

The $f_i(E)$ used in the calculation are those given previously. Combining terms,

$$\Delta E^{mp}_{resonance} = \sum_i (\frac{dN_i}{dx}\Delta x - \frac{1}{2}) E'_i.$$

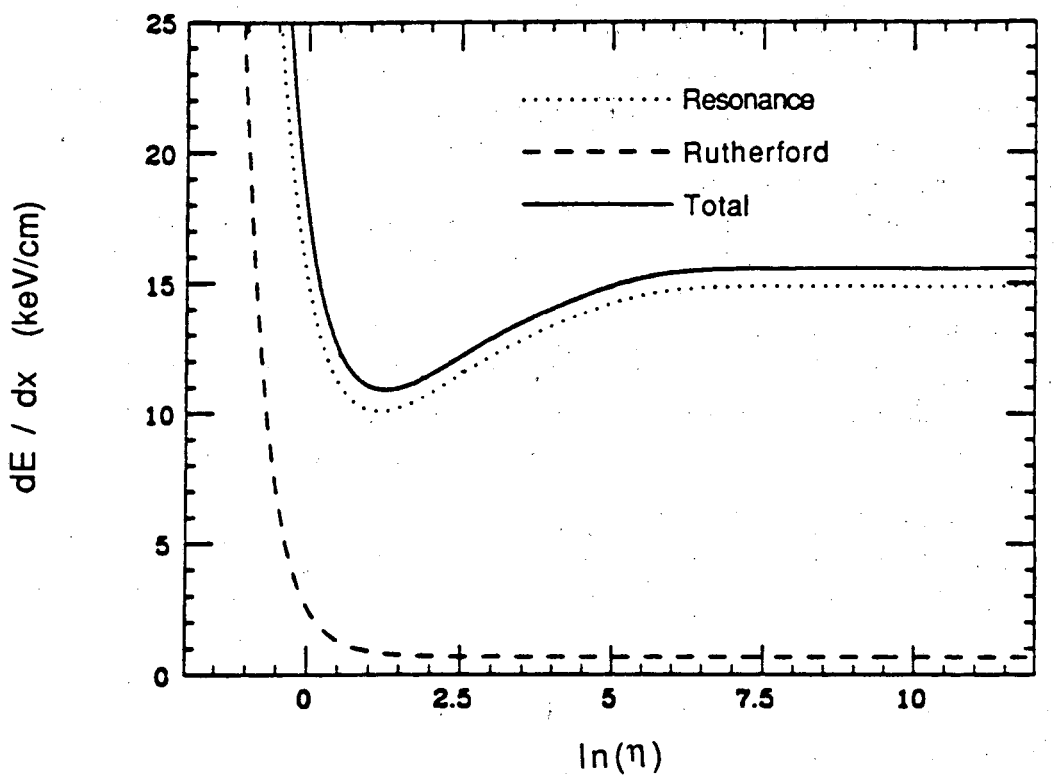

Figure 15: Calculated most probable energy loss per unit path length as a function of $\eta = \beta\gamma$.

The expression used for the most probable energy loss due to Rutherford scattering was that of Maccabee and Papworth [25], first derived by Landau [24].

$$\Delta E^{mp}_{Rutherford} = \sum_i \xi_i [\ln(\frac{\xi_i}{E'_i}) + 0.198]$$

where

$$\xi_i = \frac{2\pi e^4}{mc^2} n_i \Delta x \frac{1}{\beta^2}.$$

From these expressions, and taking into account the gas mixture of the TPC, the most probable energy loss as a function of $\beta\gamma = \beta/\sqrt{1-\beta^2}$ shown in Fig. 15 was obtained.

This calculated curve was then used as the basic functional form in a fit to experimental data. The average truncated mean dE/dx as a function of $\beta\gamma$ was measured for low energy protons and pions from multihadron events, cosmic ray muons, conversion electrons, and wide angle Bhabha electrons since all of these particles are easily identifiable. The $\beta\gamma$ value was extracted from the momentum. The fit was of the form

$$\ln(\beta\gamma)_{\text{model}} = A \ln(\beta\gamma)_{\text{measured}} + B$$

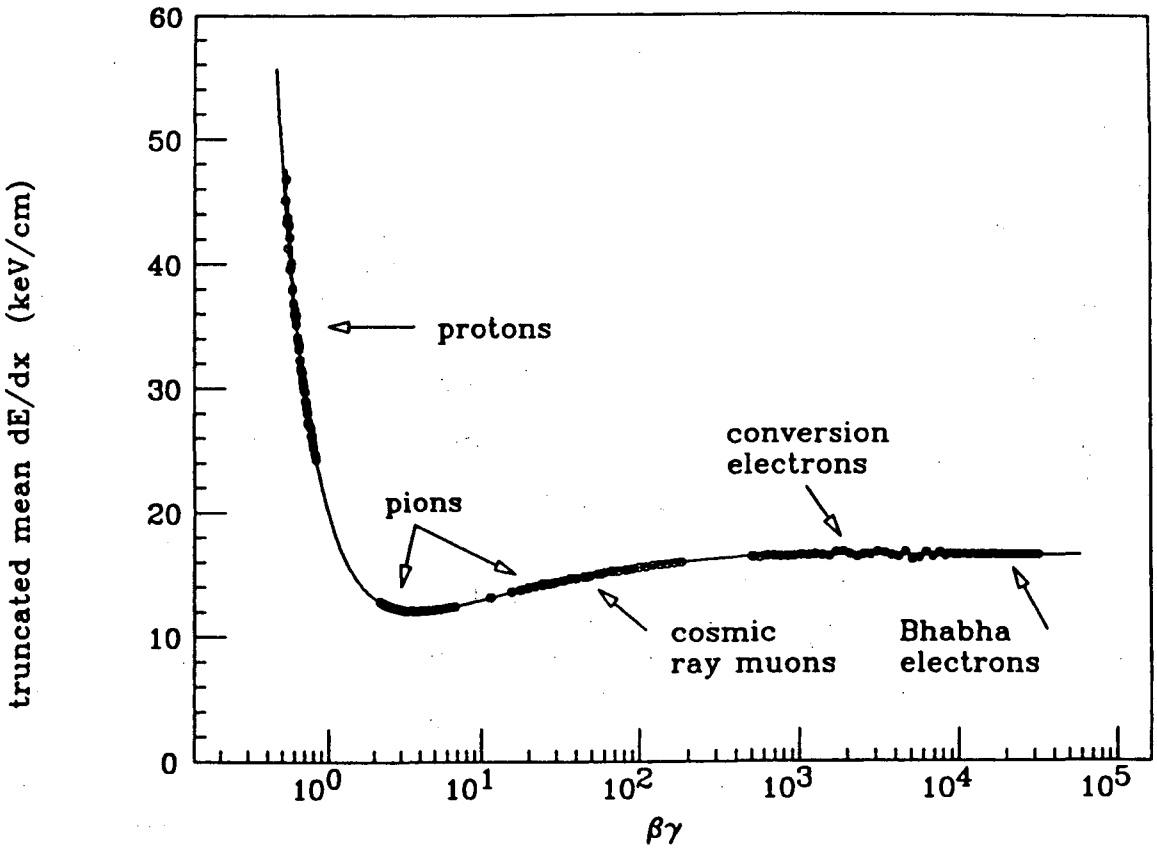

Figure 16: Fitted truncated mean dE/dx as a function of $\beta\gamma$ showing the various experimental measurements used in making the fit.

$$(dE/dx)_{\text{trunc. mean}} = C(dE/dx)_{\text{model}} + D$$

and is depicted in Fig. 16. The values of A, B, C, and D giving the minimum χ^2 were

$$A = 0.986$$

$$B = -0.055$$

$$C = 0.999$$

$$D = 1.53 \text{ keV/cm}.$$

The resulting χ^2 per degree of freedom was 1.50, indicating a very good parameterization of the truncated mean dE/dx as a function of $\beta\gamma$. A plot of the average R =(trunc. mean/prediction) as a function of $\beta\gamma$ for pions and cosmic ray muons in the relativistic rise region is shown in Fig. 17. It indicates the fitted dE/dx vs. $\beta\gamma$ curve is accurate to 0.2%.

The fitted dE/dx vs. $\beta\gamma$ curve can be easily converted to a dE/dx vs. momentum curve for a given particle type by scaling the abscissa with the particle mass. When

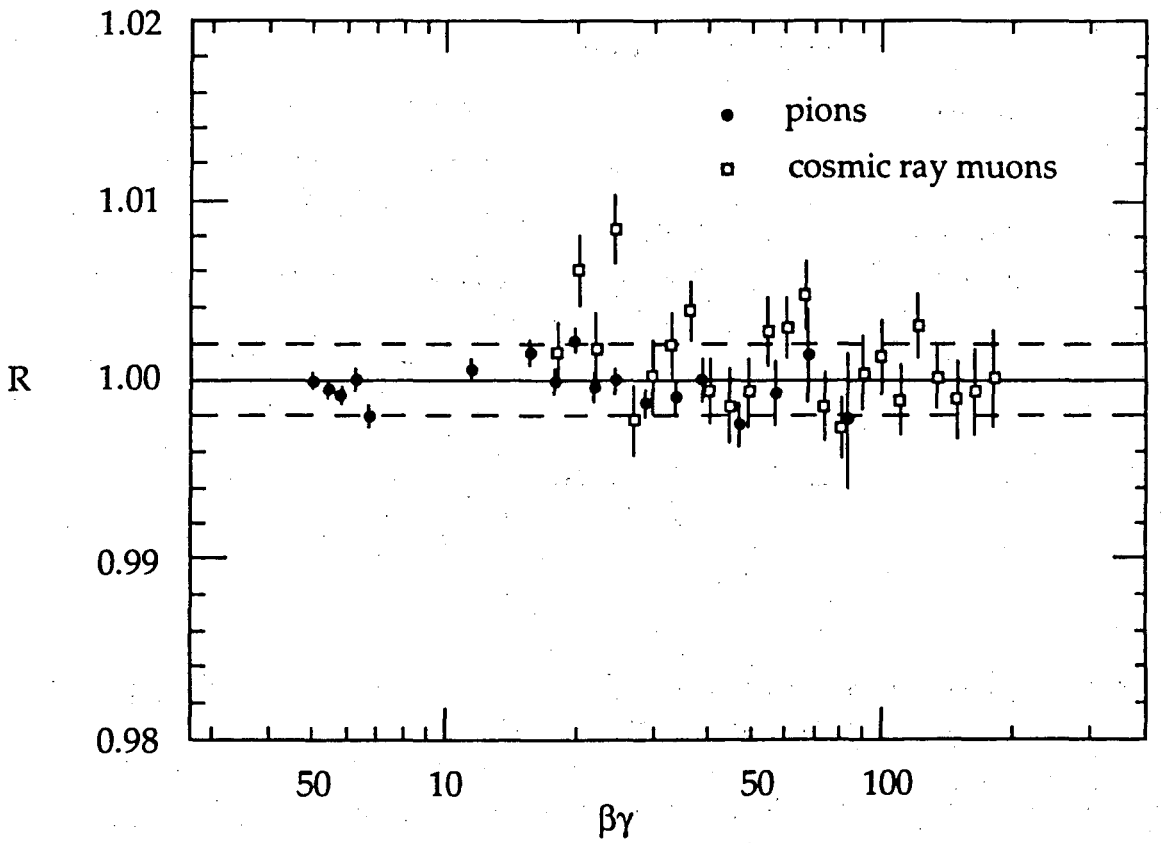

Figure 17: Plot of average R =(trunc. mean/prediction) as a function of $\beta\gamma$ for the relativistic rise region indicating the fitted dE/dx vs. $\beta\gamma$ curve is accurate to 0.2%.

this is done, the solid curves of Fig. 18 are generated. The figure also shows our measured dE/dx as a function of measured momentum for tracks with 80 or more wire hits (65% of the tracks) for the 1984-1986 data set. The bands of electrons, muons, pions, kaons, and protons are clearly visible. A deuteron band is also visible. (The deuterons are knocked out of the beam pipe.)

The distribution of dE/dx values in a momentum slice is approximately Gaussian with a relative width (dE/dx resolution) averaged over tracks of $3.6 \pm 0.2\%$ for minimum ionizing pions. Since an accurate knowledge of the dE/dx resolution is crucial for proper particle identification, the dE/dx resolution for minimum ionizing pions was measured as a function of the number of dE/dx samples and the track dip angle. The resolution as a function of the number of dE/dx measurements is shown in Fig. 19. The resolution is well described by

$$\frac{\sigma_{trmean}}{average\ trmean} = \sqrt{\frac{A}{\#wires} + B}\ (1 + C \cdot \#wires + D \cdot |\sin(dip)|).$$

A and B, giving the main contribution, were determined to be $A = 1.7 \times 10^{-1}$ and $B = 4.6 \times 10^{-4}$. $C = -5.5 \times 10^{-4}$ and $D = -2.6 \times 10^{-1}$ give a small fine tuning of the resolution. For particles in the relativistic rise region, cosmic ray studies indicated that the relative dE/dx resolution is approximately independent of momentum (i.e. mean dE/dx). Studies of protons in the $1/\beta^2$ (i.e. large dE/dx) region showed, however, that the relative dE/dx resolution of these tracks improves by a factor of approximately $((dE/dx)_{min\ ion}/(dE/dx))^{0.35}$.

For minimum ionizing pions, the distribution in

$$S = \frac{\text{trunc. mean} - \text{prediction}}{\text{predicted resolution}}$$

is shown in Fig. 20 for tracks with at least 80 wires. The distribution is consistent with Gaussian of width 1 out to approximately 3 S.D.

For tracks that use pads to determine the dE/dx, the resolution is considerably worse than for tracks that use wires. The resolution for tracks with at least 13 pads is 7.6%.

Overall, the average dE/dx resolution improved in 1984 because of better corrections. For Bhabhas it improved from 3.1% to 2.9%, and for tracks with 120 or more wire hits in jet events the dE/dx resolution improved from 3.6% to 3.4%.

Except in regions where the dE/dx curves cross, the energy loss measurement provides a separation between species of many S.D. at low momentum, and of 1-2 S.D. k/p and 2-4 S.D. π/k at high momentum. A plot of relative dE/dx separation vs. momentum is shown in Fig. 21 (assuming a nominal resolution of 3.6%), from which the regions of good particle identification are evident.

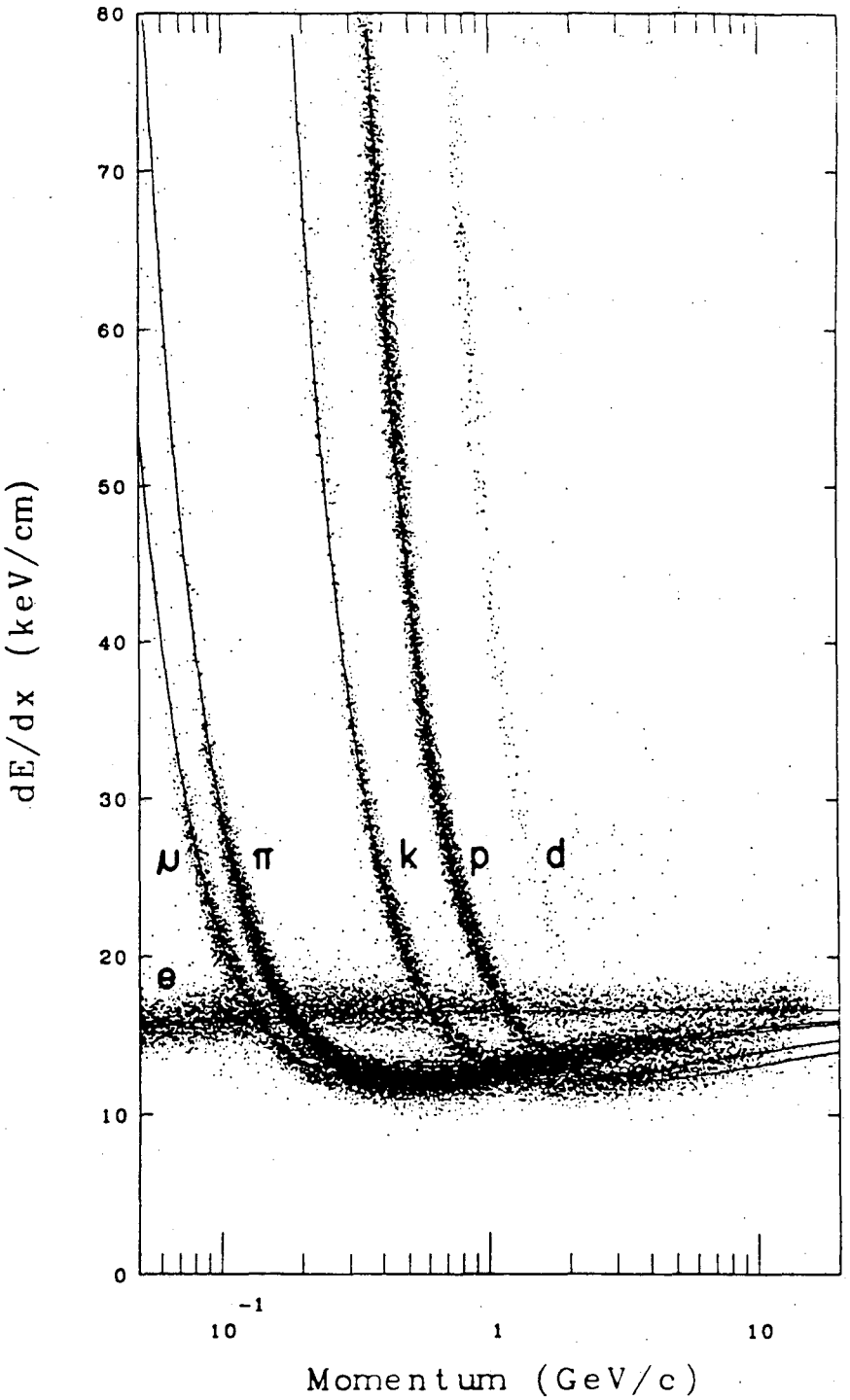

Figure 18: Measured dE/dx as a function of momentum. The bands of electrons, muons, pions, kaons, and protons are clearly visible. The appropriate curves from the fitted truncated mean dE/dx vs. $\beta\gamma$ plot (obtained by scaling the abscissa by the particle mass) are also shown.

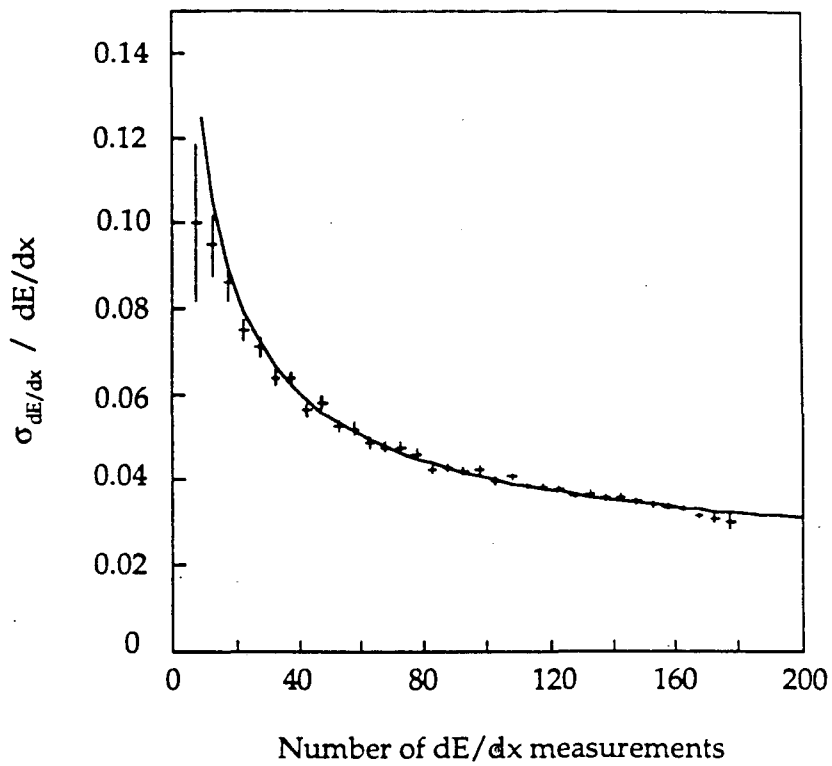

Figure 19: Plot showing the dependence of the dE/dx resolution on the number of wires.

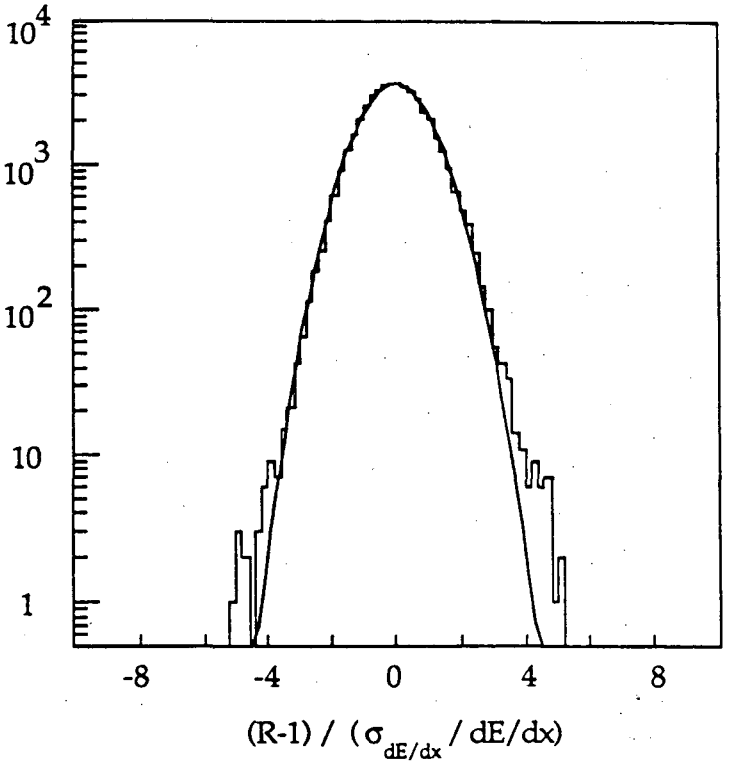

Figure 20: Plot showing the distribution in S (as defined in the text) for minimum ionizing pions. The distribution is consistent with Gaussian of width 1 out to approximately 3 S.D.

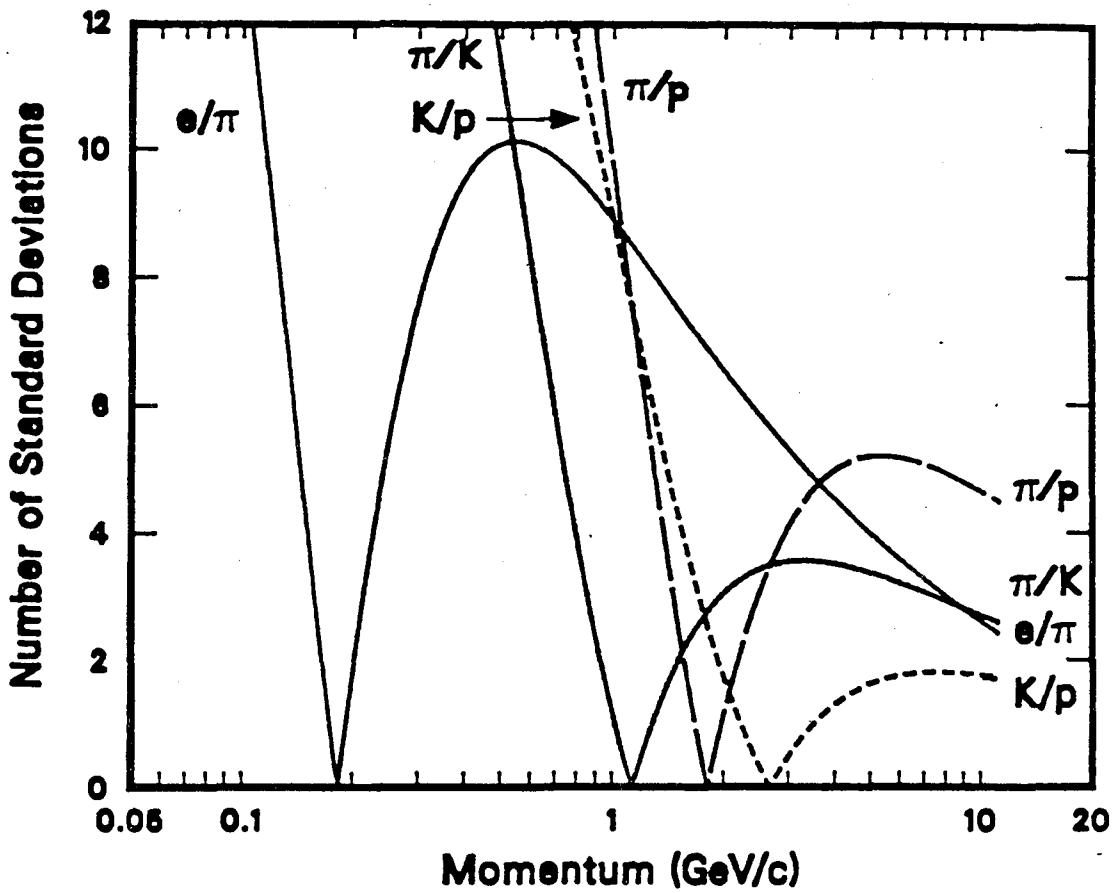

Figure 21: Plot showing the dE/dx separation in terms of the resolution as a function of momentum.

4.2 Particle identification algorithms

In the $1/\beta^2$ region of the dE/dx vs. momentum plot, particle identification is easy since the dE/dx bands are widely separated (see Fig. 18). The measured momentum and dE/dx value uniquely determine the particle type. Cross sections and particle fractions as a function of momentum are easily found in this region by counting particles.

One dimensional fits to the dE/dx spectrum for a small momentum slice determine the number of particles of each species as a function of momentum. The dE/dx spectrum is expressed as a sum of Gaussians, one for each particle species. The area under each Gaussian gives the number of particles, from which cross sections and particle fractions are easily determined. This is illustrated in Fig. 22 for particles with momenta between 4.4 and 5.1 GeV/c. Such fits use the maximum amount of the information available, but the method is straightforward only for momentum distributions; it fails if particles are selected according to some other criteria such as rapidity or transverse momentum since the dE/dx spectrum in a rapidity or p_t interval is no longer a sum of Gaussians.

When cross sections in rapidity or momentum transverse to an event axis are desired, an unfolding technique provides an attractive alternative to one dimensional fits. Basically, some algorithm is used to identify particles; the raw rates are then corrected for misidentification using a "confusion matrix" derived from a Monte Carlo simulation.

Both the dE/dx fitting technique and the unfolding technique of data analysis were used for this paper. Both methods are described in detail in the following section. The dE/dx fitting technique was used to find the cross sections and particle fractions as a function of scaled momentum $z = 2p/\sqrt{s}$ and as a function of scaled energy $x = 2E/\sqrt{s}$ for $x > 0.5$. All other distributions were found using the unfolding technique.

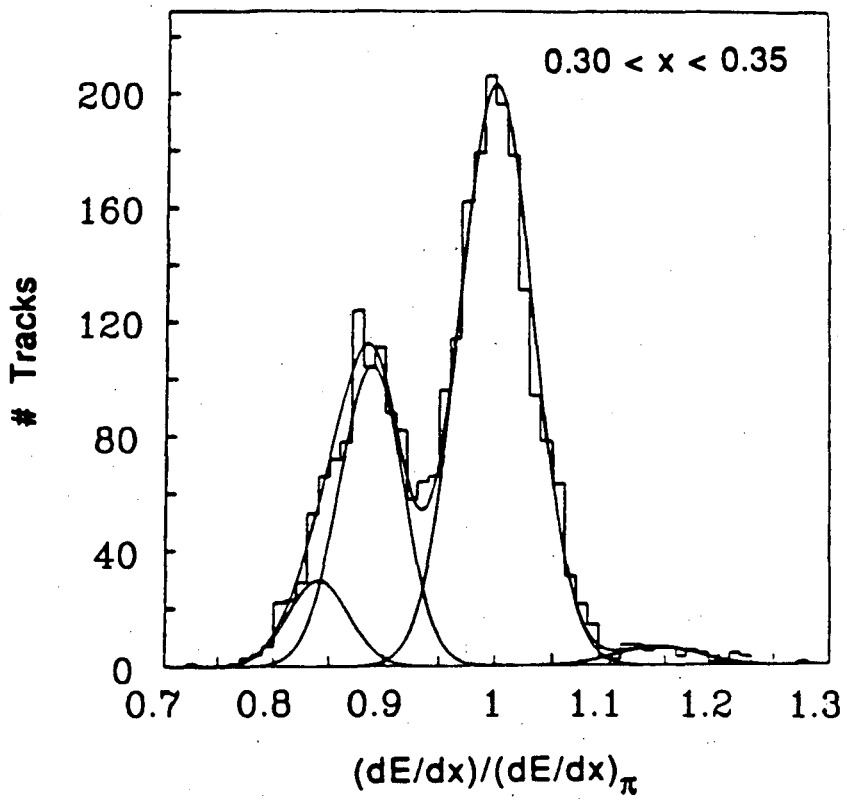

Figure 22: At high momentum a sum of Gaussians can be fit to the dE/dx spectrum to determine the number of particles of each species present.

5 MEASUREMENT OF INCLUSIVE CROSS SECTIONS

5.1 Definition of variables and choice of event axis

The cross sections presented in this paper are

1. $\frac{1}{\beta\sigma}\frac{d\sigma}{dx}$ $\quad (x = 2E/\sqrt{s})$
2. $\frac{z}{\sigma}\frac{d\sigma}{dz}$ $\quad (z = 2p/\sqrt{s})$
3. $\frac{1}{\sigma}\frac{d\sigma}{d|y|}$ $\quad (y = \frac{1}{2}\ln(\frac{E+p_\parallel}{E-p_\parallel}))$
4. $\frac{1}{\sigma}\frac{d\sigma}{dp_t^2}$
5. $\frac{1}{\sigma}\frac{d\sigma}{d|y|dp_t^2}$

for pions, kaons, and protons (both + and − charges are combined). For each cross section the associated particle fractions are also given. E is the particle energy, p is its momentum, $p_\parallel$ and p_t are the components of momentum along and transverse to the event axis, respectively, and $\sqrt{s} = 29$ GeV at the PEP ring.

The distributions involving rapidity (y) and transverse momentum (p_t) require the definition of an event axis. The two most common choices are the sphericity axis and the thrust axis, and we present distributions for both. The sphericity axis is determined by finding the direction of the unit vector $\vec{n}$ that minimizes

$$S(\vec{n}) = \frac{3}{2}\frac{\sum p_i^2 \sin^2\theta_i}{\sum p_i^2},$$

where the sums run over all charged particles. p_i is the magnitude of the momentum of particle i, and θ_i is the angle between the direction of particle i and the vector $\vec{n}$ that is being varied. The thrust axis is determined by finding the direction that maximizes

$$T(\vec{n}) = \frac{\sum |p_i \cos\theta_i|}{\sum |p_i|}.$$

This expression is linear in the particle momenta, and therefore is more stable under fluctuations in fragmentation than sphericity.

As pointed out in [26], rapidity and p_t distributions measured with respect to an event axis determined from the tracks themselves is, strictly speaking, not a truly inclusive measurement. Almost by definition, the choice of a jet axis will introduce some bias. Sphericity and thrust behave rather complementary in this regard, and their effect on inclusive distributions can be understood qualitatively as follows [27]. Consider the hypothetical case in which all tracks in an event lie in a plane. Suppose the direction of $\vec{n}$ is close to extremizing $S(\vec{n})$ or $T(\vec{n})$, and consider the sensitivity of $S(\vec{n})$ and $T(\vec{n})$ to changes $d\theta$ in the direction of $\vec{n}$:

$$dS \sim \sum_i 2p_i^2 \sin\theta_i \cos\theta_i d\theta$$

and

$$dT \sim \sum_i (\pm) p_i \sin\theta_i d\theta,$$

where $(\pm)$ in dT accounts for the effect of the absolute value in T. From these relations several facts emerge regarding the final extrema of S and T:

1. Because of p_i^2, the sphericity axis tends to align along fast tracks.
2. Sphericity tolerates low momentum tracks perpendicular to the axis.
3. Thrust avoids having particles perpendicular to the jet axis, even at the expense of a minor misalignment of fast particles.

The influence of detector acceptance and momentum measurement errors on the direction of the sphericity and thrust axes was studied using a Monte Carlo [27]. The reconstructed axis using charged particles was compared to the "true" sphericity or thrust axis derived using all generated (charged + neutral) particles, the angle between them being ϕ (always positive). It was found that the accuracies of the sphericity and thrust axes were identical and gave $\langle\phi\rangle \simeq 9°$. However, if very poorly measured tracks were included, thrust was more reliable than sphericity as might be expected since it depends only linearly on the momentum. But for tracks measured with the typical TPC resolution, those used for this analysis, both methods were well within their range of stable operation.

Our Monte Carlo studies determined that the errors on the measured values of y and p_t were due largely to errors in the determination of the jet axis. For the older data set, the resolution for measuring rapidity was $\sigma_y \simeq 0.3$ for y near zero and $\sigma_y \simeq 0.5$ for large y. Of this, the contribution from momentum measurement error was $\sigma_y \simeq 0.1$ for y near zero and $\sigma_y \simeq 0.2$ at large y. Both sphericity and thrust gave similar results.

It was also determined in our Monte Carlo studies that the dip in $d\sigma/dy$ at $y = 0$ is more pronounced using the thrust axis than the sphericity axis. This is borne out by the data presented here. The dip is easily understood from the previous discussion since thrust tends to remove particles perpendicular to the event axis $(y = 0)$.

5.2 Unfolding technique to measure cross sections

The cross sections and particle fractions were determined in two steps. An algorithm was used to identify tracks in the TPC as electrons, pions, kaons, or protons. Then corrections derived from our fast detector simulation Monte Carlo were applied accounting for particle misidentification and detector acceptance. The process is described in detail below.

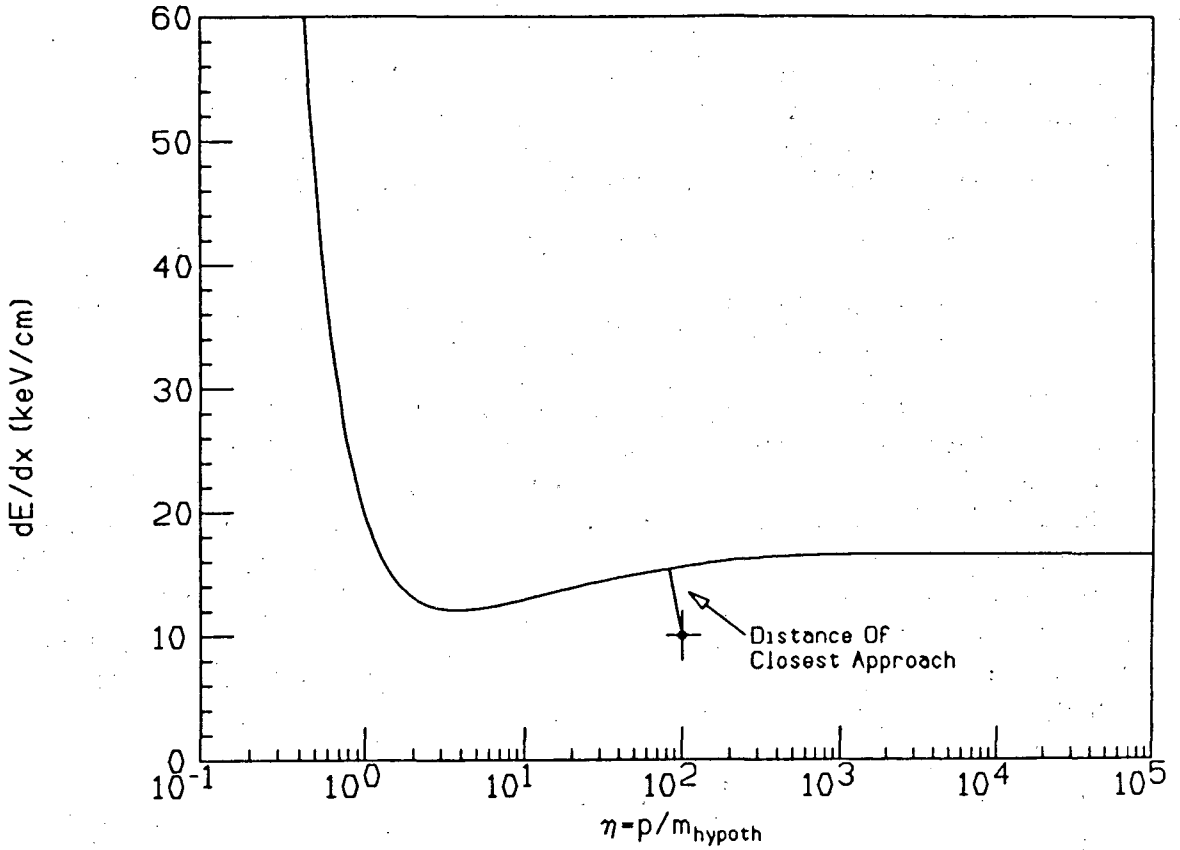

Figure 23: The χ^2 assigned to an identity hypothesis is the "distance" in terms of the resolutions from the point $(\eta,(dE/dx)_{meas})$, $\eta = p_{meas}/m_{hypoth}$, to the dE/dx vs. η curve.

5.2.1 Particle identification

To identify particles, having measured the momentum and dE/dx in the TPC, different particle hypotheses (e,π,k,p) are tried and a χ^2 is determined for each hypothesis. The method for determining the χ^2 is illustrated in Fig. 23. The measured momentum divided by the hypothesized mass determines the abscissa and the measured dE/dx determines the ordinate of a point in the plot. The χ^2 for the mass hypothesis is given by the distance of the point from the fitted dE/dx vs. $\beta\gamma$ curve in terms of the dE/dx and momentum resolutions. The χ_i^2 $(i = \mathrm{e},\pi,\mathrm{k},\mathrm{p})$ are converted to probabilities P_i by incorporating guesses for particle fractions $f_i(p)$ based on previous measurements. Our final results are very insensitive to the values of $f_i(p)$ used, since their effect on particle misidentification is corrected for, as discussed later. P_i is defined as

$$P_i = N f_i(p) \mathrm{e}^{-\frac{1}{2}\chi_i^2},$$

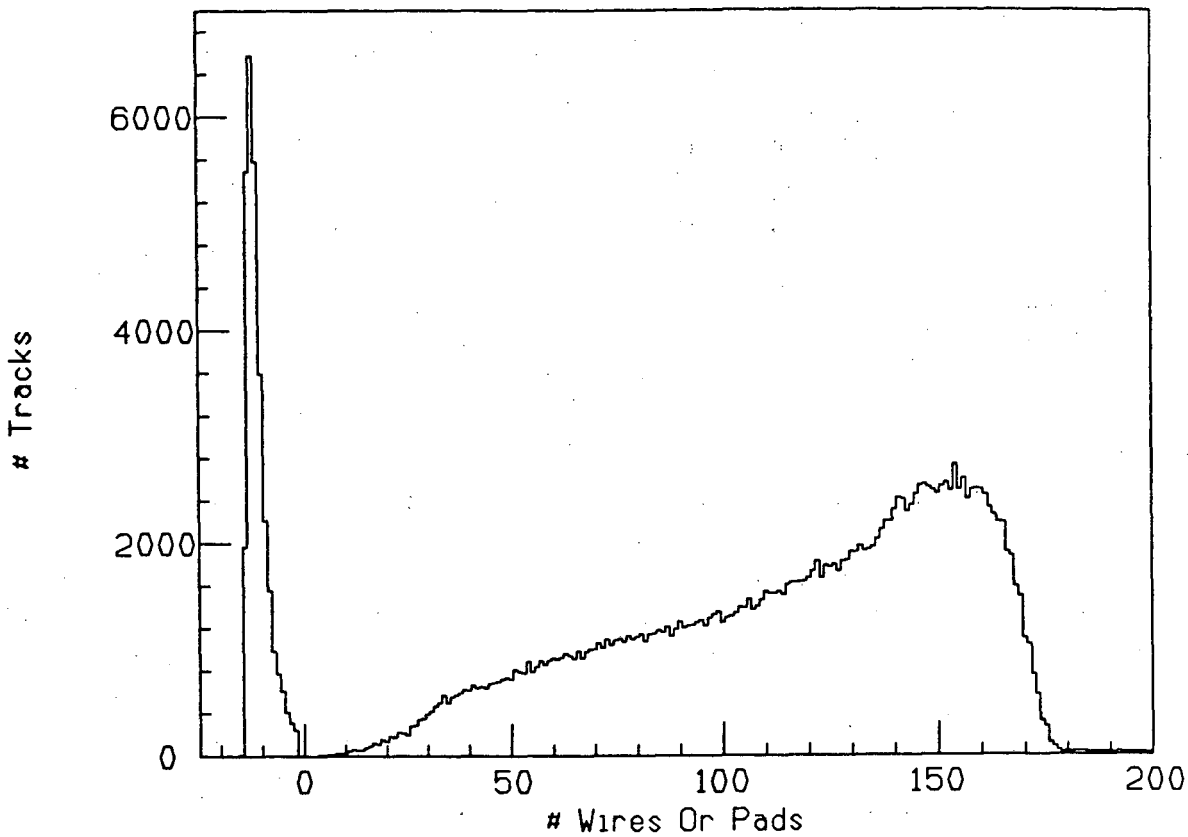

Figure 24: Distribution of the number of wires per track for tracks used in this analysis. A negative number of wires indicates pads were used for dE/dx.

where N normalizes the sum of the P_i. A particle is "identifiable" and considered of type j if the following criteria are met:

1. The number of dE/dx samples has to be larger than or equal to 40, and the dE/dx must not have been determined from the pad signals.
2. The ionization measured must not have saturated the electronics.
3. The χ^2 for hypothesis j has to be less than or equal to 10.
4. The probability of hypothesis j, P_j, must be larger than or equal to 0.7.

Fig. 24 shows the distribution of the number of wires per track for tracks used in this analysis. 12.9% of the tracks use pads for dE/dx and 3.8% of the tracks that use wires have fewer than 40 wires, so 16.7% of the tracks are excluded by cut 1. This cut and cut 2 are needed to get an accurate dE/dx measurement. Cut 4 selects for the analysis only tracks with a high probability of being from a certain particle

type. In the Monte Carlo, pions are identified correctly more than 95% of the time over the momentum range, while outside of crossover regions, kaons and protons are identified correctly more than 85% and 60% of the time, respectively.

No attempt has been made to separate muons from pions. Since most muons come from pion decay, such a separation would rely heavily on the event generator Monte Carlo. Thus, our "pion" cross sections are actually pion+muon cross sections, including pions and a small number of muons from sources other than pion decay.

5.2.2 Unfolding

The particles identified via the method just described are counted for each bin of the independent variable. This gives experimentally determined average numbers per event of electrons, pions, kaons, and protons M_i ($i = \mathrm{e}, \pi, \mathrm{k}, \mathrm{p}$) for each bin. The M_i are corrected for particle misidentification, detector acceptance, and initial state radiation by the matrix inversion technique we now describe.

There is some ambiguity regarding particle decays in defining the corrections. We correct to a "vertex" where particles with lifetimes shorter than 10^{-9} sec have decayed, leaving only the long lived particles γ, ν, $\mathrm{e}^{\pm}$, $\mu^{\pm}$, $\pi^{\pm}$, $\mathrm{k}^{\pm}$, k_L, p, $\bar{\mathrm{p}}$, n, and $\bar{\mathrm{n}}$.

Let V_i ($i = \mathrm{e}, \pi, \mathrm{k}, \mathrm{p}$) be the actual average number of particles per event of type i produced at the $\mathrm{e}^+\mathrm{e}^-$ interaction "vertex" with no initial state radiation and after short lived particles have decayed. Particles and antiparticles have been lumped together, and π stands for pions+muons as discussed earlier. The V_i are the desired quantities.

We define I_i ($i = \mathrm{e}, \pi, \mathrm{k}, \mathrm{p}$) as the average number per event of particles of type i in the TPC which are "identifiable", meaning the cuts of the previous subsection were passed. The I_i and the V_j are related by an expression $I_i = D_{ij}V_j$, or in matrix form

$$I = DV.$$

D_{ij} is the probability that a particle of type j at the vertex produces an identifiable particle of type i in the TPC. Note that D is diagonal to a good approximation, and that D_{ii} is essentially the probability that a particle of type i at the vertex makes it into the TPC and passes the cuts to be identified as something.

Since the particle identification is imperfect, a particle of type j is labeled as type i with probability C_{ij}. The average measured number per event M_i of particles called i is $M_i = C_{ij}I_j$, or in matrix form,

$$M = CI.$$

Note that the columns of C sum to 1. Combining equations gives

$$M = CDV,$$

and multiplying by the inverses of the matrices gives the desired result

$$V = D^{-1}C^{-1}M.$$

The C matrix describing particle misidentification depends on well-measured detector properties such as the separation in dE/dx between species and the dE/dx and momentum resolutions, and on the algorithm used for identification. Any dependence on the physics generator is very indirect (the angular width of jets, etc. influences track overlap in the TPC, and hence the average number of wire samples and the dE/dx resolution); in particular, the C matrix is independent of the particle composition created by the event generator. Changing the fractions $f_i(p)$ changes the M_i's, and the C_{ij}'s and D_{ij}'s, but not the resulting V_i's. This was in fact tested by using several sets of $f_i(p)$, among those a set of constant fractions $f_e = 0.05$, $f_\pi = 0.75$, $f_k = 0.15$, and $f_p = 0.05$ for all momenta. The resulting z distributions were computed and agreed with the distributions presented here within errors.

The D matrix is diagonal to a good approximation. Small nondiagonal elements are due e.g. to nuclear interactions in the beam pipe with a secondary in the TPC. Also, such effects as momentum smearing and initial state radiation move tracks into different kinematical bins. Since all these corrections are small, instead of unfolding the data, we define an effective diagonal D matrix for a given bin as follows:

$$D_{ii} = \frac{\begin{array}{c}\#\text{ of particles of type } i \\ \text{identified as something in the TPC} \\ \text{per generated event including initial state radiation}\end{array}}{\begin{array}{c}\#\text{ of generated particles of type } i \text{ after decays} \\ \text{per event with no initial state radiation}\end{array}};$$

$$D_{ij} = 0 \text{ for } i \neq j.$$

D_{ii} is the average number of particles of type i in the TPC in the given bin identified as something, divided by the average number of particles of type i in the given bin at a generator vertex with no initial state radiation. Thus the D matrix does the acceptance correction, the initial state radiation correction, and corrects for mismeasurement of the independent variable. A reliance on the physics generator is introduced since the particle fractions must be right to account for non-diagonal effects such as kaon decay before the TPC, although such effects are small. (If pions were separated from muons, the corresponding off diagonal term would be required since it would be large.) One possible large non-diagonal effect is pions, for instance, knocking protons from the beam pipe into the TPC. Only negative particles from the TPC were used in the analysis to avoid this problem, since the cross sections for such processes are not perfectly simulated.

When the generator is run without initial state radiation for determining D_{ii}, the rapidity and p_t bins a particle goes in are determined from the event axis calculated using only charged stable particles. So no correction is made to find the distributions using all particles (or some other scheme) to determine the event axis.

Figure 25 shows plots of the C and D matrix elements as a function of $z = 2p/\sqrt{s}$. The dE/dx crossover regions are clearly visible in the plots of C_{ij} as dips in C_{ii} and peaks in C_{ij}, $i \neq j$. The close p-π and p-k crossover regions leave nothing called a proton from $z \simeq 0.12$ to $z \simeq 0.22$ making the C matrix singular in this

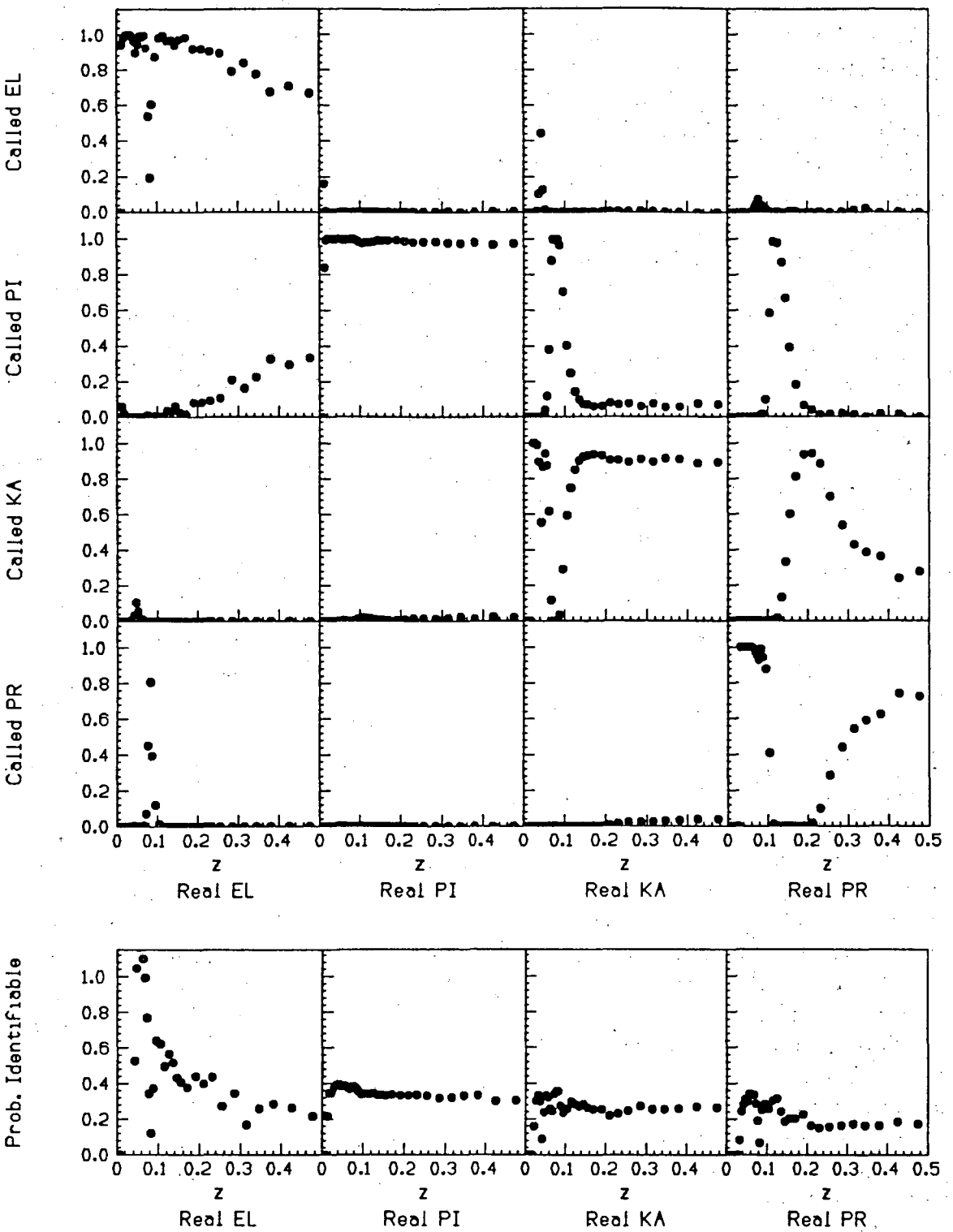

Figure 25: Plots of C_{ij} and D_{ii} as a function of scaled momentum. The effect of the dE/dx crossover regions is apparent.

region. Otherwise, the particle identification is very good. Since only negative particles from the TPC are used in the analysis, the maximum value of D_{ii} in principle is 0.5. The electrons knocked out of the material in front of the TPC, however, make $D_{el,el} > 0.5$ at low z. The effects of the crossover regions are visible in D_{ii} since it includes a correction for the requirement that the particle be identified as something.

A very important problem in the unfolding process is that the bin a particle goes in must not depend on the identity assigned to that particle, otherwise misidentification could move particles between bins. The bin a particle goes in should only depend on its measured momentum, even for variables like x which depend on mass. To see how this was done, consider the variable $x = 2E/\sqrt{s}$ which depends on the particle's identification through the mass in the energy. First, the π, k, and p cross sections were determined for bins in x_π ($x_\pi \equiv 2\sqrt{p^2 + m_\pi^2}/\sqrt{s}$). The full analysis was then repeated for x_k and x_p. Only the pion cross sections were used from the x_π binning, only the kaon cross sections were used from the x_k binning, etc. The x_i values used in each case were the correct x values for the particles kept. Thus the bins did not depend on the identity we assigned to the particle.

In areas where one particle species is absent, such as for $x_p < 2m_p/\sqrt{s}$, the dimensions of the C and D matrices are reduced correspondingly.

A place where the unfolding method fails is in the dE/dx crossover regions. For instance, all the kaons might be called pions in the π-k crossover leaving no particles called kaons. In this case a row of the C matrix has all zeros and it can not be inverted. A partial fix to this problem is to combine the species whose dE/dx bands are crossing, allowing the cross section for the remaining species to be found. Thus, the proton cross section was found in the π-k crossover region, etc.

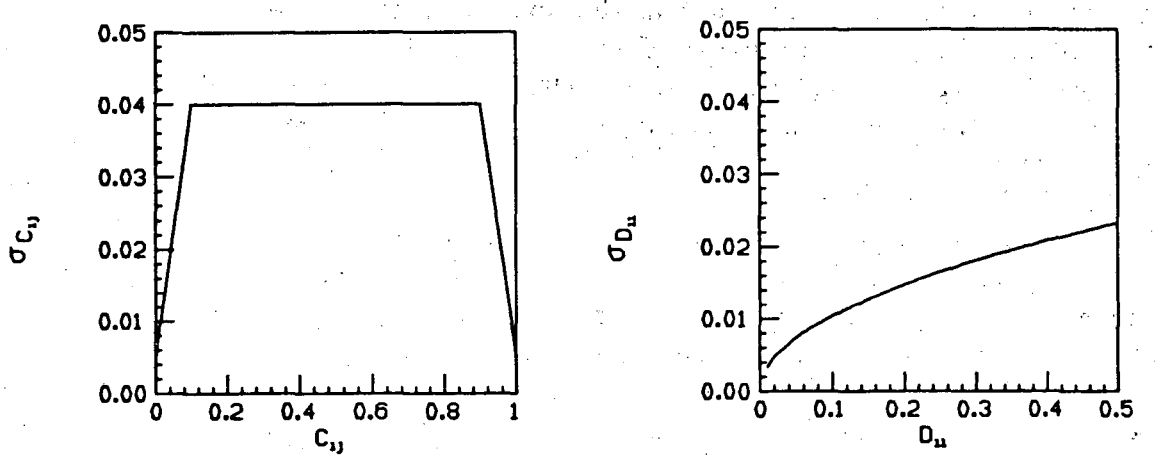

Figure 26: Systematic error $\sigma_{C_{ij}}$ as a function of C_{ij}, and systematic error $\sigma_{D_{ii}}$ as a function of D_{ii}.

5.2.3 Error analysis

The error analysis becomes fairly laborious when using the matrix inversion technique. Each term in both the C and D matrices has an error associated with it, and these errors have to be propagated through the matrix inversion. This was done using standard techniques for small errors. Statistical errors enter in the measured number of particles and in the C and D matrix elements since they were computed with large, but limited statistics. Systematic errors enter in both the C and D matrix elements and these will be discussed further below. All errors were assumed to be uncorrelated except for the C matrix elements since the columns sum to 1. The resulting correlations were taken into account.

The systematic error on the C matrix elements is controlled by how well the detector simulator Monte Carlo mimics the experimental data in assigning dE/dx and momentum values to tracks so the misidentification probabilities are correct. The shape of the average truncated mean vs. $\beta\gamma$ curve used in the Monte Carlo has the largest effect. To estimate the systematic error on the C matrix elements, the shape of this curve was varied within an uncertainty of 0.3% and the changes in the C_{ij} were noted. For both $C_{ij} \simeq 0$ and $C_{ij} \simeq 1$ there was very little change (≤ 0.005), and for intermediate C_{ij} the largest change was ~ 0.04. The systematic error as a function of the value of C_{ij} shown in Fig. 26 was used. In general, the final errors were found to be insensitive to the error on the intermediate C_{ij} values because the errors on the D_{ii} dominated.

There are three major contributions to the error on a D matrix element. D_{ii} is the probability that a particle of type i goes through the beam pipe and is identified (correctly or incorrectly). The probability to go through the beam pipe depends on nuclear cross sections which are accurate in the detector simulator to 10%. This puts

approximately 1.6% error on the probability of a particle to interact in the beam pipe in the Monte Carlo. Once a particle is in the TPC it has to be found by pattern recognition programs. The track finding efficiency is $\sim (97 \pm 2)\%$, determined by scanning events. Once the track is found it has to be identifiable, meaning that it has to pass cuts on the number of wires, can not be a conversion electron (determined by track reconstruction), and has to have a probability larger than 0.7 of being a particular particle type. In comparisons of the Monte Carlo to the data, the Monte Carlo reproduced the probability to pass these cuts to 2.1%. Adding these errors in quadrature gives a systematic error to the D_{ii} of $(\sigma_{D_{ii}}/D_{ii}) = 3.3\%$. Small values of D_{ii} indicate larger losses and are generally accompanied by increased uncertainties. The resulting systematic error can be represented as $\sigma_{D_{ii}} = 0.033\sqrt{D_{ii}}$. Note that typically $0 \leq D_{ii} \leq 0.5$ since only negative particles are included in the analysis.

5.3 Fitting technique to measure momentum distributions

A fitting technique [28] was used to determine the cross sections and particle fractions as a function of scaled momentum $z = 2p/\sqrt{s}$ and as a function of scaled energy $x = 2E/\sqrt{s}$ for $x > 0.5$. For the momentum distribution, the fitting technique provided smaller errors as noted in section 4.2. For the energy distribution in the high x region, the unfolding technique works in principle, but few particles satisfy the criteria to be identified so the statistics are poor. Also, as the dE/dx bands converge, the reliance on the dE/dx being correct in the Monte Carlo increases. For these reasons, fits to the dE/dx spectrum were used to find the cross sections and particle fractions for $x > 0.5$.

For the determination of the cross sections and hadron fractions using the dE/dx fit, the tracks are divided into momentum intervals as shown in Fig. 27. The number of particles of each type: e, π, k, p, are determined by an extended maximum likelihood fit [29]. The likelihood function is given by

$$L = \exp(-\sum_i \phi_i) \prod_j (\sum_i \frac{\phi_i}{\sqrt{2\pi}\sigma_{ij}} \exp(\frac{-(R_j - \mu_i(p_j))^2}{2\sigma_{ij}^2}))$$

where the index j runs over all tracks in the momentum interval, and i runs from 1 to 4 corresponding to the four particle species: e, π, k, and p. R_j is the measured dE/dx for track j divided by the predicted value for a pion at the measured momentum of the track; σ_{ij} is the R resolution for track j, particle hypothesis i, which is estimated from the number of dE/dx measurements, the dip angle, and the curvature error of the track; $\mu_i(p_j)$ is the expected R value for a track of momentum p_j, particle species i. There are four adjustable parameters ϕ_i, $i = 1, 4$, corresponding to the abundances of the four particle types. The fit does not require binning in the variable R (i.e. dE/dx) and makes maximal use of the information available for each track. We do not attempt to separate pions from muons, but instead subtract the muon rate obtained in an independent measurement [30].

The number of hadrons in each momentum interval is then corrected for effects of geometrical acceptance, nuclear interactions in the material between the interaction

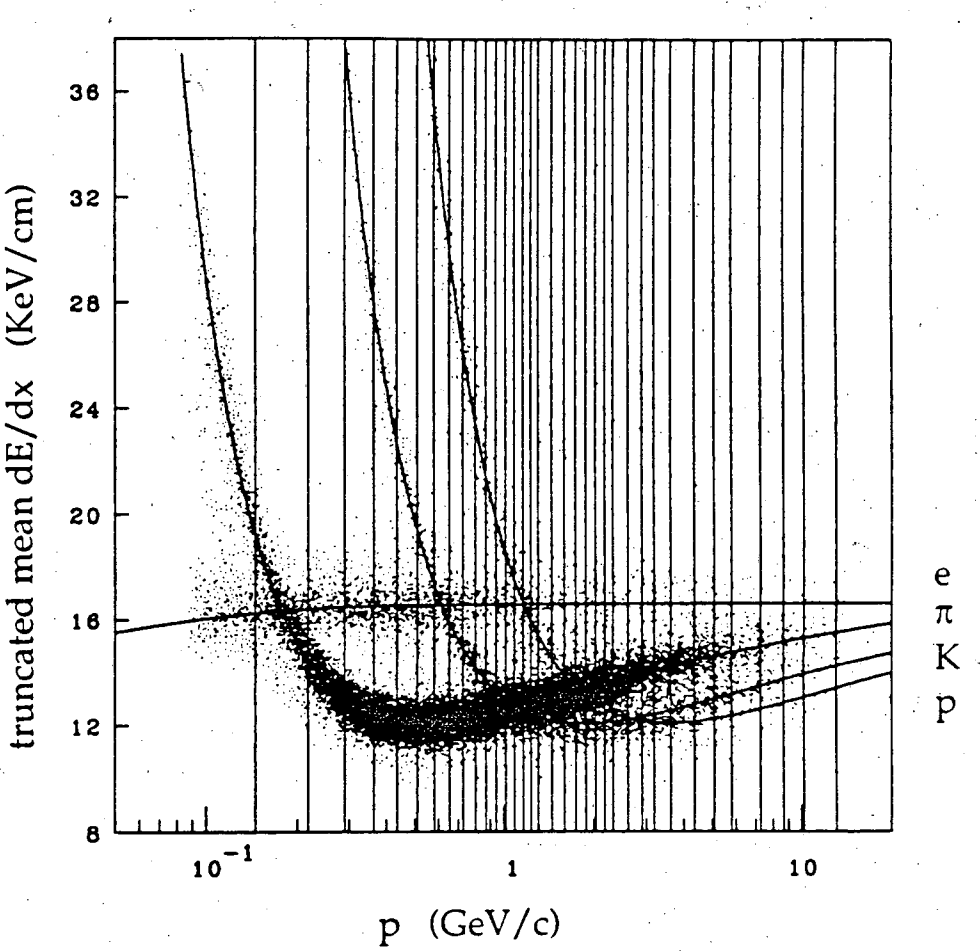

Figure 27: Momentum intervals used in the dE/dx fits.

point and the detector, event and track selection cuts, muon contamination of the pion sample, momentum smearing and initial state radiation. Protons are defined to include decay products of weakly decaying baryons; pions include decay products of k_s^0 but not k_l^0. Typical efficiencies are 70% for pions and kaons and 60% for protons. The proton efficiency is lower due to differences in the nuclear interaction cross sections and inability to detect protons coming from decays of high momentum lambdas. (Approximately 80% of the decays $\Lambda \rightarrow \pi p$ above 10 GeV occur outside the active volume of the TPC or result in proton and pion tracks not sufficiently well separated to allow the required number of dE/dx measurements.)

Errors are assigned on a momentum dependent basis and correspond to the quadratic sum of statistical and systematic uncertainties. For the cross sections, statistical errors dominate above $x \simeq 0.5$. The systematic errors for the proton and kaon cross sections are dominated by an 0.2% uncertainty in the dE/dx vs. velocity curve and an 8% uncertainty in the dE/dx resolution. The pion cross section is dominated by a 2% uncertainty in the pattern recognition efficiency. A number of the systematic errors (eg. those related to acceptance) are correlated between particle types and largely cancel out in the fractions. As a result, uncertainties in the fractions are predominantly statistical over almost the entire momentum range.

The unfolding technique worked for the momentum distribution up to $z = 0.5$, but gave slightly larger errors than the fitting method. In the region of overlap, the two methods gave almost identical results as illustrated in Fig. 28 for the particle fractions.

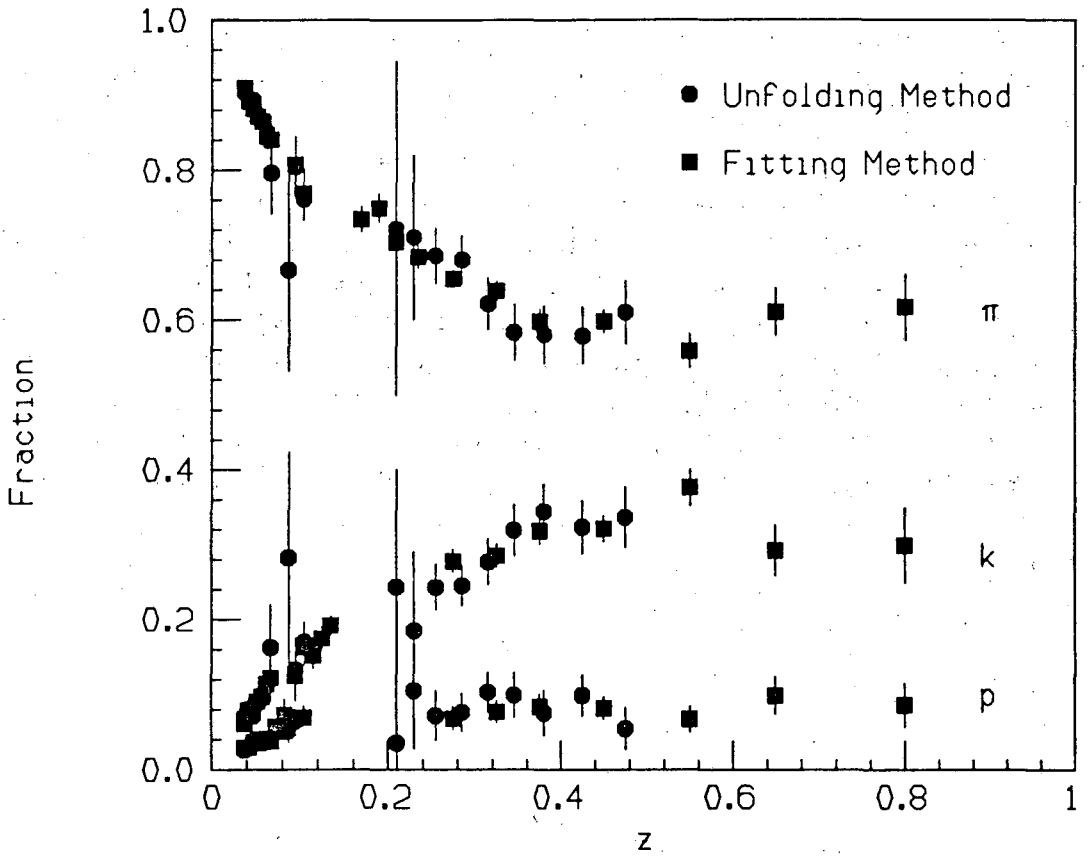

Figure 28: Comparison of the charged hadron fractions as a function of scaled momentum using the unfolding and fitting methods of data analysis.

5.4 Comparison of results to previous work

No experiment so far has measured the π,k,p cross sections as a function of all the variables explored here. However, measurements of π,k,p cross sections as a function of momentum exist from TPC using the older data set, from TASSO for the large x region based on TOF and Cherenkov techniques, and from several other detectors for the low x region using TOF only. Furthermore, rapidity distributions have been published assuming that all charged hadrons are pions. In this section we compare our data with these limited existing measurements. In all cases where pion, kaon, and proton cross sections appear in the same plot, the kaon cross section has been divided by 10 and the proton cross section by 100 so that the distributions are clearly separated. All points are placed in the centers of the bins. Our binsizes were chosen according to a criteria which we discuss in the following section.

The TPC group previously published the invariant cross section $(1/\beta\sigma)(d\sigma/dx)$, where $x = 2E/\sqrt{s}$, and the particle fractions as a function of momentum for the 1982/83 data sample [31]. A technique of fitting the dE/dx distribution in fixed momentum intervals was used for the analysis. Fig. 29 shows comparisons of the old cross sections and the present ones. The newer 1984/86 data set with the improved momentum resolution allows much finer binning. Overall, the agreement is very good. Fig. 30 shows the particle fractions as a function of $z = 2p/\sqrt{s}$ for the old and new data sets. Again, the results are entirely consistent.

A comparison of our pion, kaon, and proton cross sections $(1/\beta\sigma)(d\sigma/dx)$ to those of TASSO, HRS, and Mark II is shown in Fig. 31. All errors are statistical and systematic combined. The TASSO [32] $(s/\beta)(d\sigma/dx)$ cross sections were converted to $(1/\beta\sigma)(d\sigma/dx)$ using $s = (34\ \mathrm{GeV})^2$, $\sigma(\mathrm{e^+e^-} \rightarrow \mu^+\mu^-) = 0.0868/s\ \mu\mathrm{b}$ (s in GeV^2), and the MAC [33] value of $R = 3.96$ (error neglected). The momentum bins were converted to π, k, and p x-bins, where $x = 2E/\sqrt{s}$. In the low energy region, HRS [34] has published π,k,p cross sections and Mark II [35] has published k cross sections. Overall, the agreement is good.

Fig. 32 compares our particle fractions as a function of scaled momentum $z = 2p/\sqrt{s}$ to those of TASSO [32] and HRS [34]. TASSO's kaon fraction is higher at low z than ours and HRS's.

The TPC and TASSO [32] π, k, and p momentum distributions $(1/\sigma)(d\sigma/dz)$, $z = 2p/\sqrt{s}$, are shown in Fig. 33. The errors are statistical and systematic combined. The TASSO $(s)(d\sigma/dp)$ cross sections were converted to $(1/\sigma)(d\sigma/dz)$ in the manner indicated above for the energy distribution. The discrepancy in the low momentum kaon cross section is clearly visible, although the overall agreement is very good.

Other detectors have made measurements of inclusive charged hadron momentum distributions with no particle identification, but with very high precision. We compare with those measurements by adding our corrected numbers of $\pi^\pm$, $\mathrm{k}^\pm$, and $\mathrm{p}(\bar{\mathrm{p}})$ before we compute the cross sections. Fig. 34 compares our charged hadron cross section $(1/\sigma)(d\sigma/dz)$ as a function of $z = 2p/\sqrt{s}$ to that of TASSO [36] and Mark II [37]. The TASSO errors are statistical only, with the systematic errors estimated to be of the same order. The Mark II errors are also statistical only.

Their systematic error is estimated to be between 6% at low z and 10% at high z. The agreement is very good.

Our charged hadron rapidity distribution $(1/\sigma)(d\sigma/d|y|)$ using the thrust axis is compared to that of TASSO [36] and Mark II [38] in Fig. 35. We used the y_π bins and added the numbers of $\pi^\pm$, $k^\pm$, and $p(\bar{p})$ before computing the cross section. Thus, all particles were considered pions when computing the rapidity in all three analyses. The TPC errors are statistical and systematic combined. The TASSO errors are statistical only. Their systematic errors are estimated to be of the same order as the statistical errors. The Mark II errors are statistical and systematic combined. The TASSO cross section extends to higher y, consistent with their higher energy of 34 GeV.

In Fig. 36 our charged hadron p_t distribution is compared to TASSO [36] and Mark II [38] using the sphericity axis. At low p_t the agreement is very good, but at higher p_t the TASSO cross section is larger, consistent with their higher energy. The TPC and Mark II errors are statistical and systematic combined, and the TASSO errors are statistical only with the systematic errors estimated to be of the same order as the statistical errors, although the error bars in the plot are smaller than the symbols and are not visible.

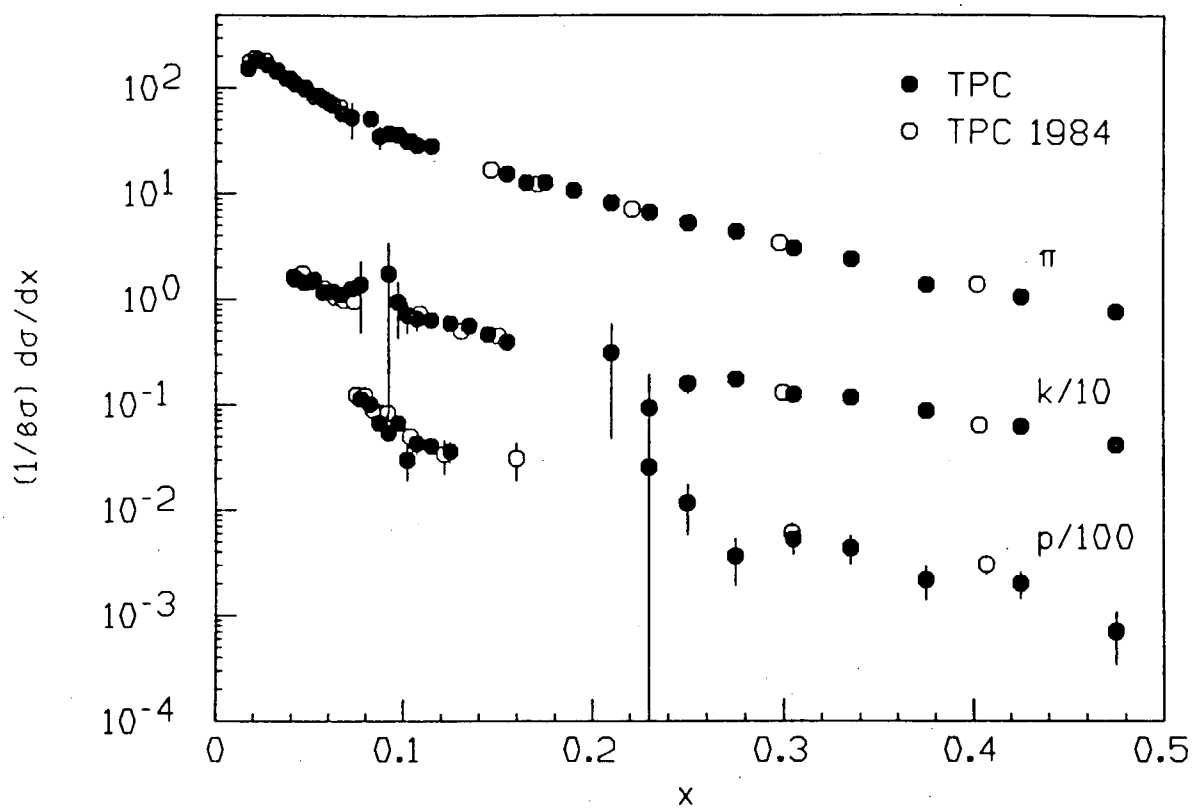

Figure 29: Comparison of the $(1/\beta\sigma)(d\sigma/dx)$ cross sections from the 1982/83 running period and the more recent 1984/86 running period. The kaon cross sections have been divided by 10 and the proton cross sections by 100 for separation.

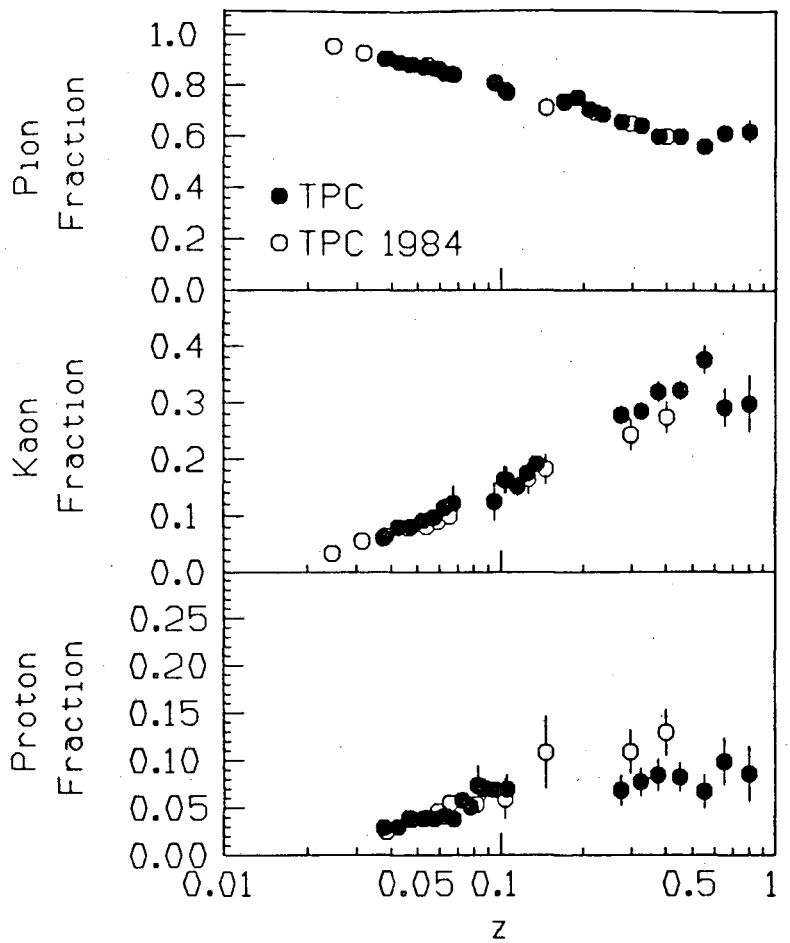

Figure 30: Comparison of the charged hadron fractions as a function of $z = 2p/\sqrt{s}$ for the old and new data sets.

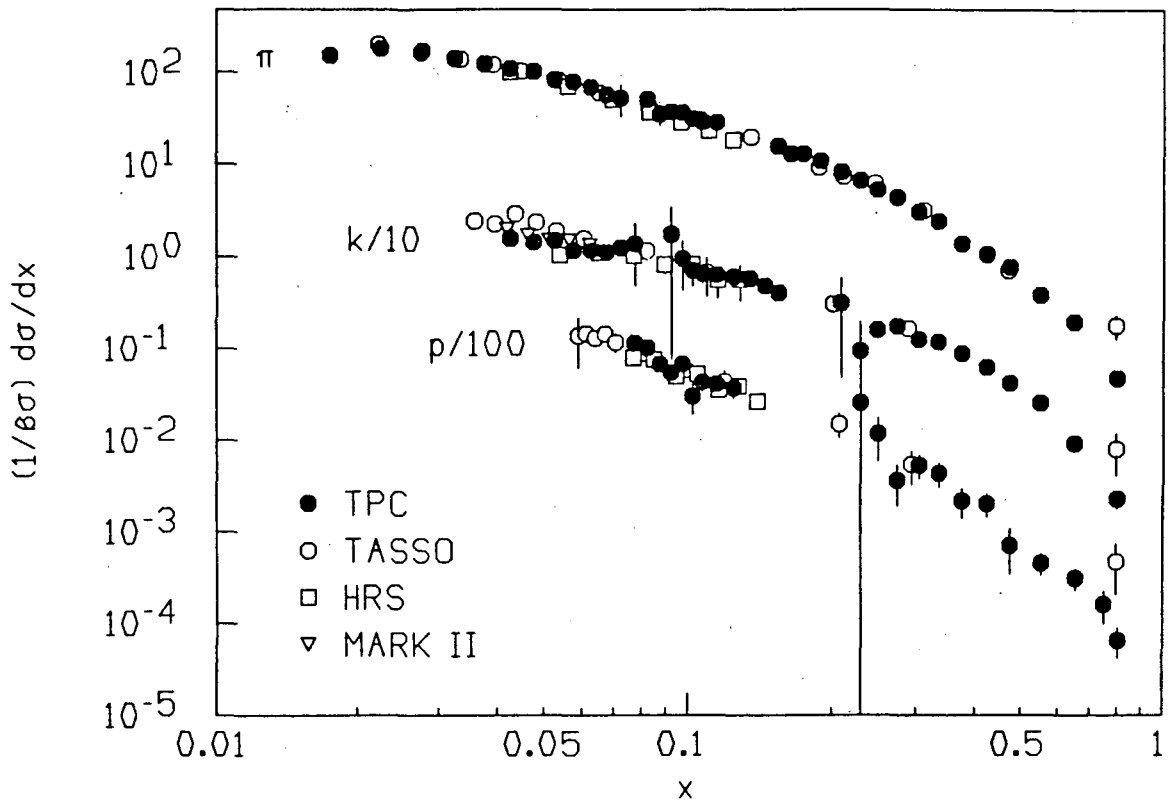

Figure 31: Comparison to TASSO and HRS of the $(1/\beta\sigma)(d\sigma/dx)$ cross sections for pions, kaons, and protons. Also shown is the kaon cross section from Mark II. The kaon cross section has been divided by 10 and the proton cross section by 100 for separation.

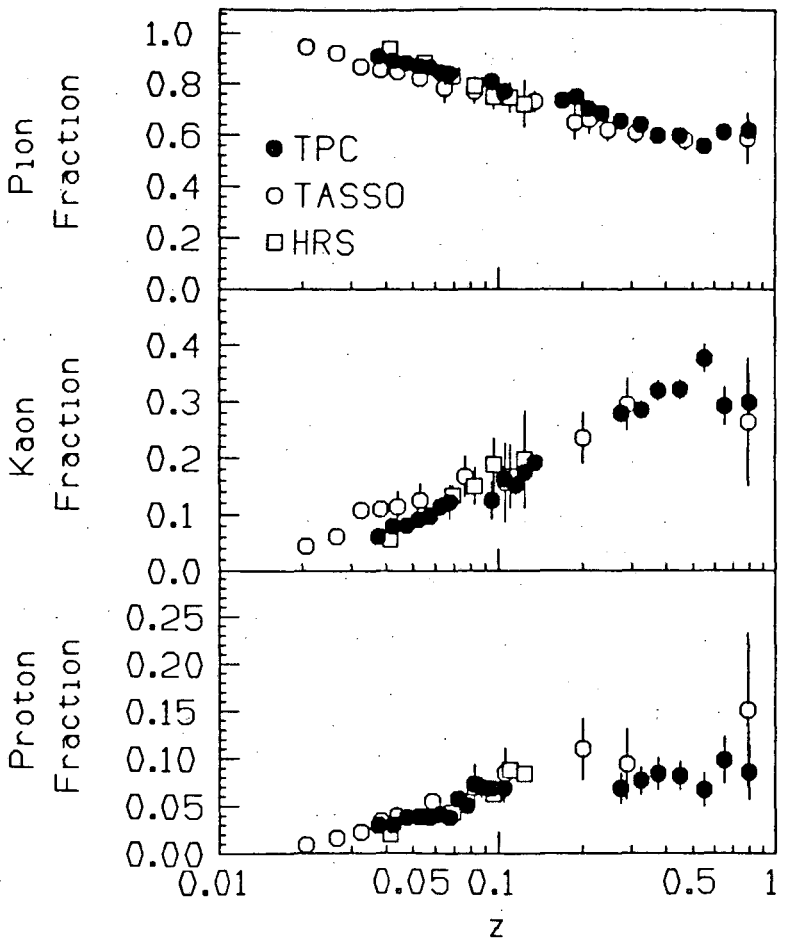

Figure 32: Comparison to TASSO and HRS of the pion, kaon, and proton fractions as a function of scaled momentum $z = 2p/\sqrt{s}$.

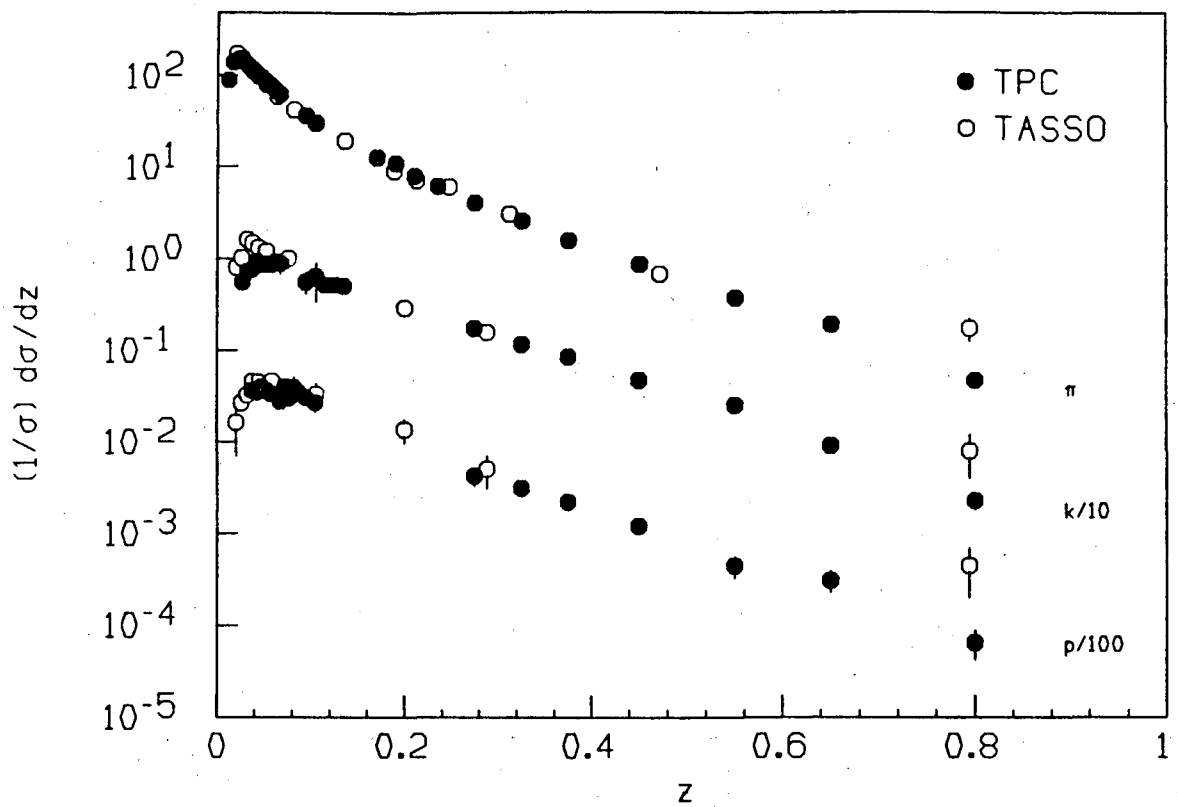

Figure 33: Comparison to TASSO of the π, k, and p momentum distributions $(1/\sigma)(d\sigma/dz)$, $z = 2p/\sqrt{s}$. The kaon cross section has been divided by 10 and the proton cross section by 100 for separation.

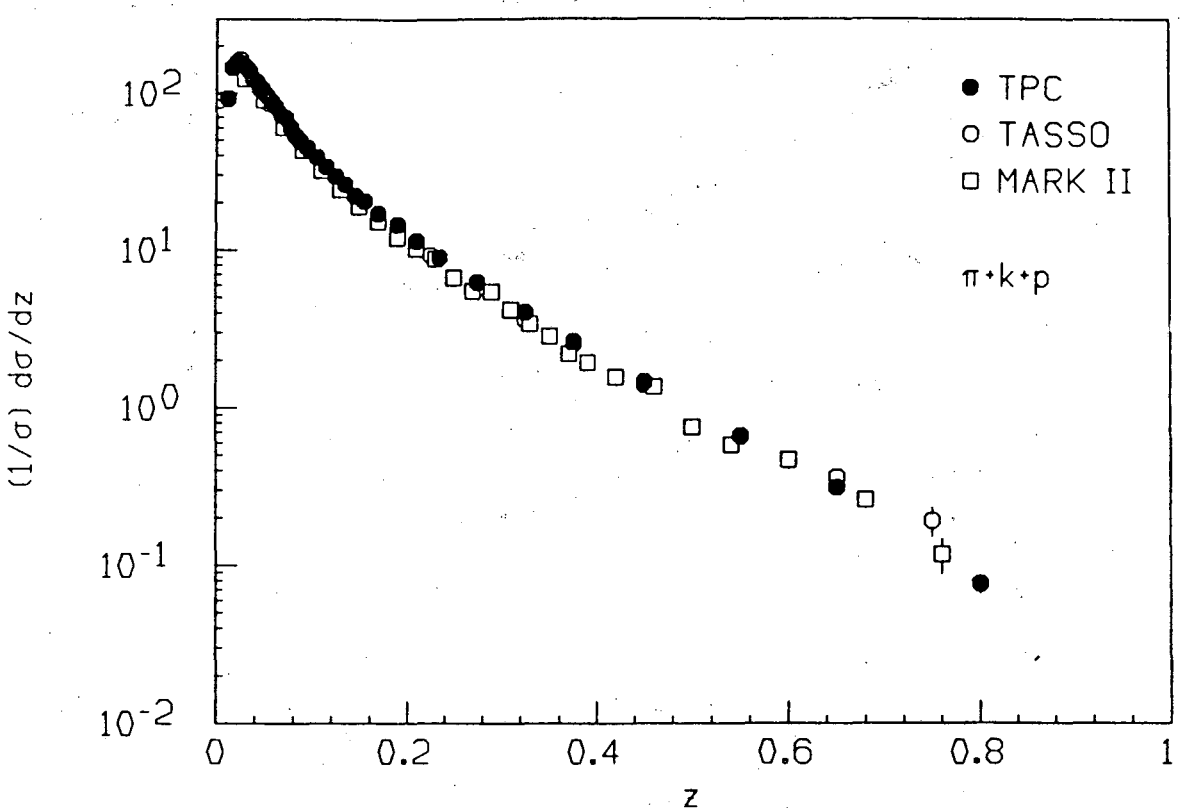

Figure 34: Comparison to TASSO and Mark II of the total charged hadron cross section $(1/\sigma)(d\sigma/dz)$ as a function of scaled momentum $z = 2p/\sqrt{s}$.

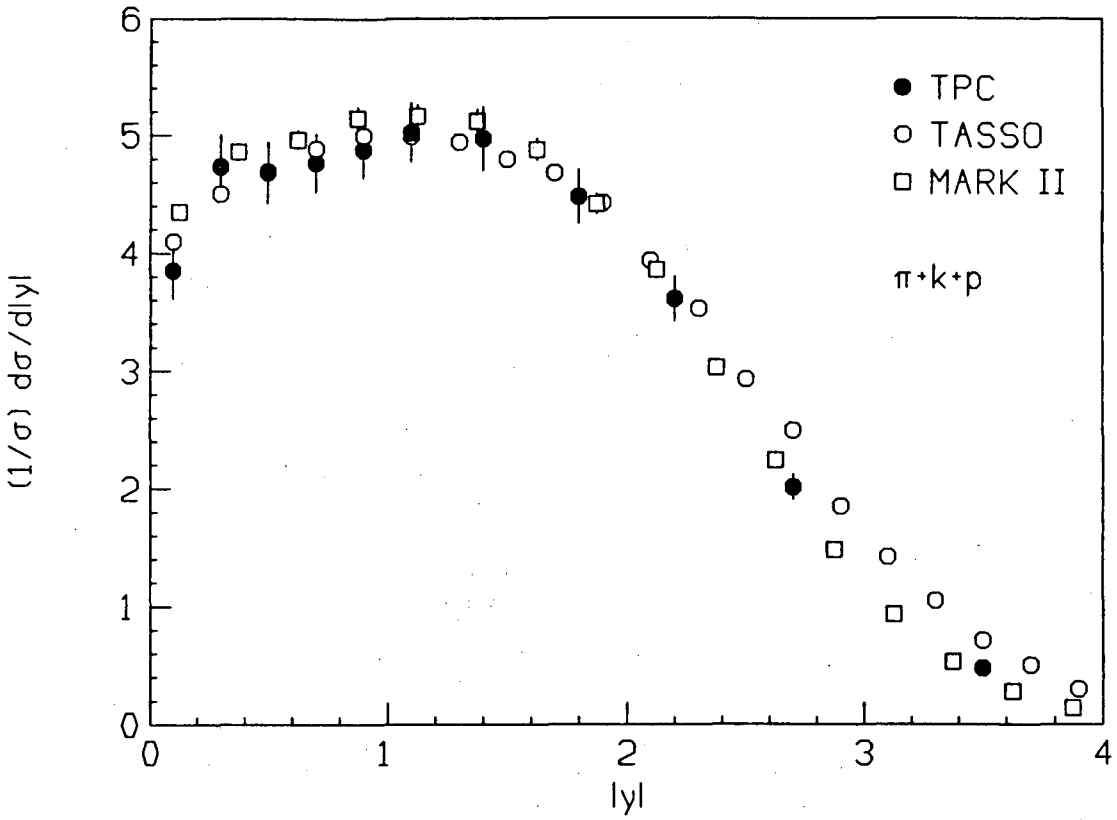

Figure 35: Comparison to TASSO and Mark II of the total charged hadron cross section $(1/\sigma)(d\sigma/d|y|)$ as a function of rapidity using the thrust axis.

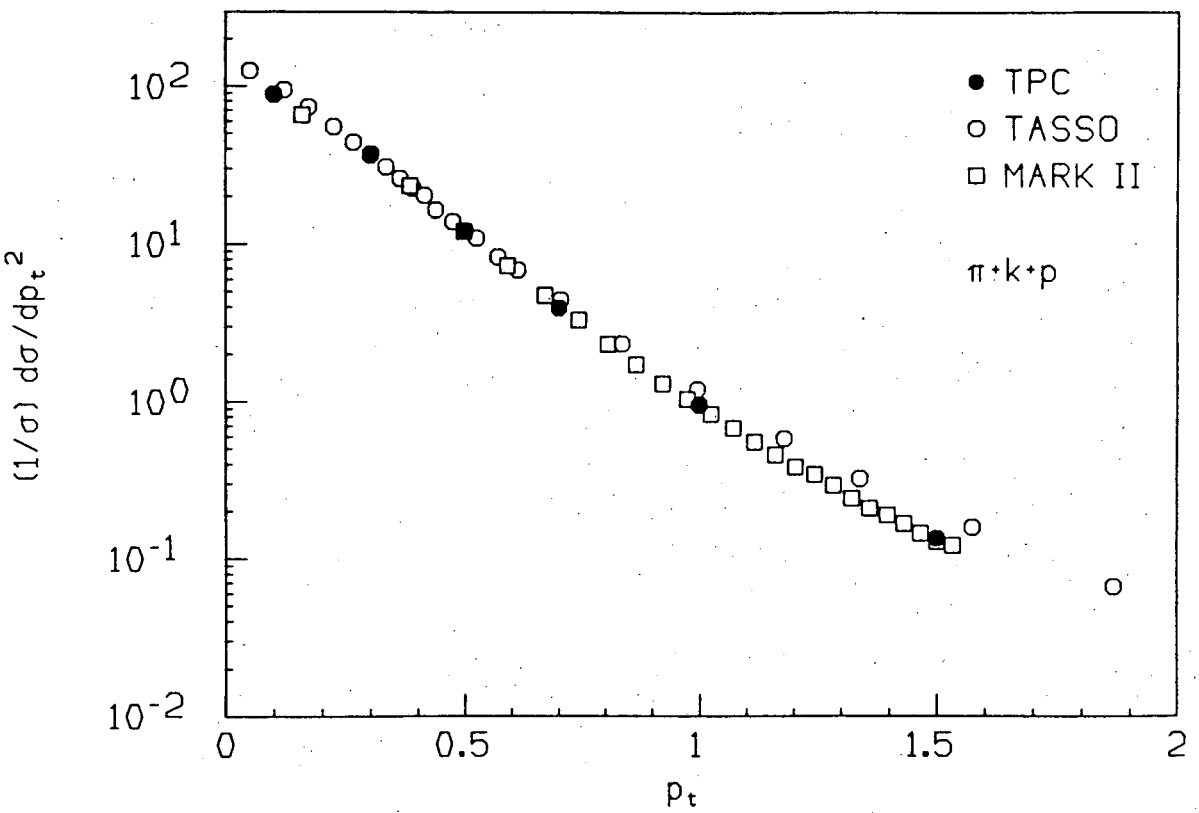

Figure 36: Comparison to TASSO and Mark II of the charged hadron cross section $(1/\sigma)(d\sigma/dp_t^2)$ as a function of p_t using the sphericity axis.

6 RESULTS

6.1 Values of cross sections and particle fractions

The results of the cross section and particle fraction measurements are presented below. In order to avoid an additional unfolding of the experimental resolution, the bin widths in the various variables were chosen such that at least 70% of the particles measured in a certain bin actually belonged in the bin as determined by the Monte Carlo[1]. Remaining small corrections are included in the acceptance correction factors. For the x and z distributions, the bin widths were dominated by the momentum resolution, whereas for the y, p_t, and yp_t distributions, the bin widths were determined largely by the error in the direction of the event axis.

Table 3 contains the measured cross sections $(1/\beta\sigma)(d\sigma/dx)$ for pions, kaons, and protons, where $x = 2\sqrt{p^2+m^2}/\sqrt{s}$. In computing the cross sections, $(1/\sigma)(d\sigma/dx)$ was measured directly and was multiplied by $\langle 1/\beta \rangle$ to remove phase space effects. The $\langle 1/\beta \rangle$ for each bin was obtained from a fit to the data. Table 4 contains the values used. The minimum kinematically allowed x values for pions, kaons, and protons are respectively 0.0096, 0.0341, and 0.0647. With the $p \geq 0.15$ GeV/c cut, the minimum measured x values for pions, kaons, and protons are respectively 0.0141, 0.0356, and 0.0655. Also shown in Table 3 are the measured particle fractions for each bin. The π-k, π-p, and k-p crossovers occur at $x \simeq 0.08$, $x \simeq 0.13$, and $x \simeq 0.17$, respectively, accounting for the missing data points. Cross sections and particle fractions for $x < 0.5$ were determined by the unfolding technique, and for $x > 0.5$ by the technique of fitting the dE/dx spectrum.

The results for the z-distributions $(z/\sigma)(d\sigma/dz)$, where $z = 2p/\sqrt{s}$, are given in Table 5 along with the particle fractions. With the $p \geq 0.15$ GeV/c cut, the minimum measured z value is 1.03×10^{-2}. Kaons are missing for $z < 0.025$ and protons are missing for $z < 0.035$ because most of them can not make it through the material in front of the TPC. The z range from 0.070 to 0.090 is the π-k crossover region, from 0.11 to 0.16 is the π-p crossover region, and from 0.14 to 0.25 is the k-p crossover region. The cross sections and fractions as a function of z were found by the technique of fitting the dE/dx spectrum. The cross section $(1/\sigma)(d\sigma/dz)$ was measured directly and was multiplied by $\langle z \rangle$. The $\langle z \rangle$ values were determined by a fit to all charged particles. For each channel, we used the same $\langle z \rangle$ value given in Table 6 for all three species.

The measured rapidity distributions $(1/\sigma)(d\sigma/d|y|)$ and particle fractions as a function of $|y|$, where $y = (1/2)\ln((E+p_{\|})/(E-p_{\|}))$, are given in Table 7. The sphericity axis computed from the charged particles was used as the event axis. The absolute value of the rapidity is used to improve statistics, since the distribution is symmetric about $y = 0$. Table 8 is the corresponding table using the thrust axis. The large dip at $y = 0$ with the thrust axis is expected from the discussion of section

[1]The 70% criteria applied to the sphericity axis for y and p_t. The same bins were used for thrust as for sphericity, violating the criteria in some cases.

5.1.

Table 9 contains the cross sections $(1/\sigma)(d\sigma/dp_t^2)$ and particle fractions as a function of p_t using the sphericity axis. The denominator of the cross section was computed by taking the difference of the squares of the endpoints of each bin, giving the distribution in dp_t^2 even though the independent variable is p_t. A combination of particle misidentification and few high-p_t particles with the sphericity axis made the maximum p_t values for which the cross section could be measured 3.0 GeV/c and 1.8 GeV/c, respectively, for kaons and protons. The corresponding table using the thrust axis is Table 10.

The values of the double differential cross sections $(1/\sigma)(d\sigma/d|y|dp_t^2)$ and particle fractions as a function of p_t for different ranges of $|y|$ are given in Tables 11(a-d). The event axis is the sphericity axis. At low $|y|$ the improved resolution allowed finer binning than at large $|y|$. The binsizes were chosen so p_t bins with $0 < |y| < 1$ could be combined to give the cross section in the bins used for $|y| > 1$. At high $|y|$, much of the p_t range is excluded as shown in Fig. 37, where the shaded regions are kinematically forbidden. The corresponding numbers using the thrust axis are given in Table 12(a-d).

The hadron multiplicities were determined from the unfolding technique by summing the corrected number of particles at the vertex in each bin V_i ($i = \pi$,k,p) over all bins. The rapidity and p_t distributions (with bins at large $|y|$ and p_t so the full kinematically allowed range was covered) were used, and they gave consistent results. We determined the $\pi^{\pm}$, $k^{\pm}$, and $p(\bar{p})$ multiplicities to be 10.6 ± 0.6, 1.43 ± 0.09, and 0.53 ± 0.07, respectively. Both statistical and systematic errors are combined.

x range	$e^+e^- \to \pi^\pm + X$		$e^+e^- \to k^\pm + X$		$e^+e^- \to p^\pm + X$	
	π fraction %	$\langle\frac{1}{\beta}\rangle\frac{1}{\sigma}\frac{d\sigma_\pi}{dx}$	k fraction %	$\langle\frac{1}{\beta}\rangle\frac{1}{\sigma}\frac{d\sigma_k}{dx}$	p fraction %	$\langle\frac{1}{\beta}\rangle\frac{1}{\sigma}\frac{d\sigma_p}{dx}$
0.015 – 0.020	100.0 ± 0.0	$(1.53 \pm 0.12) \times 10^2$	–	–	–	–
0.020 – 0.025	100.0 ± 0.0	$(1.83 \pm 0.11) \times 10^2$	–	–	–	–
0.025 – 0.030	100.0 ± 0.0	$(1.65 \pm 0.09) \times 10^2$	–	–	–	–
0.030 – 0.035	–	$(1.42 \pm 0.08) \times 10^2$	–	–	–	–
0.035 – 0.040	–	$(1.23 \pm 0.07) \times 10^2$	–	–	–	–
0.040 – 0.045	91.9 ± 0.8	$(1.09 \pm 0.06) \times 10^2$	8.1 ± 0.8	$(1.56 \pm 0.15) \times 10^1$	–	–
0.045 – 0.050	90.8 ± 0.9	$(1.01 \pm 0.06) \times 10^2$	9.2 ± 0.9	$(1.44 \pm 0.12) \times 10^1$	–	–
0.050 – 0.055	87.7 ± 1.5	$(8.36 \pm 0.48) \times 10^1$	12.3 ± 1.5	$(1.52 \pm 0.19) \times 10^1$	–	–
0.055 – 0.060	89.2 ± 1.6	$(7.85 \pm 0.45) \times 10^1$	10.8 ± 1.6	$(1.17 \pm 0.18) \times 10^1$	–	–
0.060 – 0.065	–	$(6.87 \pm 0.41) \times 10^1$	–	$(1.18 \pm 0.11) \times 10^1$	–	–
0.065 – 0.070	–	$(5.72 \pm 0.40) \times 10^1$	–	$(1.10 \pm 0.12) \times 10^1$	–	–
0.070 – 0.075	–	$(5.26 \pm 1.95) \times 10^1$	–	$(1.24 \pm 0.21) \times 10^1$	–	–
0.075 – 0.080	–	–	–	$(1.36 \pm 0.89) \times 10^1$	–	$(1.14 \pm 0.12) \times 10^1$
0.080 – 0.085	–	$(5.08 \pm 0.31) \times 10^1$	–	–	–	$(1.01 \pm 0.11) \times 10^1$
0.085 – 0.090	–	$(3.49 \pm 0.88) \times 10^1$	–	–	–	$(6.71 \pm 0.74) \times 10^0$
0.090 – 0.095	64.9 ± 17.7	$(3.71 \pm 0.35) \times 10^1$	28.3 ± 19.5	$(1.73 \pm 1.66) \times 10^1$	6.8 ± 2.0	$(5.42 \pm 0.62) \times 10^0$
0.095 – 0.100	72.2 ± 7.2	$(3.61 \pm 0.26) \times 10^1$	17.8 ± 8.0	$(9.43 \pm 5.15) \times 10^0$	10.1 ± 1.6	$(6.71 \pm 0.85) \times 10^0$
0.100 – 0.105	77.5 ± 4.7	$(3.10 \pm 0.22) \times 10^1$	16.7 ± 4.6	$(7.05 \pm 2.29) \times 10^0$	5.8 ± 2.1	$(3.00 \pm 1.11) \times 10^0$
0.105 – 0.110	74.9 ± 3.4	$(2.87 \pm 0.22) \times 10^1$	16.2 ± 3.2	$(6.50 \pm 1.48) \times 10^0$	8.9 ± 1.9	$(4.27 \pm 0.94) \times 10^0$
0.110 – 0.120	74.9 ± 2.4	$(2.80 \pm 0.20) \times 10^1$	16.2 ± 2.3	$(6.32 \pm 0.97) \times 10^0$	9.0 ± 1.1	$(4.05 \pm 0.50) \times 10^0$
0.120 – 0.130	–	–	–	$(5.87 \pm 0.79) \times 10^0$	–	$(3.60 \pm 0.85) \times 10^0$
0.130 – 0.140	–	–	–	$(5.57 \pm 0.71) \times 10^0$	–	–
0.140 – 0.150	–	–	–	$(4.67 \pm 0.61) \times 10^0$	–	–
0.150 – 0.160	–	$(1.54 \pm 0.11) \times 10^1$	–	$(3.93 \pm 0.63) \times 10^0$	–	–
0.160 – 0.170	–	$(1.27 \pm 0.09) \times 10^1$	–	–	–	–
0.170 – 0.180	–	$(1.28 \pm 0.09) \times 10^1$	–	–	–	–
0.180 – 0.200	–	$(1.07 \pm 0.07) \times 10^1$	–	–	–	–
0.200 – 0.220	–	$(8.17 \pm 0.56) \times 10^0$	–	$(3.12 \pm 2.64) \times 10^0$	–	–
0.220 – 0.240	66.4 ± 20.5	$(6.64 \pm 0.47) \times 10^0$	9.2 ± 9.4	$(9.27 \pm 10.0) \times 10^{-1}$	24.4 ± 22.2	$(2.54 \pm 3.03) \times 10^0$
0.240 – 0.260	66.2 ± 5.6	$(5.26 \pm 0.39) \times 10^0$	19.7 ± 3.5	$(1.58 \pm 0.31) \times 10^0$	14.1 ± 6.1	$(1.16 \pm 0.58) \times 10^0$
0.260 – 0.290	67.9 ± 3.2	$(4.36 \pm 0.31) \times 10^0$	26.7 ± 2.8	$(1.73 \pm 0.21) \times 10^0$	5.4 ± 2.4	$(3.58 \pm 1.68) \times 10^{-1}$
0.290 – 0.320	63.4 ± 3.5	$(3.01 \pm 0.23) \times 10^0$	25.9 ± 3.0	$(1.24 \pm 0.16) \times 10^0$	10.8 ± 2.9	$(5.23 \pm 1.52) \times 10^{-1}$
0.320 – 0.350	60.2 ± 3.6	$(2.38 \pm 0.19) \times 10^0$	29.2 ± 3.2	$(1.16 \pm 0.15) \times 10^0$	10.6 ± 3.0	$(4.30 \pm 1.30) \times 10^{-1}$
0.350 – 0.400	55.9 ± 3.6	$(1.35 \pm 0.11) \times 10^0$	35.4 ± 3.4	$(8.60 \pm 1.05) \times 10^{-1}$	8.7 ± 2.9	$(2.14 \pm 0.76) \times 10^{-1}$
0.400 – 0.450	56.3 ± 3.8	$(1.03 \pm 0.10) \times 10^0$	33.0 ± 3.6	$(6.09 \pm 0.81) \times 10^{-1}$	10.7 ± 2.8	$(1.98 \pm 0.56) \times 10^{-1}$
0.450 – 0.500	61.2 ± 4.2	$(7.55 \pm 0.76) \times 10^{-1}$	33.2 ± 4.0	$(4.10 \pm 0.62) \times 10^{-1}$	5.6 ± 2.7	$(6.97 \pm 3.57) \times 10^{-2}$
0.500 – 0.600	55.8 ± 2.3	$(3.70 \pm 0.22) \times 10^{-1}$	37.5 ± 2.5	$(2.50 \pm 0.20) \times 10^{-1}$	6.7 ± 1.8	$(4.49 \pm 1.20) \times 10^{-2}$
0.600 – 0.700	61.0 ± 3.2	$(1.90 \pm 0.15) \times 10^{-1}$	29.1 ± 3.4	$(9.07 \pm 1.17) \times 10^{-2}$	9.8 ± 2.5	$(3.08 \pm 0.81) \times 10^{-2}$
0.700 – 0.900	61.7 ± 4.5	$(4.66 \pm 0.70) \times 10^{-2}$	29.8 ± 5.0	$(2.25 \pm 0.48) \times 10^{-2}$	8.5 ± 2.9	$(6.49 \pm 2.29) \times 10^{-3}$

Table 3: Table of the measured cross sections $\langle 1/\beta \rangle (1/\sigma)(d\sigma/dx)$ and particle fractions for pions, kaons, and protons as a function of $x = 2E/\sqrt{s}$.

x-range	pion $\langle\frac{1}{\beta}\rangle$	kaon $\langle\frac{1}{\beta}\rangle$	proton $\langle\frac{1}{\beta}\rangle$
0.015-0.020	1.204	-	-
0.020-0.025	1.108	-	-
0.025-0.030	1.068	-	-
0.030-0.035	1.047	-	-
0.035-0.040	1.035	-	-
0.040-0.045	1.027	1.683	-
0.045-0.050	1.021	1.438	-
0.050-0.055	1.017	1.316	-
0.055-0.060	1.015	1.242	-
0.060-0.065	1.012	1.193	-
0.065-0.070	1.011	1.159	-
0.070-0.075	1.009	1.133	-
0.075-0.080	1.008	1.114	1.827
0.080-0.085	1.007	1.098	1.616
0.085-0.090	1.006	1.086	1.488
0.090-0.095	1.006	1.076	1.401
0.095-0.100	1.005	1.067	1.338
0.100-0.105	1.004	1.060	1.290
0.105-0.110	1.004	1.054	1.253
0.110-0.120	1.004	1.047	1.211
0.120-0.130	1.003	1.039	1.170
0.130-0.140	1.003	1.034	1.140
0.140-0.150	1.002	1.029	1.118
0.150-0.160	1.002	1.025	1.101
0.160-0.170	1.002	1.022	1.087
0.170-0.180	1.002	1.020	1.076
0.180-0.200	1.001	1.017	1.064
0.200-0.220	1.001	1.013	1.051
0.220-0.240	1.001	1.011	1.042
0.240-0.260	1.001	1.009	1.035
0.260-0.290	1.001	1.008	1.029
0.290-0.320	1.000	1.006	1.023
0.320-0.350	1.000	1.005	1.019
0.350-0.400	1.000	1.004	1.015
0.400-0.450	1.000	1.003	1.012
0.450-0.500	1.000	1.003	1.009
0.500-0.600	1.000	1.002	1.007
0.600-0.700	1.000	1.001	1.005
0.700-0.900	1.000	1.001	1.004

Table 4: Table of the $\langle 1/\beta \rangle$ values used in Table 3.

z range	$e^+e^- \to \pi^\pm + X$		$e^+e^- \to k^\pm + X$		$e^+e^- \to p^\pm + X$	
	π fraction %	$\langle z \rangle \frac{1}{\sigma} \frac{d\sigma_\pi}{dz}$	k fraction %	$\langle z \rangle \frac{1}{\sigma} \frac{d\sigma_k}{dz}$	p fraction %	$\langle z \rangle \frac{1}{\sigma} \frac{d\sigma_p}{dz}$
0.010 – 0.015	–	$(1.12 \pm 0.09) \times 10^0$	–	–	–	–
0.015 – 0.020	–	$(2.43 \pm 0.10) \times 10^0$	–	–	–	–
0.020 – 0.025	–	$(3.36 \pm 0.15) \times 10^0$	–	–	–	–
0.025 – 0.030	–	$(3.96 \pm 0.14) \times 10^0$	–	$(1.53 \pm 0.14) \times 10^{-1}$	–	–
0.030 – 0.035	–	$(4.25 \pm 0.13) \times 10^0$	–	$(2.34 \pm 0.18) \times 10^{-1}$	–	–
0.035 – 0.040	91.0 ± 0.7	$(4.23 \pm 0.13) \times 10^0$	6.1 ± 0.4	$(2.84 \pm 0.22) \times 10^{-1}$	2.9 ± 0.5	$(1.36 \pm 0.24) \times 10^{-1}$
0.040 – 0.045	89.2 ± 1.0	$(4.44 \pm 0.14) \times 10^0$	7.9 ± 0.9	$(3.93 \pm 0.51) \times 10^{-1}$	2.9 ± 0.4	$(1.47 \pm 0.20) \times 10^{-1}$
0.045 – 0.050	88.2 ± 0.9	$(4.45 \pm 0.14) \times 10^0$	8.0 ± 0.8	$(4.05 \pm 0.46) \times 10^{-1}$	3.8 ± 0.4	$(1.89 \pm 0.22) \times 10^{-1}$
0.050 – 0.055	87.1 ± 0.7	$(4.40 \pm 0.14) \times 10^0$	9.1 ± 0.6	$(4.58 \pm 0.34) \times 10^{-1}$	3.8 ± 0.4	$(1.91 \pm 0.22) \times 10^{-1}$
0.055 – 0.060	86.5 ± 0.9	$(4.37 \pm 0.14) \times 10^0$	9.7 ± 0.8	$(4.87 \pm 0.42) \times 10^{-1}$	3.8 ± 0.4	$(1.92 \pm 0.22) \times 10^{-1}$
0.060 – 0.065	84.5 ± 1.7	$(4.26 \pm 0.16) \times 10^0$	11.4 ± 1.6	$(5.74 \pm 0.84) \times 10^{-1}$	4.1 ± 0.5	$(2.07 \pm 0.25) \times 10^{-1}$
0.065 – 0.070	84.0 ± 3.1	$(4.11 \pm 0.20) \times 10^0$	12.2 ± 3.1	$(5.95 \pm 1.53) \times 10^{-1}$	3.8 ± 0.4	$(1.86 \pm 0.22) \times 10^{-1}$
0.070 – 0.075	–	–	–	–	5.8 ± 0.7	$(2.89 \pm 0.35) \times 10^{-1}$
0.075 – 0.080	–	–	–	–	5.1 ± 0.9	$(2.35 \pm 0.45) \times 10^{-1}$
0.080 – 0.085	–	–	–	–	7.3 ± 2.1	$(3.21 \pm 0.98) \times 10^{-1}$
0.085 – 0.090	–	–	–	–	7.0 ± 1.1	$(3.00 \pm 0.50) \times 10^{-1}$
0.090 – 0.100	80.7 ± 3.5	$(3.41 \pm 0.18) \times 10^0$	12.5 ± 3.3	$(5.27 \pm 1.39) \times 10^{-1}$	6.9 ± 0.7	$(2.90 \pm 0.31) \times 10^{-1}$
0.100 – 0.110	76.9 ± 3.2	$(3.14 \pm 0.16) \times 10^0$	16.2 ± 2.3	$(6.63 \pm 0.97) \times 10^{-1}$	6.9 ± 1.5	$(2.83 \pm 0.63) \times 10^{-1}$
0.110 – 0.120	–	–	15.1 ± 1.7	$(5.89 \pm 0.70) \times 10^{-1}$	–	–
0.120 – 0.130	–	–	17.5 ± 1.6	$(6.40 \pm 0.61) \times 10^{-1}$	–	–
0.130 – 0.140	–	–	19.1 ± 1.3	$(6.74 \pm 0.52) \times 10^{-1}$	–	–
0.140 – 0.150	–	–	–	–	–	–
0.150 – 0.160	–	–	–	–	–	–
0.160 – 0.180	73.4 ± 1.6	$(2.12 \pm 0.09) \times 10^0$	–	–	–	–
0.180 – 0.200	74.8 ± 1.9	$(2.04 \pm 0.08) \times 10^0$	–	–	–	–
0.200 – 0.220	70.3 ± 1.6	$(1.67 \pm 0.08) \times 10^0$	–	–	–	–
0.220 – 0.250	68.4 ± 1.6	$(1.44 \pm 0.06) \times 10^0$	–	–	–	–
0.250 – 0.300	65.4 ± 1.1	$(1.11 \pm 0.04) \times 10^0$	27.8 ± 1.6	$(4.73 \pm 0.29) \times 10^{-1}$	6.8 ± 1.6	$(1.16 \pm 0.27) \times 10^{-1}$
0.300 – 0.350	63.9 ± 1.3	$(8.43 \pm 0.32) \times 10^{-1}$	28.5 ± 1.6	$(3.76 \pm 0.24) \times 10^{-1}$	7.7 ± 1.5	$(1.01 \pm 0.20) \times 10^{-1}$
0.350 – 0.400	59.8 ± 1.7	$(5.88 \pm 0.26) \times 10^{-1}$	31.8 ± 1.8	$(3.13 \pm 0.20) \times 10^{-1}$	8.4 ± 1.7	$(8.27 \pm 1.70) \times 10^{-2}$
0.400 – 0.500	59.7 ± 1.5	$(3.88 \pm 0.17) \times 10^{-1}$	32.1 ± 1.7	$(2.08 \pm 0.13) \times 10^{-1}$	8.2 ± 1.5	$(5.31 \pm 0.98) \times 10^{-2}$
0.500 – 0.600	55.8 ± 2.3	$(2.00 \pm 0.12) \times 10^{-1}$	37.5 ± 2.5	$(1.35 \pm 0.11) \times 10^{-1}$	6.7 ± 1.8	$(2.40 \pm 0.64) \times 10^{-2}$
0.600 – 0.700	61.0 ± 3.2	$(1.21 \pm 0.10) \times 10^{-1}$	29.1 ± 3.4	$(5.79 \pm 0.75) \times 10^{-2}$	9.8 ± 2.5	$(1.95 \pm 0.51) \times 10^{-2}$
0.700 – 0.900	61.7 ± 4.5	$(3.59 \pm 0.54) \times 10^{-2}$	29.8 ± 5.0	$(1.73 \pm 0.37) \times 10^{-2}$	8.5 ± 2.9	$(4.96 \pm 1.75) \times 10^{-3}$

Table 5: Table of the measured cross sections $\langle z \rangle (1/\sigma)(d\sigma/dz)$ and particle fractions for pions, kaons, and protons as a function of $z = 2p/\sqrt{s}$.

z-range	$\langle z \rangle$
0.010 - 0.015	0.0126
0.015 - 0.020	0.0175
0.020 - 0.025	0.0225
0.025 - 0.030	0.0275
0.030 - 0.035	0.0325
0.035 - 0.040	0.0374
0.040 - 0.045	0.0424
0.045 - 0.050	0.0474
0.050 - 0.055	0.0525
0.055 - 0.060	0.0575
0.060 - 0.065	0.0625
0.065 - 0.070	0.0675
0.070 - 0.075	0.0724
0.075 - 0.080	0.0775
0.080 - 0.085	0.0825
0.085 - 0.090	0.0875
0.090 - 0.100	0.0948
0.100 - 0.110	0.1049
0.110 - 0.120	0.1149
0.120 - 0.130	0.1248
0.130 - 0.140	0.1349
0.140 - 0.150	0.1448
0.150 - 0.160	0.1550
0.160 - 0.180	0.1699
0.180 - 0.200	0.1896
0.200 - 0.220	0.2095
0.220 - 0.250	0.2346
0.250 - 0.300	0.2728
0.300 - 0.350	0.3236
0.350 - 0.400	0.3722
0.400 - 0.500	0.4438
0.500 - 0.600	0.5420
0.600 - 0.700	0.6408
0.700 - 0.900	0.7701

Table 6: Table of $\langle z \rangle$ values used in Table 5.

|y| range	$e^+e^- \to \pi^\pm + X$		$e^+e^- \to k^\pm + X$		$e^+e^- \to p^\pm + X$	
	π fraction %	$\frac{1}{\sigma}\frac{d\sigma_\pi}{d\|y\|}$	k fraction %	$\frac{1}{\sigma}\frac{d\sigma_k}{d\|y\|}$	p fraction %	$\frac{1}{\sigma}\frac{d\sigma_p}{d\|y\|}$
0.0 – 0.2	85.5 ± 1.4	$(4.04 \pm 0.27) \times 10^0$	8.2 ± 1.0	$(3.89 \pm 0.47) \times 10^{-1}$	6.2 ± 0.9	$(2.94 \pm 0.39) \times 10^{-1}$
0.2 – 0.4	84.2 ± 1.4	$(3.94 \pm 0.26) \times 10^0$	9.1 ± 1.1	$(4.24 \pm 0.48) \times 10^{-1}$	6.8 ± 0.8	$(3.16 \pm 0.36) \times 10^{-1}$
0.4 – 0.6	85.9 ± 1.2	$(3.98 \pm 0.25) \times 10^0$	8.6 ± 0.9	$(4.00 \pm 0.42) \times 10^{-1}$	5.5 ± 0.6	$(2.54 \pm 0.26) \times 10^{-1}$
0.6 – 0.8	85.2 ± 1.2	$(4.07 \pm 0.25) \times 10^0$	9.4 ± 1.0	$(4.48 \pm 0.47) \times 10^{-1}$	5.5 ± 0.6	$(2.62 \pm 0.28) \times 10^{-1}$
0.8 – 1.0	84.5 ± 1.4	$(4.00 \pm 0.23) \times 10^0$	10.7 ± 1.3	$(5.08 \pm 0.60) \times 10^{-1}$	4.7 ± 0.7	$(2.24 \pm 0.33) \times 10^{-1}$
1.0 – 1.2	84.2 ± 1.6	$(4.16 \pm 0.23) \times 10^0$	10.6 ± 1.4	$(5.24 \pm 0.72) \times 10^{-1}$	5.3 ± 0.9	$(2.60 \pm 0.46) \times 10^{-1}$
1.2 – 1.6	83.2 ± 3.0	$(4.02 \pm 0.22) \times 10^0$	12.0 ± 1.9	$(5.80 \pm 0.98) \times 10^{-1}$	4.8 ± 2.7	$(2.32 \pm 1.38) \times 10^{-1}$
1.6 – 2.0	84.0 ± 2.3	$(3.55 \pm 0.20) \times 10^0$	12.9 ± 1.5	$(5.46 \pm 0.66) \times 10^{-1}$	3.1 ± 2.0	$(1.31 \pm 0.88) \times 10^{-1}$
2.0 – 2.4	82.9 ± 1.9	$(2.86 \pm 0.17) \times 10^0$	14.1 ± 1.8	$(4.86 \pm 0.66) \times 10^{-1}$	3.0 ± 0.7	$(1.03 \pm 0.25) \times 10^{-1}$
2.4 – 3.0	83.6 ± 1.6	$(1.64 \pm 0.10) \times 10^0$	14.4 ± 1.5	$(2.84 \pm 0.30) \times 10^{-1}$	1.9 ± 0.5	$(3.80 \pm 0.96) \times 10^{-2}$
3.0 – 4.0	87.0 ± 1.5	$(5.01 \pm 0.33) \times 10^{-1}$	12.7 ± 1.4	$(7.32 \pm 0.82) \times 10^{-2}$	0.3 ± 0.2	$(1.46 \pm 0.99) \times 10^{-3}$

Sphericity Axis

Table 7: Table of the measured rapidity distributions $(1/\sigma)(d\sigma/d|y|)$ and particle fractions for pions, kaons, and protons as a function of $y \doteq (1/2)\ln((E+p_{||})/(E-p_{||}))$ using the sphericity axis.

|y| range	$e^+e^- \to \pi^\pm + X$		$e^+e^- \to k^\pm + X$		$e^+e^- \to p^\pm + X$	
	π fraction %	$\frac{1}{\sigma}\frac{d\sigma_\pi}{d\|y\|}$	k fraction %	$\frac{1}{\sigma}\frac{d\sigma_k}{d\|y\|}$	p fraction %	$\frac{1}{\sigma}\frac{d\sigma_p}{d\|y\|}$
0.0 – 0.2	86.3 ± 1.4	$(3.32 \pm 0.23) \times 10^0$	7.8 ± 1.1	$(3.00 \pm 0.39) \times 10^{-1}$	5.9 ± 0.9	$(2.27 \pm 0.32) \times 10^{-1}$
0.2 – 0.4	84.2 ± 1.4	$(3.98 \pm 0.26) \times 10^0$	9.2 ± 1.1	$(4.35 \pm 0.49) \times 10^{-1}$	6.6 ± 0.8	$(3.13 \pm 0.36) \times 10^{-1}$
0.4 – 0.6	85.7 ± 1.2	$(4.01 \pm 0.25) \times 10^0$	8.3 ± 0.9	$(3.90 \pm 0.40) \times 10^{-1}$	6.0 ± 0.7	$(2.80 \pm 0.28) \times 10^{-1}$
0.6 – 0.8	84.3 ± 1.3	$(4.01 \pm 0.24) \times 10^0$	10.3 ± 1.1	$(4.88 \pm 0.50) \times 10^{-1}$	5.5 ± 0.6	$(2.61 \pm 0.28) \times 10^{-1}$
0.8 – 1.0	84.4 ± 1.4	$(4.12 \pm 0.23) \times 10^0$	10.5 ± 1.2	$(5.13 \pm 0.60) \times 10^{-1}$	5.0 ± 0.7	$(2.45 \pm 0.35) \times 10^{-1}$
1.0 – 1.2	84.3 ± 1.6	$(4.24 \pm 0.23) \times 10^0$	10.8 ± 1.4	$(5.42 \pm 0.71) \times 10^{-1}$	4.9 ± 0.9	$(2.46 \pm 0.45) \times 10^{-1}$
1.2 – 1.6	84.1 ± 2.7	$(4.18 \pm 0.23) \times 10^0$	12.4 ± 1.9	$(6.16 \pm 1.00) \times 10^{-1}$	3.5 ± 2.2	$(1.76 \pm 1.14) \times 10^{-1}$
1.6 – 2.0	83.4 ± 1.9	$(3.74 \pm 0.21) \times 10^0$	13.5 ± 1.5	$(6.04 \pm 0.71) \times 10^{-1}$	3.1 ± 1.3	$(1.41 \pm 0.60) \times 10^{-1}$
2.0 – 2.4	82.8 ± 1.7	$(2.98 \pm 0.18) \times 10^0$	14.0 ± 1.6	$(5.05 \pm 0.59) \times 10^{-1}$	3.2 ± 0.7	$(1.17 \pm 0.27) \times 10^{-1}$
2.4 – 3.0	84.9 ± 1.5	$(1.71 \pm 0.11) \times 10^0$	13.9 ± 1.5	$(2.79 \pm 0.29) \times 10^{-1}$	1.3 ± 0.4	$(2.59 \pm 0.75) \times 10^{-2}$
3.0 – 4.0	91.7 ± 1.2	$(4.36 \pm 0.30) \times 10^{-1}$	8.1 ± 1.2	$(3.86 \pm 0.54) \times 10^{-2}$	0.2 ± 0.1	$(8.56 \pm 5.99) \times 10^{-4}$

Thrust Axis

Table 8: Same as Table 7 only using the thrust axis.

p_t range	$e^+e^- \to \pi^\pm + X$		$e^+e^- \to k^\pm + X$		$e^+e^- \to p^\pm + X$	
	π fraction %	$\frac{1}{\sigma}\frac{d\sigma_\pi}{dp_t^2}$	k fraction %	$\frac{1}{\sigma}\frac{d\sigma_k}{dp_t^2}$	p fraction %	$\frac{1}{\sigma}\frac{d\sigma_p}{dp_t^2}$
0.0 – 0.2	91.2 ± 1.0	$(8.05 \pm 0.53) \times 10^{1}$	6.7 ± 0.9	$(5.90 \pm 0.74) \times 10^{0}$	2.1 ± 0.4	$(1.85 \pm 0.33) \times 10^{0}$
0.2 – 0.4	86.4 ± 1.2	$(3.21 \pm 0.18) \times 10^{1}$	10.0 ± 1.1	$(3.69 \pm 0.38) \times 10^{0}$	3.6 ± 0.5	$(1.35 \pm 0.17) \times 10^{0}$
0.4 – 0.6	81.0 ± 1.5	$(9.76 \pm 0.54) \times 10^{0}$	13.7 ± 1.4	$(1.65 \pm 0.17) \times 10^{0}$	5.3 ± 0.6	$(6.40 \pm 0.74) \times 10^{-1}$
0.6 – 0.8	75.1 ± 1.9	$(2.94 \pm 0.17) \times 10^{0}$	17.5 ± 1.8	$(6.86 \pm 0.76) \times 10^{-1}$	7.4 ± 0.9	$(2.89 \pm 0.35) \times 10^{-1}$
0.8 – 1.2	72.0 ± 2.2	$(6.82 \pm 0.40) \times 10^{-1}$	19.1 ± 2.1	$(1.81 \pm 0.22) \times 10^{-1}$	8.9 ± 1.2	$(8.45 \pm 1.17) \times 10^{-2}$
1.2 – 1.8	67.1 ± 3.2	$(9.01 \pm 0.60) \times 10^{-2}$	21.4 ± 2.5	$(2.87 \pm 0.38) \times 10^{-2}$	11.4 ± 2.7	$(1.53 \pm 0.40) \times 10^{-2}$
1.8 – 2.4	–	$(1.23 \pm 0.12) \times 10^{-2}$	–	$(5.86 \pm 0.96) \times 10^{-3}$	–	–
2.4 – 3.0	–	$(2.26 \pm 0.39) \times 10^{-3}$	–	$(1.25 \pm 0.68) \times 10^{-3}$	–	–
3.0 – 4.0	–	$(3.06 \pm 1.01) \times 10^{-4}$	–	–	–	–

Sphericity Axis

Table 9: Table of the p_t-distributions $(1/\sigma)(d\sigma/dp_t^2)$ and particle fractions for pions, kaons, and protons as a function of p_t using the sphericity axis.

p_t range	$e^+e^- \to \pi^\pm + X$		$e^+e^- \to k^\pm + X$		$e^+e^- \to p^\pm + X$	
	π fraction %	$\frac{1}{\sigma}\frac{d\sigma_\pi}{dp_t^2}$	k fraction %	$\frac{1}{\sigma}\frac{d\sigma_k}{dp_t^2}$	p fraction %	$\frac{1}{\sigma}\frac{d\sigma_p}{dp_t^2}$
0.0 – 0.2	92.1 ± 0.9	$(8.06 \pm 0.53) \times 10^{1}$	6.1 ± 0.8	$(5.38 \pm 0.69) \times 10^{0}$	1.7 ± 0.3	$(1.53 \pm 0.28) \times 10^{0}$
0.2 – 0.4	87.0 ± 1.1	$(3.19 \pm 0.18) \times 10^{1}$	9.5 ± 1.0	$(3.47 \pm 0.37) \times 10^{0}$	3.5 ± 0.5	$(1.29 \pm 0.16) \times 10^{0}$
0.4 – 0.6	80.4 ± 1.6	$(9.47 \pm 0.53) \times 10^{0}$	13.7 ± 1.4	$(1.61 \pm 0.17) \times 10^{0}$	5.8 ± 0.7	$(6.88 \pm 0.78) \times 10^{-1}$
0.6 – 0.8	74.8 ± 2.0	$(3.02 \pm 0.17) \times 10^{0}$	17.6 ± 1.8	$(7.12 \pm 0.80) \times 10^{-1}$	7.6 ± 0.9	$(3.06 \pm 0.38) \times 10^{-1}$
0.8 – 1.2	70.2 ± 2.3	$(7.17 \pm 0.41) \times 10^{-1}$	22.2 ± 2.1	$(2.27 \pm 0.25) \times 10^{-1}$	7.6 ± 1.1	$(7.74 \pm 1.18) \times 10^{-2}$
1.2 – 1.8	68.6 ± 2.9	$(1.05 \pm 0.07) \times 10^{-1}$	22.8 ± 2.4	$(3.50 \pm 0.42) \times 10^{-2}$	8.7 ± 2.3	$(1.33 \pm 0.39) \times 10^{-2}$
1.8 – 2.4	62.3 ± 4.6	$(1.58 \pm 0.14) \times 10^{-2}$	28.8 ± 4.0	$(7.31 \pm 1.23) \times 10^{-3}$	8.9 ± 4.2	$(2.26 \pm 1.15) \times 10^{-3}$
2.4 – 3.0	67.5 ± 7.8	$(3.79 \pm 0.53) \times 10^{-3}$	24.6 ± 6.0	$(1.38 \pm 0.39) \times 10^{-3}$	7.9 ± 7.5	$(4.42 \pm 4.51) \times 10^{-4}$
3.0 – 4.0	51.3 ± 11.6	$(3.17 \pm 0.83) \times 10^{-4}$	43.5 ± 11.7	$(2.69 \pm 1.02) \times 10^{-4}$	5.2 ± 8.1	$(3.20 \pm 5.24) \times 10^{-5}$

Thrust Axis

Table 10: Same as Table 9 only using the thrust axis.

p_t range	$e^+e^- \to \pi^\pm + X$		$e^+e^- \to k^\pm + X$		$e^+e^- \to p^\pm + X$	
	π fraction %	$\frac{1}{\sigma}\frac{d\sigma_\pi}{d\|y\|dp_t^2}$	k fraction %	$\frac{1}{\sigma}\frac{d\sigma_k}{d\|y\|dp_t^2}$	p fraction %	$\frac{1}{\sigma}\frac{d\sigma_p}{d\|y\|dp_t^2}$
0.0 – 0.2	92.5 ± 1.0	$(2.49 \pm 0.23) \times 10^1$	5.0 ± 0.8	$(1.34 \pm 0.18) \times 10^0$	2.6 ± 0.5	$(6.88 \pm 1.28) \times 10^{-1}$
0.2 – 0.4	89.1 ± 0.9	$(1.21 \pm 0.07) \times 10^1$	6.8 ± 0.7	$(9.29 \pm 0.86) \times 10^{-1}$	4.1 ± 0.5	$(5.59 \pm 0.61) \times 10^{-1}$
0.4 – 0.6	82.0 ± 1.3	$(3.72 \pm 0.20) \times 10^0$	11.1 ± 1.1	$(5.04 \pm 0.49) \times 10^{-1}$	6.9 ± 0.7	$(3.11 \pm 0.29) \times 10^{-1}$
0.6 – 0.8	76.6 ± 1.8	$(1.27 \pm 0.07) \times 10^0$	14.0 ± 1.6	$(2.33 \pm 0.29) \times 10^{-1}$	9.4 ± 1.0	$(1.56 \pm 0.16) \times 10^{-1}$
0.8 – 1.0	71.8 ± 3.6	$(4.64 \pm 0.33) \times 10^{-1}$	17.7 ± 3.7	$(1.14 \pm 0.28) \times 10^{-1}$	10.5 ± 1.5	$(6.77 \pm 0.92) \times 10^{-2}$
1.0 – 1.2	63.1 ± 5.2	$(2.00 \pm 0.22) \times 10^{-1}$	24.8 ± 5.4	$(7.84 \pm 2.13) \times 10^{-2}$	12.1 ± 2.4	$(3.83 \pm 0.74) \times 10^{-2}$
1.2 – 1.4	72.5 ± 4.2	$(1.01 \pm 0.09) \times 10^{-1}$	16.4 ± 3.5	$(2.28 \pm 0.55) \times 10^{-2}$	11.1 ± 3.1	$(1.54 \pm 0.47) \times 10^{-2}$
1.4 – 1.6	63.4 ± 7.2	$(5.01 \pm 0.64) \times 10^{-2}$	18.3 ± 4.4	$(1.45 \pm 0.36) \times 10^{-2}$	18.3 ± 7.7	$(1.45 \pm 0.73) \times 10^{-2}$
1.6 – 2.0	–	$(1.78 \pm 0.20) \times 10^{-2}$	–	$(7.43 \pm 1.56) \times 10^{-3}$	–	–
2.0 – 2.4	–	$(5.50 \pm 0.85) \times 10^{-3}$	–	–	–	–
2.4 – 2.8	–	$(2.51 \pm 0.54) \times 10^{-3}$	–	–	–	–
2.8 – 3.2	–	$(1.22 \pm 0.36) \times 10^{-3}$	–	$(4.28 \pm 2.59) \times 10^{-4}$	–	–
3.2 – 4.0	–	$(1.34 \pm 0.75) \times 10^{-4}$	–	–	–	–

$|y|$ range 0. to 1. Sphericity Axis

p_t range	$e^+e^- \to \pi^\pm + X$		$e^+e^- \to k^\pm + X$		$e^+e^- \to p^\pm + X$	
	π fraction %	$\frac{1}{\sigma}\frac{d\sigma_\pi}{d\|y\|dp_t^2}$	k fraction %	$\frac{1}{\sigma}\frac{d\sigma_k}{d\|y\|dp_t^2}$	p fraction %	$\frac{1}{\sigma}\frac{d\sigma_p}{d\|y\|dp_t^2}$
0.0 – 0.2	92.3 ± 1.3	$(2.81 \pm 0.16) \times 10^1$	5.6 ± 1.2	$(1.71 \pm 0.36) \times 10^0$	2.1 ± 0.7	$(6.50 \pm 2.22) \times 10^{-1}$
0.2 – 0.4	84.5 ± 1.9	$(1.13 \pm 0.06) \times 10^1$	10.8 ± 1.6	$(1.45 \pm 0.22) \times 10^0$	4.7 ± 1.2	$(6.28 \pm 1.60) \times 10^{-1}$
0.4 – 0.8	78.0 ± 2.8	$(2.25 \pm 0.13) \times 10^0$	16.2 ± 2.0	$(4.68 \pm 0.62) \times 10^{-1}$	5.8 ± 2.4	$(1.67 \pm 0.73) \times 10^{-1}$
0.8 – 1.2	73.8 ± 5.0	$(2.82 \pm 0.18) \times 10^{-1}$	20.2 ± 2.9	$(7.74 \pm 1.18) \times 10^{-2}$	6.0 ± 5.4	$(2.29 \pm 2.20) \times 10^{-2}$
1.2 – 1.6	65.8 ± 4.4	$(4.41 \pm 0.35) \times 10^{-2}$	30.4 ± 3.9	$(2.04 \pm 0.33) \times 10^{-2}$	3.8 ± 3.6	$(2.54 \pm 2.47) \times 10^{-3}$
1.6 – 2.4	72.7 ± 5.2	$(5.18 \pm 0.61) \times 10^{-3}$	23.8 ± 4.8	$(1.69 \pm 0.40) \times 10^{-3}$	3.6 ± 3.1	$(2.55 \pm 2.28) \times 10^{-4}$
2.4 – 3.2	–	$(1.10 \pm 0.46) \times 10^{-4}$	–	$(2.81 \pm 3.17) \times 10^{-4}$	–	–

$|y|$ range 1. to 2. Sphericity Axis

p_t range	$e^+e^- \to \pi^\pm + X$		$e^+e^- \to k^\pm + X$		$e^+e^- \to p^\pm + X$	
	π fraction %	$\frac{1}{\sigma}\frac{d\sigma_\pi}{d\|y\|dp_t^2}$	k fraction %	$\frac{1}{\sigma}\frac{d\sigma_k}{d\|y\|dp_t^2}$	p fraction %	$\frac{1}{\sigma}\frac{d\sigma_p}{d\|y\|dp_t^2}$
0.0 – 0.2	88.8 ± 1.5	$(1.79 \pm 0.11) \times 10^1$	9.0 ± 1.3	$(1.82 \pm 0.27) \times 10^0$	2.3 ± 0.6	$(4.55 \pm 1.27) \times 10^{-1}$
0.2 – 0.4	83.7 ± 1.7	$(6.80 \pm 0.42) \times 10^0$	13.7 ± 1.6	$(1.11 \pm 0.14) \times 10^0$	2.6 ± 0.7	$(2.10 \pm 0.54) \times 10^{-1}$
0.4 – 0.8	79.0 ± 2.0	$(1.13 \pm 0.07) \times 10^0$	18.7 ± 1.9	$(2.68 \pm 0.29) \times 10^{-1}$	2.3 ± 0.7	$(3.30 \pm 1.01) \times 10^{-2}$
0.8 – 1.2	70.2 ± 3.6	$(6.43 \pm 0.53) \times 10^{-2}$	26.0 ± 3.3	$(2.38 \pm 0.36) \times 10^{-2}$	3.8 ± 2.1	$(3.48 \pm 1.96) \times 10^{-3}$
1.2 – 1.6	60.2 ± 11.0	$(4.60 \pm 1.17) \times 10^{-3}$	25.3 ± 9.4	$(1.93 \pm 0.83) \times 10^{-3}$	14.5 ± 9.6	$(1.11 \pm 0.83) \times 10^{-3}$
1.6 – 2.4	–	$(7.46 \pm 4.08) \times 10^{-4}$	–	$(3.86 \pm 4.30) \times 10^{-5}$	–	–

$|y|$ range 2. to 3. Sphericity Axis

p_t range	$e^+e^- \to \pi^\pm + X$		$e^+e^- \to k^\pm + X$		$e^+e^- \to p^\pm + X$	
	π fraction %	$\frac{1}{\sigma}\frac{d\sigma_\pi}{d\|y\|dp_t^2}$	k fraction %	$\frac{1}{\sigma}\frac{d\sigma_k}{d\|y\|dp_t^2}$	p fraction %	$\frac{1}{\sigma}\frac{d\sigma_p}{d\|y\|dp_t^2}$
0.0 – 0.2	87.7 ± 1.6	$(6.01 \pm 0.43) \times 10^0$	12.1 ± 1.6	$(8.33 \pm 1.13) \times 10^{-1}$	0.1 ± 0.2	$(9.95 \pm 16.0) \times 10^{-3}$
0.2 – 0.4	86.6 ± 1.8	$(1.72 \pm 0.12) \times 10^0$	13.2 ± 1.8	$(2.62 \pm 0.36) \times 10^{-1}$	0.1 ± 0.2	$(2.89 \pm 3.03) \times 10^{-3}$
0.4 – 0.8	85.8 ± 3.0	$(1.13 \pm 0.10) \times 10^{-1}$	13.8 ± 3.0	$(1.83 \pm 0.43) \times 10^{-2}$	0.4 ± 0.5	$(4.81 \pm 6.44) \times 10^{-4}$
0.8 – 1.2	–	$(8.76 \pm 4.97) \times 10^{-4}$	–	–	–	–

$|y|$ range 3. to 4. Sphericity Axis

Table 11: Table of the cross sections $(1/\sigma)(d\sigma/d|y|dp_t^2)$ and particle fractions for pions, kaons, and protons as a function of p_t in the rapidity intervals $0 < |y| < 1$, $1 < |y| < 2$, $2 < |y| < 3$, and $3 < |y| < 4$. The sphericity axis was used as the event axis.

p_t range	$e^+e^- \to \pi^\pm + X$		$e^+e^- \to k^\pm + X$		$e^+e^- \to p^\pm + X$	
	π fraction %	$\frac{1}{\sigma}\frac{d\sigma_\pi}{d\|y\|dp_t^2}$	k fraction %	$\frac{1}{\sigma}\frac{d\sigma_k}{d\|y\|dp_t^2}$	p fraction %	$\frac{1}{\sigma}\frac{d\sigma_p}{d\|y\|dp_t^2}$
0.0 – 0.2	92.2 ± 1.0	$(2.49 \pm 0.23) \times 10^{1}$	5.1 ± 0.8	$(1.39 \pm 0.18) \times 10^{0}$	2.6 ± 0.5	$(7.14 \pm 1.28) \times 10^{-1}$
0.2 – 0.4	88.8 ± 0.9	$(1.20 \pm 0.07) \times 10^{1}$	7.1 ± 0.7	$(9.58 \pm 0.88) \times 10^{-1}$	4.2 ± 0.5	$(5.64 \pm 0.61) \times 10^{-1}$
0.4 – 0.6	81.3 ± 1.3	$(3.52 \pm 0.19) \times 10^{0}$	11.1 ± 1.1	$(4.82 \pm 0.47) \times 10^{-1}$	7.6 ± 0.7	$(3.32 \pm 0.30) \times 10^{-1}$
0.6 – 0.8	75.4 ± 1.9	$(1.14 \pm 0.07) \times 10^{0}$	14.9 ± 1.7	$(2.26 \pm 0.28) \times 10^{-1}$	9.7 ± 1.0	$(1.48 \pm 0.15) \times 10^{-1}$
0.8 – 1.0	74.1 ± 3.7	$(4.46 \pm 0.32) \times 10^{-1}$	16.7 ± 3.8	$(1.00 \pm 0.26) \times 10^{-1}$	9.2 ± 1.4	$(5.56 \pm 0.81) \times 10^{-2}$
1.0 – 1.2	64.9 ± 4.9	$(1.71 \pm 0.17) \times 10^{-1}$	22.8 ± 5.0	$(6.01 \pm 1.64) \times 10^{-2}$	12.3 ± 2.4	$(3.25 \pm 0.65) \times 10^{-2}$
1.2 – 1.4	71.1 ± 4.1	$(9.96 \pm 0.90) \times 10^{-2}$	15.5 ± 3.1	$(2.17 \pm 0.48) \times 10^{-2}$	13.4 ± 3.5	$(1.87 \pm 0.54) \times 10^{-2}$
1.4 – 1.6	57.6 ± 9.9	$(3.70 \pm 0.59) \times 10^{-2}$	24.9 ± 6.2	$(1.60 \pm 0.39) \times 10^{-2}$	17.5 ± 12.2	$(1.12 \pm 0.93) \times 10^{-2}$
1.6 – 2.0	–	$(1.89 \pm 0.20) \times 10^{-2}$	–	$(6.94 \pm 1.56) \times 10^{-3}$	–	–
2.0 – 2.4	–	$(6.23 \pm 0.91) \times 10^{-3}$	–	$(3.99 \pm 0.92) \times 10^{-3}$	–	–
2.4 – 2.8	–	$(3.17 \pm 0.63) \times 10^{-3}$	–	$(1.05 \pm 0.32) \times 10^{-3}$	–	–
2.8 – 3.2	–	$(5.26 \pm 1.91) \times 10^{-4}$	–	$(3.04 \pm 2.27) \times 10^{-4}$	–	–
3.2 – 4.0	–	$(2.22 \pm 0.84) \times 10^{-4}$	–	$(1.44 \pm 0.79) \times 10^{-4}$	–	–

$|y|$ range 0. to 1. Thrust Axis

p_t range	$e^+e^- \to \pi^\pm + X$		$e^+e^- \to k^\pm + X$		$e^+e^- \to p^\pm + X$	
	π fraction %	$\frac{1}{\sigma}\frac{d\sigma_\pi}{d\|y\|dp_t^2}$	k fraction %	$\frac{1}{\sigma}\frac{d\sigma_k}{d\|y\|dp_t^2}$	p fraction %	$\frac{1}{\sigma}\frac{d\sigma_p}{d\|y\|dp_t^2}$
0.0 – 0.2	91.7 ± 1.3	$(2.93 \pm 0.17) \times 10^{1}$	6.4 ± 1.2	$(2.05 \pm 0.39) \times 10^{0}$	1.8 ± 0.6	$(5.86 \pm 1.95) \times 10^{-1}$
0.2 – 0.4	84.6 ± 1.8	$(1.18 \pm 0.06) \times 10^{1}$	10.7 ± 1.5	$(1.48 \pm 0.23) \times 10^{0}$	4.7 ± 1.1	$(6.53 \pm 1.55) \times 10^{-1}$
0.4 – 0.8	79.0 ± 2.6	$(2.27 \pm 0.13) \times 10^{0}$	16.5 ± 2.0	$(4.73 \pm 0.62) \times 10^{-1}$	4.5 ± 2.1	$(1.30 \pm 0.62) \times 10^{-1}$
0.8 – 1.2	71.9 ± 3.4	$(3.04 \pm 0.18) \times 10^{-1}$	23.1 ± 2.6	$(9.75 \pm 1.26) \times 10^{-2}$	5.0 ± 3.1	$(2.11 \pm 1.39) \times 10^{-2}$
1.2 – 1.6	69.4 ± 4.3	$(5.83 \pm 0.42) \times 10^{-2}$	26.6 ± 3.7	$(2.24 \pm 0.38) \times 10^{-2}$	4.0 ± 3.4	$(3.39 \pm 2.99) \times 10^{-3}$
1.6 – 2.4	66.9 ± 4.2	$(9.16 \pm 0.82) \times 10^{-3}$	25.1 ± 3.8	$(3.44 \pm 0.61) \times 10^{-3}$	8.0 ± 3.1	$(1.09 \pm 0.45) \times 10^{-3}$
2.4 – 3.2	66.9 ± 9.5	$(1.03 \pm 0.22) \times 10^{-3}$	28.1 ± 8.2	$(4.31 \pm 1.46) \times 10^{-4}$	5.0 ± 7.5	$(7.70 \pm 12.0) \times 10^{-5}$
3.2 – 4.0	–	$(6.53 \pm 3.65) \times 10^{-5}$	–	$(3.69 \pm 3.49) \times 10^{-4}$	–	–

$|y|$ range 1. to 2. Thrust Axis

p_t range	$e^+e^- \to \pi^\pm + X$		$e^+e^- \to k^\pm + X$		$e^+e^- \to p^\pm + X$	
	π fraction %	$\frac{1}{\sigma}\frac{d\sigma_\pi}{d\|y\|dp_t^2}$	k fraction %	$\frac{1}{\sigma}\frac{d\sigma_k}{d\|y\|dp_t^2}$	p fraction %	$\frac{1}{\sigma}\frac{d\sigma_p}{d\|y\|dp_t^2}$
0.0 – 0.2	91.0 ± 1.3	$(1.85 \pm 0.12) \times 10^{1}$	8.1 ± 1.3	$(1.64 \pm 0.26) \times 10^{0}$	0.9 ± 0.4	$(1.73 \pm 0.80) \times 10^{-1}$
0.2 – 0.4	85.5 ± 1.7	$(6.71 \pm 0.42) \times 10^{0}$	12.7 ± 1.6	$(9.95 \pm 1.28) \times 10^{-1}$	1.8 ± 0.6	$(1.44 \pm 0.46) \times 10^{-1}$
0.4 – 0.8	78.1 ± 2.0	$(1.18 \pm 0.07) \times 10^{0}$	17.8 ± 1.9	$(2.68 \pm 0.30) \times 10^{-1}$	4.1 ± 0.9	$(6.15 \pm 1.38) \times 10^{-2}$
0.8 – 1.2	64.9 ± 3.0	$(1.14 \pm 0.08) \times 10^{-1}$	31.3 ± 2.9	$(5.49 \pm 0.62) \times 10^{-2}$	3.8 ± 1.6	$(6.61 \pm 2.91) \times 10^{-3}$
1.2 – 1.6	65.7 ± 5.0	$(1.46 \pm 0.17) \times 10^{-2}$	31.7 ± 4.9	$(7.03 \pm 1.37) \times 10^{-3}$	2.6 ± 1.8	$(5.79 \pm 4.11) \times 10^{-4}$
1.6 – 2.4	61.6 ± 13.6	$(1.21 \pm 0.28) \times 10^{-3}$	31.0 ± 10.7	$(6.11 \pm 2.37) \times 10^{-4}$	7.4 ± 15.1	$(1.45 \pm 3.19) \times 10^{-4}$

$|y|$ range 2. to 3. Thrust Axis

p_t range	$e^+e^- \to \pi^\pm + X$		$e^+e^- \to k^\pm + X$		$e^+e^- \to p^\pm + X$	
	π fraction %	$\frac{1}{\sigma}\frac{d\sigma_\pi}{d\|y\|dp_t^2}$	k fraction %	$\frac{1}{\sigma}\frac{d\sigma_k}{d\|y\|dp_t^2}$	p fraction %	$\frac{1}{\sigma}\frac{d\sigma_p}{d\|y\|dp_t^2}$
0.0 – 0.2	–	$(5.24 \pm 0.39) \times 10^{0}$	–	$(2.46 \pm 0.68) \times 10^{-1}$	–	–
0.2 – 0.4	90.4 ± 1.6	$(1.33 \pm 0.10) \times 10^{0}$	9.1 ± 1.6	$(1.34 \pm 0.24) \times 10^{-1}$	0.4 ± 0.3	$(6.26 \pm 4.96) \times 10^{-3}$
0.4 – 0.8	84.4 ± 2.9	$(1.33 \pm 0.12) \times 10^{-1}$	15.3 ± 2.8	$(2.41 \pm 0.48) \times 10^{-2}$	0.3 ± 0.3	$(4.87 \pm 5.12) \times 10^{-4}$
0.8 – 1.2	89.6 ± 36.6	$(3.25 \pm 0.93) \times 10^{-3}$	10.4 ± 36.6	$(3.79 \pm 14.8) \times 10^{-4}$	–	–

$|y|$ range 3. to 4. Thrust Axis

Table 12: Same as Table 11 only using the thrust axis.

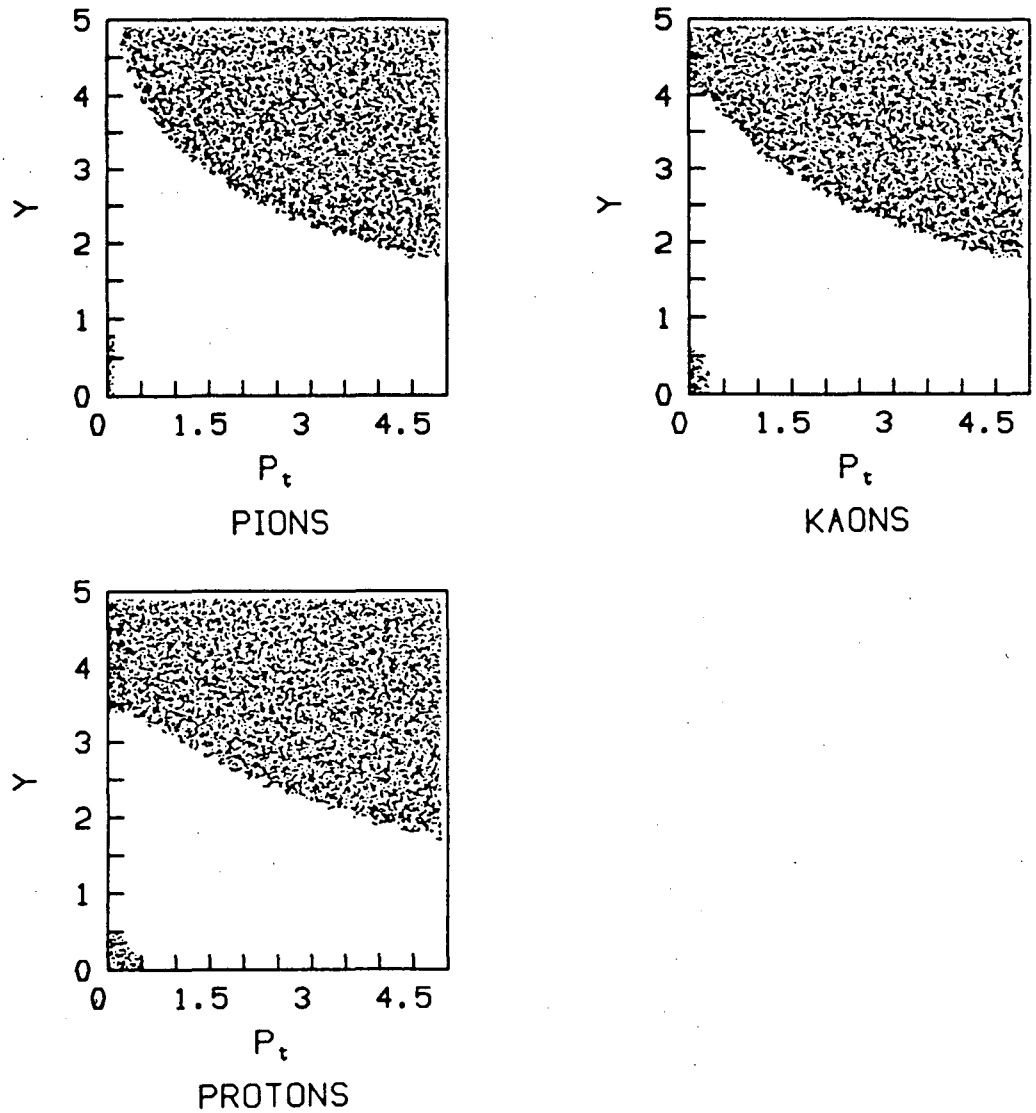

Figure 37: The shaded areas show the kinematically forbidden simultaneous $|y|$ and p_t values (upper right) and values excluded by the acceptance cuts (lower left) for pions, kaons, and protons.

6.2 Comparison with hadronization models

The tabulated results of the previous section are plotted in figures 38-47. Each data point is placed at the center of the appropriate bin. These results should be of interest to hadronization model builders because of the number of different distributions for pions, kaons, and protons, the particle fractions, and the quality of the data. The figures show the predictions of four Monte Carlos, the Lund Monte Carlo V5.3 [39] (solid line), the Lund Monte Carlo V6.3 [40] (dotdash line), the Webber Monte Carlo V3 [41] (dashed line), and the Gottschalk Monte Carlo V2 [42] (dotted line). Closed form expressions for the hadron spectra also exist using the assumption of Local Parton-Hadron Duality [43]. Comparisons to these predictions are also presented.

The Lund Monte Carlo V5.3 generates an initial parton state from fixed 2nd order QCD. Color strings are formed between the initial state quarks and gluons. The strings break by the formation of quark-antiquark pairs with flavor chosen according to prescribed probabilities. Values of $\vec{p}_t$ and $-\vec{p}_t$ are generated for the pair quark and antiquark, respectively. A meson is formed from the endpoint quark (antiquark) and the pair antiquark (quark). The meson $\vec{p}_t$ is the vector sum of the constituent $\vec{p}_t$'s, and the spin is chosen according to a vector to pseudoscalar ratio parameter. The quark content and spin identify the meson. The meson's longitudinal momentum is obtained from the Lund symmetric fragmentation function [44]. The pair quark or antiquark not used in the meson forms the new string end and the process is repeated. Baryons are produced by generating diquark-antidiquark pairs in the string instead of quark-antiquark pairs. The Lund Monte Carlo was tuned using the older data set [45]. The non-default parameters we used were $\alpha_s = 0.183$, $a = 0.955$ (a is a parameter in the symmetric fragmentation function), and $\sigma_q = 0.350$ GeV (σ_q controls the p_t distribution).

The Lund Monte Carlo V6.3 generates the initial partonic state using a leading log parton shower calculation instead of fixed order QCD. Interference effects in the shower lead to an angular ordering of the emitted gluons. An observable effect of the angular ordering is a prominent dip in the rapidity plateau near $y = 0$. Nonperturbative effects are included by introducing color strings stretched from quark to antiquark via gluons (kinks in the strings). The strings fragment producing particles as in the Lund V5.3 Monte Carlo. We used the default parameters for the Lund V6.3 Monte Carlo.

The Webber Monte Carlo V3 generates parton showers which lead to clusters, which in turn decay to form the observed particles. The parton showers are done in QCD using the leading infra-red and collinear singularities. They also include interference effects leading to an angular ordering of the emitted gluons and a dip in the rapidity plateau near $y = 0$. The partons of the shower form color singlet clusters of limited extension in both coordinate and momentum space (preconfinement). These clusters undergo phase-space-dominated decays to known resonances, which in turn decay to form the observed particles. We used the default values of the parameters when we ran the Monte Carlo.

	$\pi^{\pm}$	$k^{\pm}$	$p^{\pm}$
Lund V5.3	10.4	1.47	0.67
Lund V6.3	10.3	1.44	0.62
Webber V3	10.6	1.41	0.51
Gottschalk V2	10.3	1.34	0.71

Table 13: The charged pion, kaon, and proton multiplicities in the Lund, Webber, and Gottschalk Monte Carlos. Statistical errors were small and neglected.

The Gottschalk Monte Carlo "Caltech-II" breaks hadronization into three distinct phases. The first phase is a parton shower including coherence effects as in the Webber Monte Carlo. In the second phase color strings connect the partons produced in the shower, and the strings then break according to a covariant model analogous to the Lund model. However, the string breaking is terminated when the string pieces (clusters) are within 1-2 GeV of particle production threshold. The third phase involves decaying these clusters using a phenomenological fit to low mass data. The parameters in the Gottschalk Monte Carlo were left at their default values.

Overall, the four Monte Carlos reproduce the data fairly well. At large momentum, however, none of Monte Carlos could reproduce the data for all three particle species. It is not clear, at present, whether the Monte Carlos can be tuned to fit the data, or whether changes to the Monte Carlos need to be made. The pion, kaon, and proton multiplicities are summarized in Table 13 for the four Monte Carlos (the statistical errors were negligible).

Recently, several authors have obtained closed form expressions for the hadron spectra [43]. They start by calculating the parton (quark and gluon) spectra in perturbative QCD using the modified leading log approximation. Then they assume a Local Parton-Hadron Duality, which means there is a direct correspondence between parton and hadron differential distributions (inclusive spectra, correlations, etc.).

An interesting consequence of this is that perturbative QCD predicts a "humpbacked" structure to the parton plateau due to interference effects [43]. Thus, if the Local Parton-Hadron Duality exists, the hadron spectra should have the same characteristics of rising at low momenta, peaking, and falling at high momenta. Fig. 48 compares the predictions to our momentum distribution for pions, kaons, and protons. Both the shape and position of the peaks seem to agree with the data. Furthermore, the shape is obtained from a universal function for all hadron species, which is an interesting prediction that seems to agree with the data. Confirmation of these ideas would add new information on the hadronization mechanism and allow model-independent predictions of observable quantities from QCD.

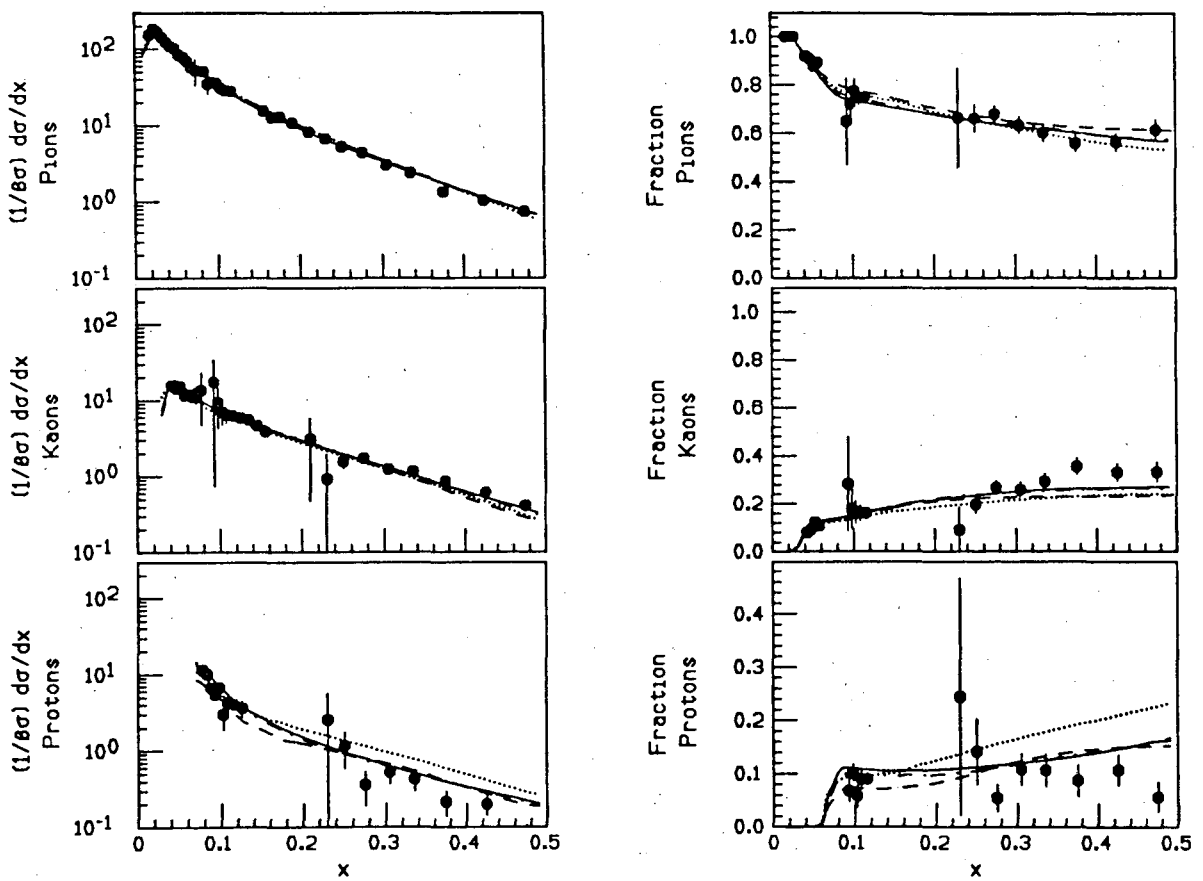

Figure 38: Plot of the measured cross sections $\langle 1/\beta \rangle (1/\sigma)(d\sigma/dx)$ and particle fractions for pions, kaons, and protons as a function of $x = 2E/\sqrt{s}$. Monte Carlo results: Lund V5.3 (solid line), Lund V6.3 (dotdash line), Webber V3 (dashed line), and Gottschalk V2 (dotted line).

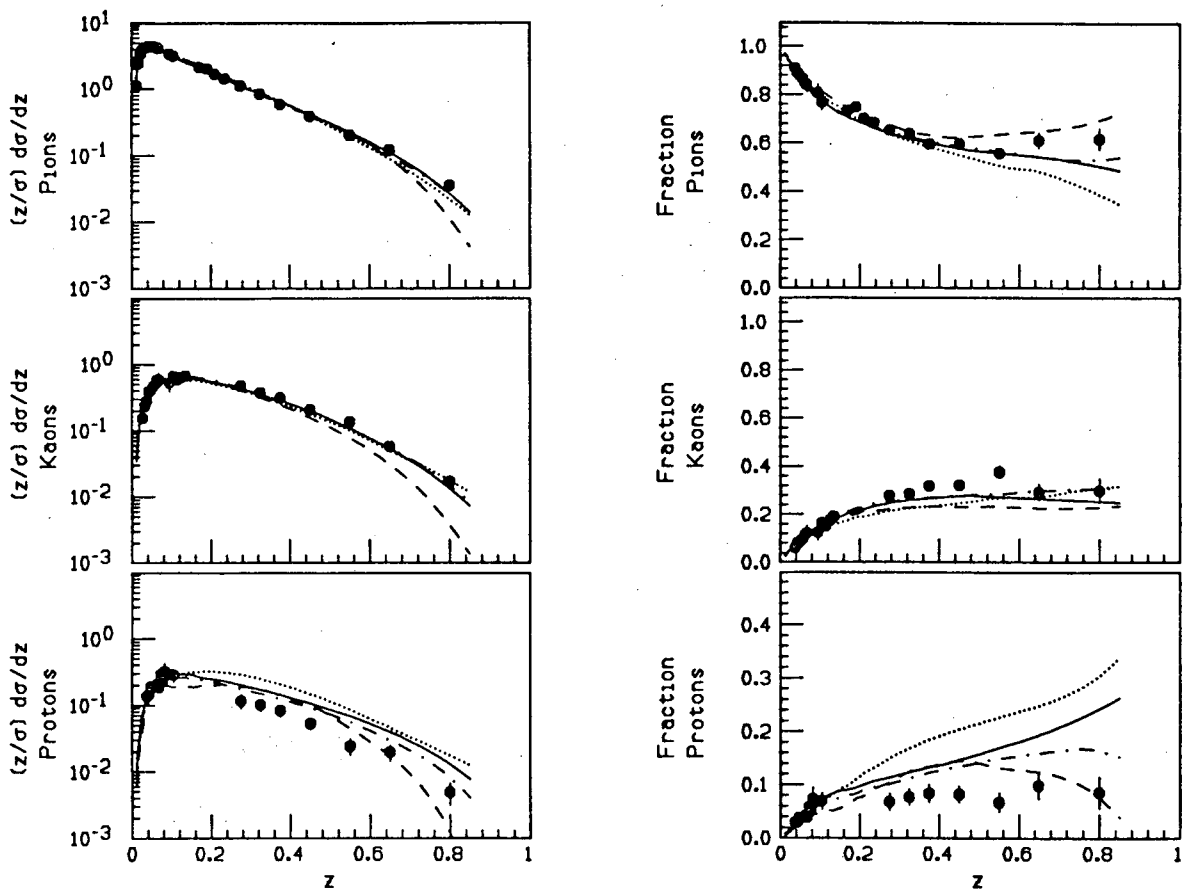

Figure 39: Plot of the measured cross sections $(\langle z \rangle/\sigma)(d\sigma/dz)$ and particle fractions for pions, kaons, and protons as a function of $z = 2p/\sqrt{s}$. Monte Carlo results: Lund V5.3 (solid line), Lund V6.3 (dotdash line), Webber V3 (dashed line), and Gottschalk V2 (dotted line).

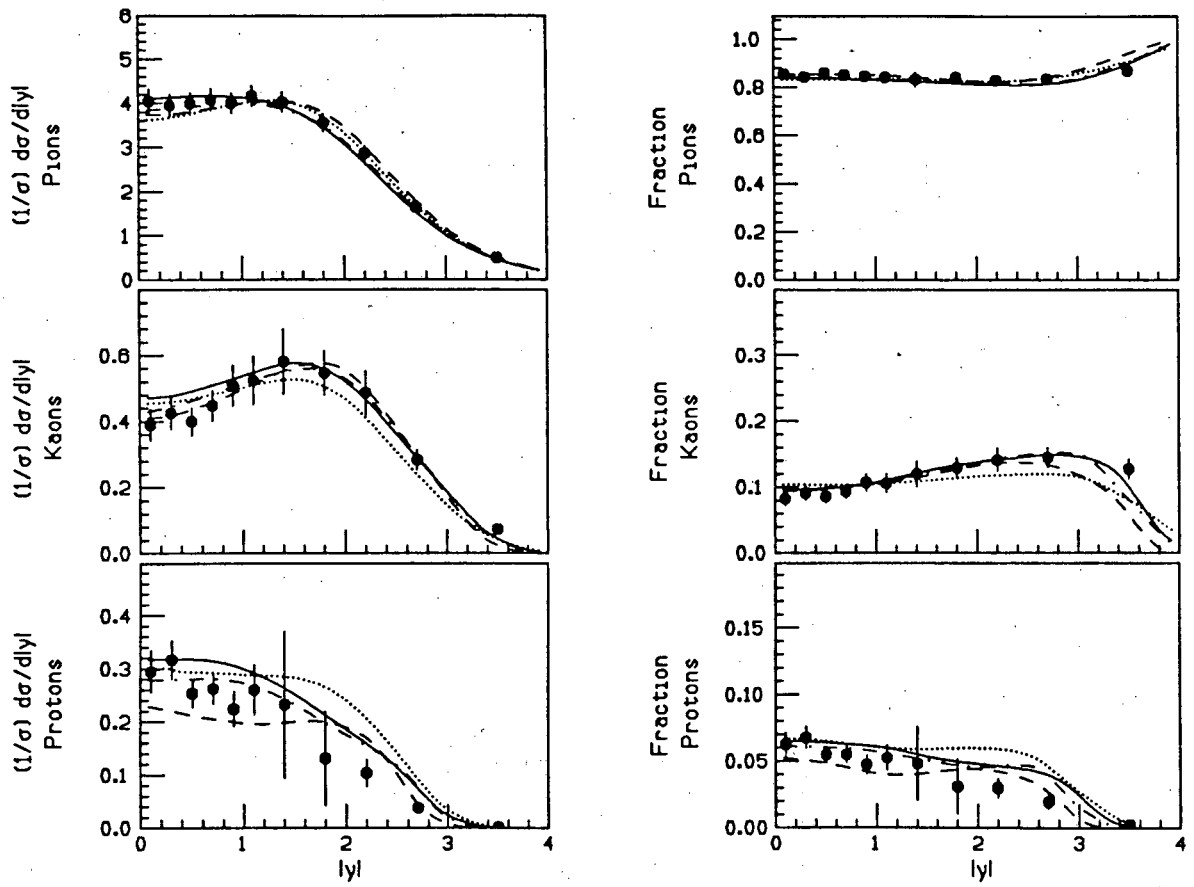

Figure 40: Plot of the measured cross sections $(1/\sigma)(d\sigma/d|y|)$ and particle fractions for pions, kaons, and protons as a function of rapidity using the sphericity axis. Monte Carlo results: Lund V5.3 (solid line), Lund V6.3 (dotdash line), Webber V3 (dashed line), and Gottschalk V2 (dotted line).

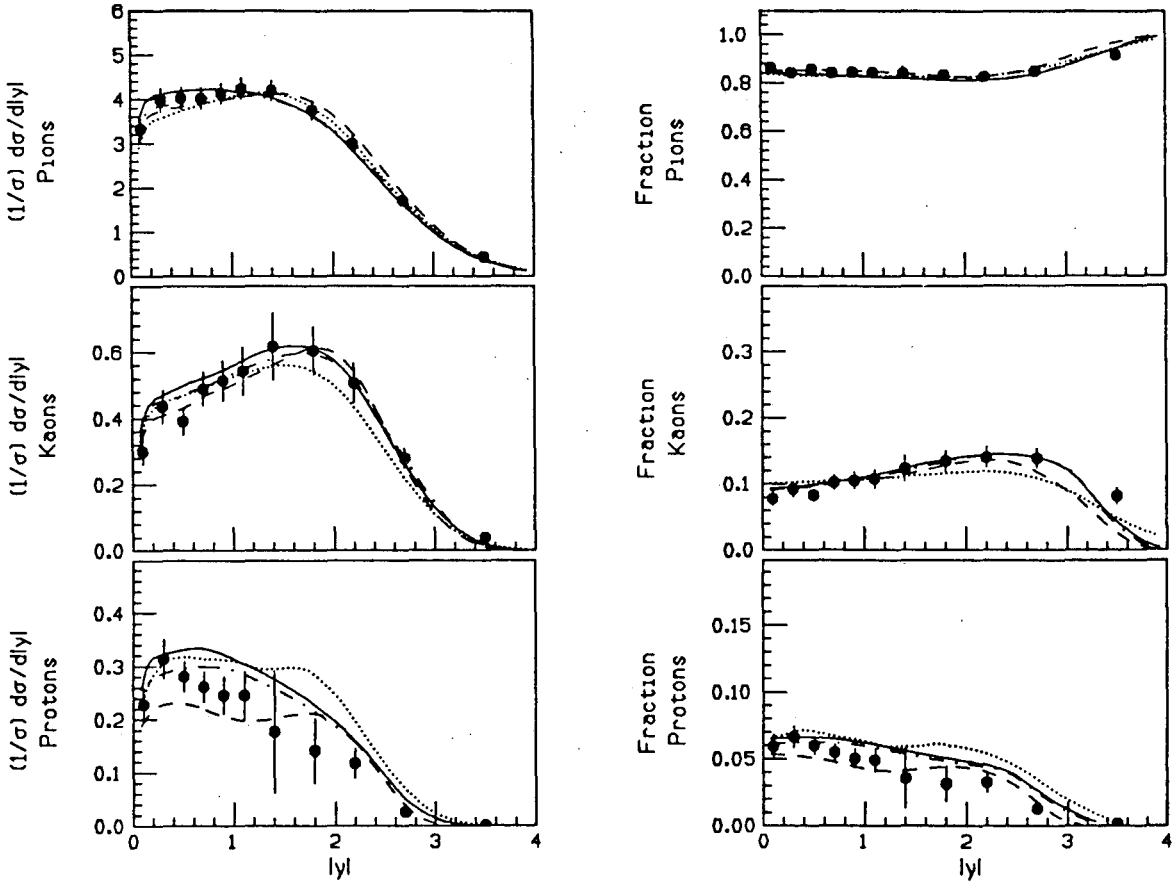

Figure 41: Same as Fig. 40 only using the thrust axis.

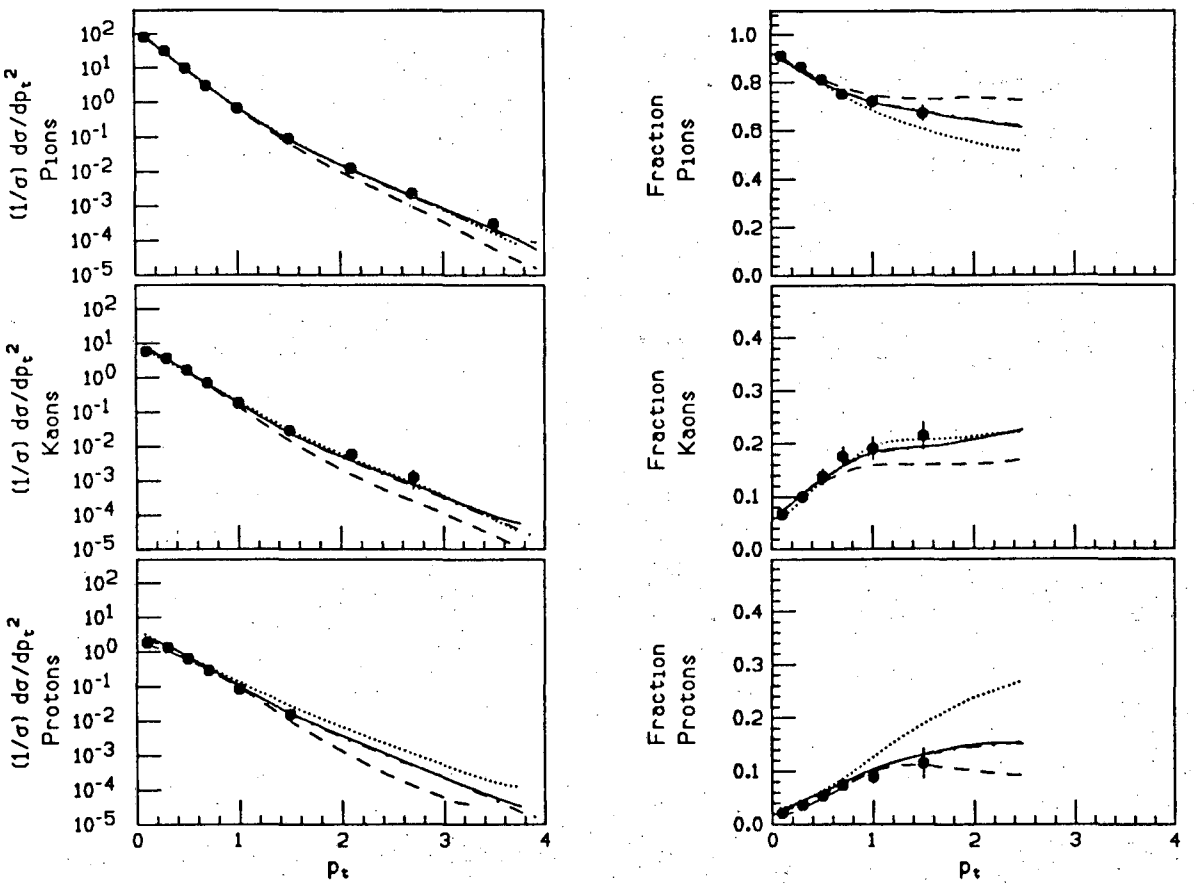

Figure 42: Plot of the measured cross sections $(1/\sigma)(d\sigma/dp_t^2)$ and particle fractions for pions, kaons, and protons as a function of p_t using the sphericity axis. Monte Carlo results: Lund V5.3 (solid line), Lund V6.3 (dotdash line), Webber V3 (dashed line), and Gottschalk V2 (dotted line).

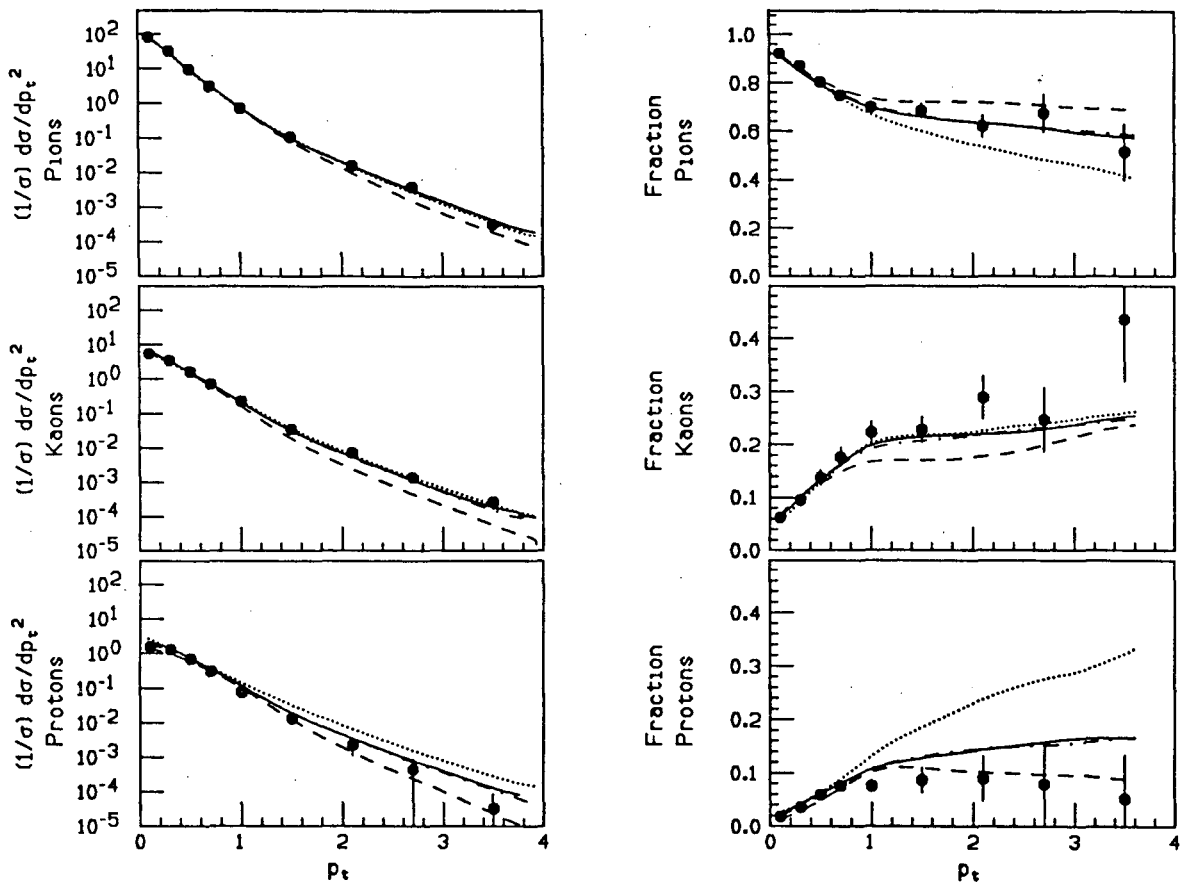

Figure 43: Same as Fig. 42 only using the thrust axis.

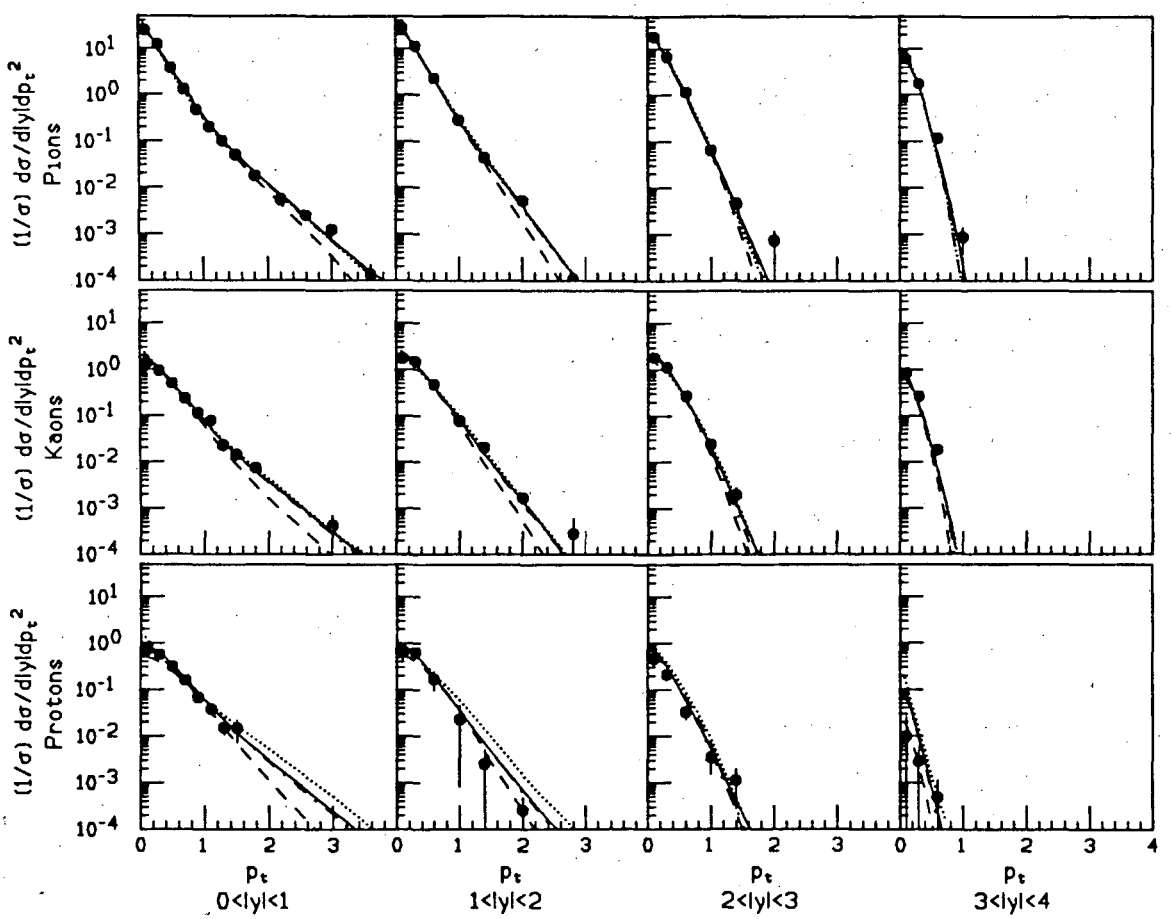

Figure 44: Plot of the measured cross sections $(1/\sigma)(d\sigma/d|y|dp_t^2)$ for pions, kaons, and protons as a function of p_t in the rapidity intervals indicated. The event axis was the sphericity axis. Monte Carlo results: Lund V5.3 (solid line), Lund V6.3 (dotdash line), Webber V3 (dashed line), and Gottschalk V2 (dotted line).

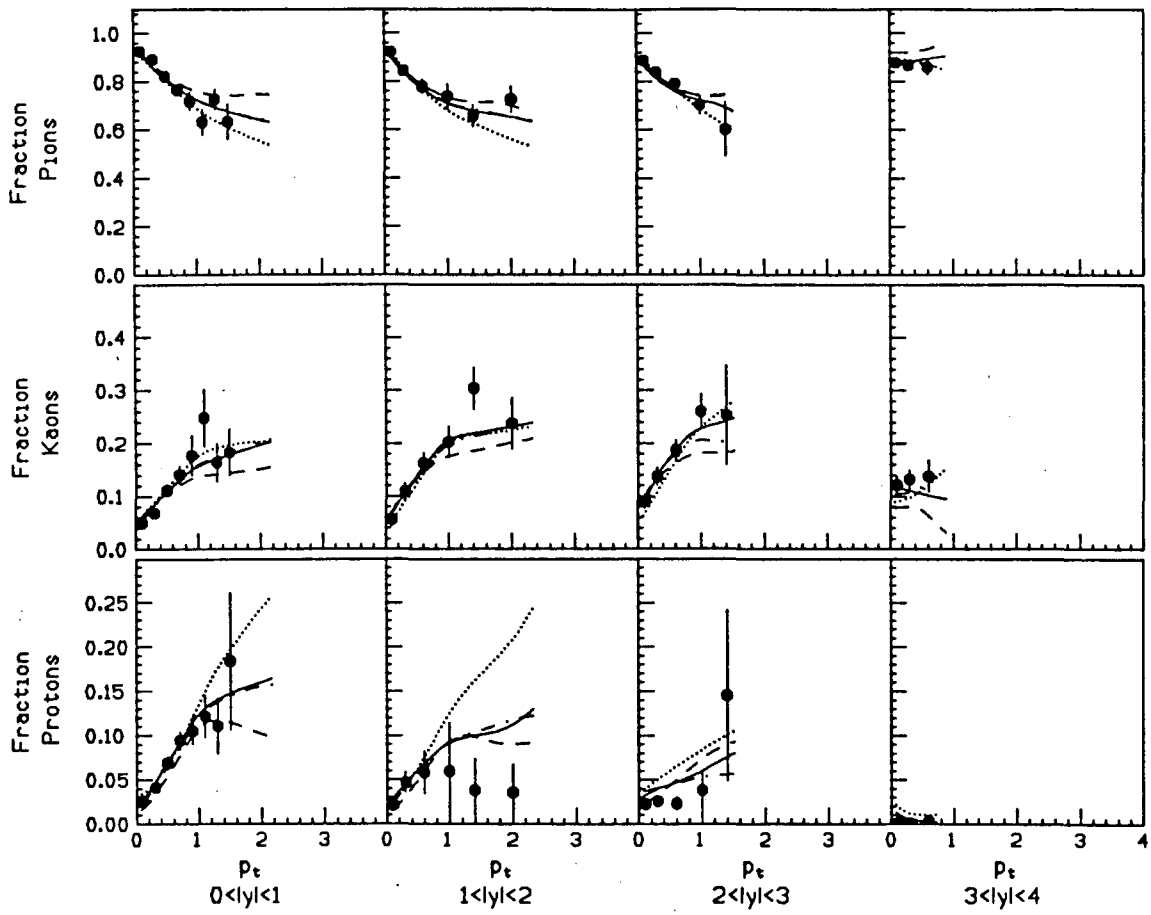

Figure 45: Plot of the particle fractions as a function of p_t in the rapidity intervals indicated. The sphericity axis was used as the event axis. Monte Carlo results: Lund V5.3 (solid line), Lund V6.3 (dotdash line), Webber V3 (dashed line), and Gottschalk V2 (dotted line).

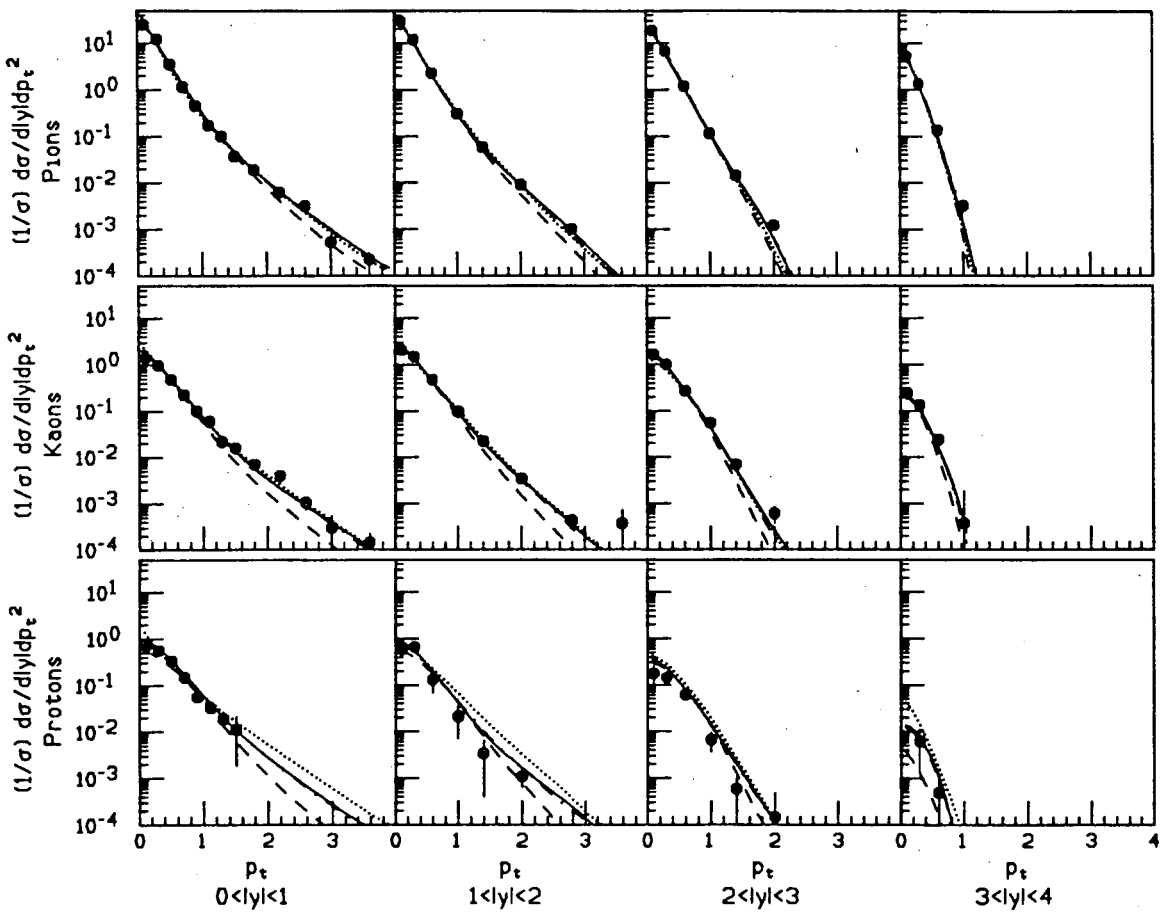

Figure 46: Same as Fig. 44 only using the thrust axis as the event axis.

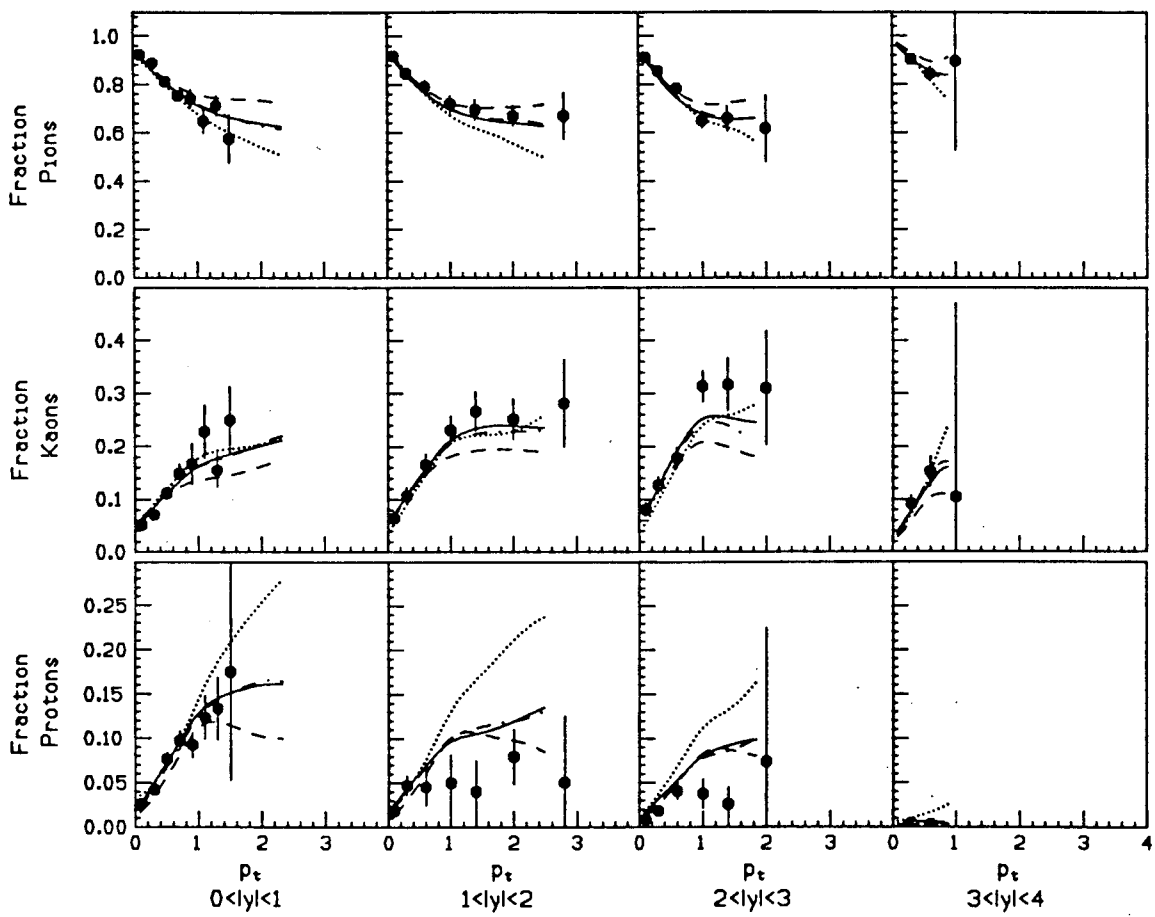

Figure 47: Same as Fig. 45 only using the thrust axis as the event axis.

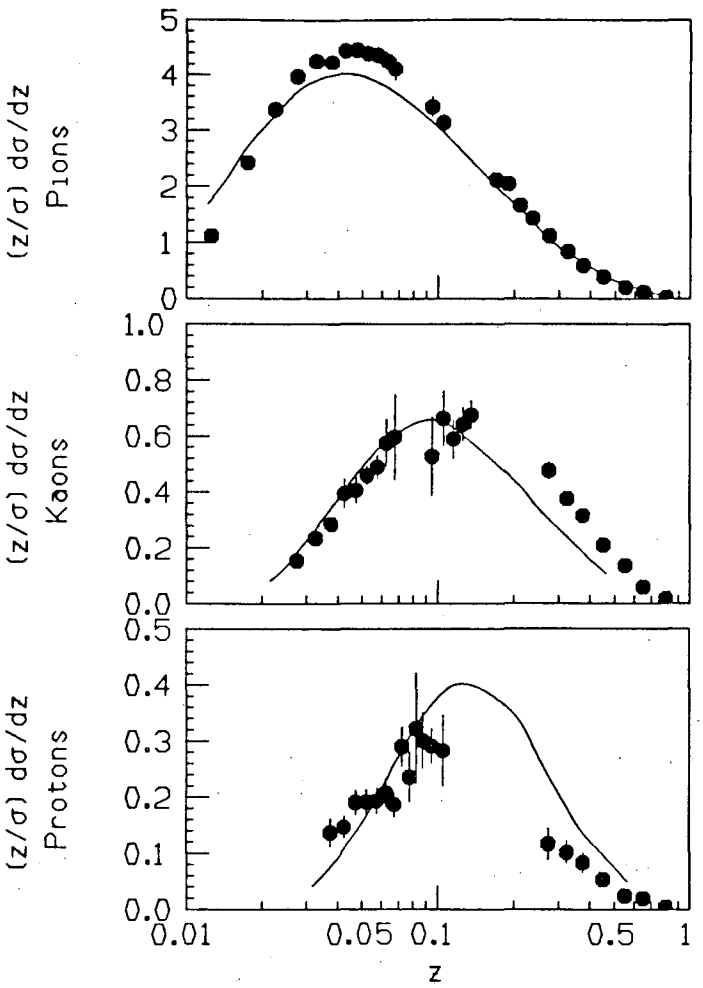

Figure 48: Comparison of the cross section $(z/\sigma)(d\sigma/dz)$, $z = 2p/\sqrt{s}$, to the predictions of Azimov *et al.* Ref. [43].

7 SUMMARY AND CONCLUSIONS

Quark hadronization is still far from understood. With the advent of better experimental data, different types of hadronization models are adjusted and tend to converge to the data. This paper provides a test of current models and a coherent data set with which to test future models.

The Time Projection Chamber allows particle identification by simultaneous momentum and dE/dx measurements. The nominal momentum resolution is $(\sigma_p/p)^2 = (0.015)^2 + (0.007p)^2$ (p in GeV/c), and the nominal dE/dx resolution is 3.4%. Outside the crossover regions, pions, kaons, and protons are identified correctly more than 95%, 85%, and 60% of the time, respectively. Overall, the particle identification capabilities of the TPC are better than any previous e^+e^- storage ring detector.

An unfolding technique and a fitting technique were used to measure cross sections and particle fractions for pions, kaons, and protons as a function of several variables: energy, momentum, rapidity, and transverse momentum. As a function of momentum we found that all the particle fractions level off at high z ($z = 2p/\sqrt{s}$). As a function of p_t the kaon and proton fractions rise at low p_t and tend to level off at high p_t. As a function of rapidity the pion, kaon, and proton fractions are fairly flat, with values of about 85%, 9%, and 6%, respectively, near $y = 0$. The measured multiplicities for pions, kaons, and protons are 10.6 ± 0.6, 1.43 ± 0.09, and 0.53 ± 0.07, respectively.

Overall, the Lund V5.3 and V6.3, Webber V3, and Gottschalk V2 Monte Carlo models reproduced the data fairly well. At high momentum, however, none of the Monte Carlos could reproduce the data for pions, kaons, and protons using the default parameters. The Local Parton-Hadron Duality model of Azimov *et al.* did surprisingly well at reproducing the pion, kaon, and proton momentum distributions, considering the small number of assumptions and parameters in the model.

These measurements are also useful for comparisons between hadron production in e^+e^- annihilation and hadron production in other processes. For example, in a previous publication we found the shapes of the p_t distributions and the particle composition in the central rapidity region to be similar to the corresponding distributions from the ISR [46]. Such agreement is predicted by string models and is in agreement with the hypothesis of a universal mechanism of particle production.

Acknowledgements: We would like to thank the PEP staff and the engineers, programmers and technicians who made these results possible. This work was supported by the United States Department of Energy, the National Science Foundation, the Joint Japan-United States Collaboration in High Energy Physics, and the Foundation for Fundamental Research on Matter in the Netherlands.

References

[1] R. J. Madaras, TPC Internal Note TPC-LBL-82-89, Unpublished.

[2] G. Cowan, TPC Internal Note TPC-LBL-87-23, Unpublished.

[3] W. Gorn *et al.*, IEEE Trans. Nucl. Sci. **26**, 68 (1979); and IEEE Trans. Nucl. Sci. **30**, 153 (1983).

[4] H. Aihara *et al.*, IEEE Trans. Nucl. Sci. **30**, 63,76,162 (1983); and Nucl. Instr. Meth. **223**, 40 (1984).

[5] H. Aihara *et al.*, IEEE Trans. Nucl. Sci. **30**, 117 (1983); and Nucl. Instr. Meth. **217**, 259 (1983).

[6] W. W. Moses, University of California Ph. D. Thesis, (Berkeley, 1986).

[7] C. Buchanan *et al.*, in *Proceedings Of The Gas Calorimeter Workshop*, Batavia, 1982, p. 284.

[8] J. Bakken *et al.*, IEEE Trans. Nucl. Sci. **30**, 67 (1983).

[9] M. P. Cain *et al.*, Phys. Lett. **147B**, 232 (1984).

[10] P. Nemethy and P. J. Oddone, Nucl. Instr. Meth. **212**, 273 (1983).

[11] R. C. Jared, D. A. Landis, and F. S. Goulding, IEEE Trans. Nucl. Sci. **29**, 57 (1982).

[12] H. Aihara *et al.*, IEEE Trans. Nucl. Sci. **30**, 63 (1983).

[13] G. R. Lynch and N. J. Hadley, in *International Conference On Instrumentation For Colliding Beam Physics* SLAC (1982).

[14] M. Shapiro, University of California Ph. D. Thesis, (Berkeley, 1984).

[15] G. Cowan, TPC Internal Note TPC-LBL-87-20, Unpublished.

[16] H. Aihara *et al.*, IEEE Trans. Nucl. Sci. **30**, 76 (1983).

[17] R. L. Gluckstern, Nucl. Instr. Meth. **24**, 381 (1963).

[18] M. Ronan *et al.*, IEEE Trans. Nucl. Sci. **29**, 427 (1982); M. Ronan, TPC Internal Note TPC-LBL-87-12, Unpublished.

[19] F. A. Berends and R. Kleiss, Nucl. Phys. **B178**, 141 (1981).

[20] G. Lynch, TPC Internal Note TPC-LBL-81-6, Unpublished.

[21] F. Lapique and F. Piuz, Nucl. Instr. Meth. **175**, 297 (1980).

[22] W. W. M. Allison and J. H. Cobb, Ann. Rev. Nucl. Sci. **30**, 253 (1980).

[23] R. Talman, Nucl. Instrum. Methods **159**, 189 (1979).

[24] L. Landau, J. Phys. USSR **8**, 201 (1944).

[25] H. D. Macabee and D. G. Papworth, Phys. Lett. **30A**, 241 (1969).

[26] Ya. I. Azimov *et al.*, Z. Phys. **C31**, 213 (1986).

[27] W. Hofmann, TPC Internal Note TPC-LBL-83-3, Unpublished.

[28] H. Aihara *et al.*, LBL report LBL-23635, to be published.

[29] L. Lyons: *Statistics for Nuclear and Particle Physicists*, Cambridge University Press, Cambridge 1986, p. 100.

[30] H. Aihara *et al.*, Phys. Rev. **D31**, 2719 (1985).

[31] H. Aihara *et al.*, Phys. Rev. Lett. **52**, 577 (1984).

[32] TASSO Collaboration, *Inclusive Pion, Kaon, and Proton Production in* e^+e^- *Annihilations at 34 GeV CMS Energy*, 1985 Int. Symp. on Lepton and Photon Interactions at High Energies, Kyoto, 1985.

[33] E. Fernandez *et al.*, Phys. Rev. **D31**, 1537 (1985).

[34] M. Derrick *et al.*, Phys. Rev. **D35**, 2639 (1987).

[35] H. Schellman *et al.*, Phys. Rev. **D31**, 3013 (1985).

[36] M. Althoff *et al.*, Z. Phys. **C22**, 307 (1984).

[37] J. F. Patrick *et al.*, Phys. Rev. Lett. **49**, 1232 (1982).

[38] A. Petersen *et al.*, SLAC publication SLAC-PUB-4290, to be published.

[39] T. Sjöstrand, Comput. Phys. Commun. **27**, 243 (1982); **28**, 229 (1983).

[40] T. Sjöstrand and M. Bengtsson, Comput. Phys. Commun. **43**, 367 (1987); T. Sjöstrand, Comput. Phys. Commun. **39**, 347 (1986).

[41] G. Marchesini and B. R. Webber, Nucl. Phys. **B238**, 1 (1984); B. R. Webber, Nucl. Phys. **B238**, 492 (1984).

[42] T. D. Gottschalk and D. A. Morris, Calt-68-1365 (1986).

[43] Ya. I. Azimov, Yu. L. Dokshitzer, V. A. Khoze, and S. I. Troyan, Z. Phys. **C31**, 213 (1986); **C27**, 65 (1985).

[44] B. Andersson, G. Gustafson, G. Ingelman, and T. Sjöstrand, Phys. Rep. **97**, 31 (1983).

[45] J. W. Gary, University of California Ph. D. Thesis, (Berkeley, 1985).

[46] H. Aihara *et al.*, Phys. Lett. **184B**, 114 (1987).

LAWRENCE BERKELEY LABORATORY
TECHNICAL INFORMATION DEPARTMENT
UNIVERSITY OF CALIFORNIA
BERKELEY, CALIFORNIA 94720